NTNU
Norwegian University of
Science and Technology

Chemical Vapour Deposition and Electron Microscopy Analysis of Graphene

Trond Rypdal Henninen

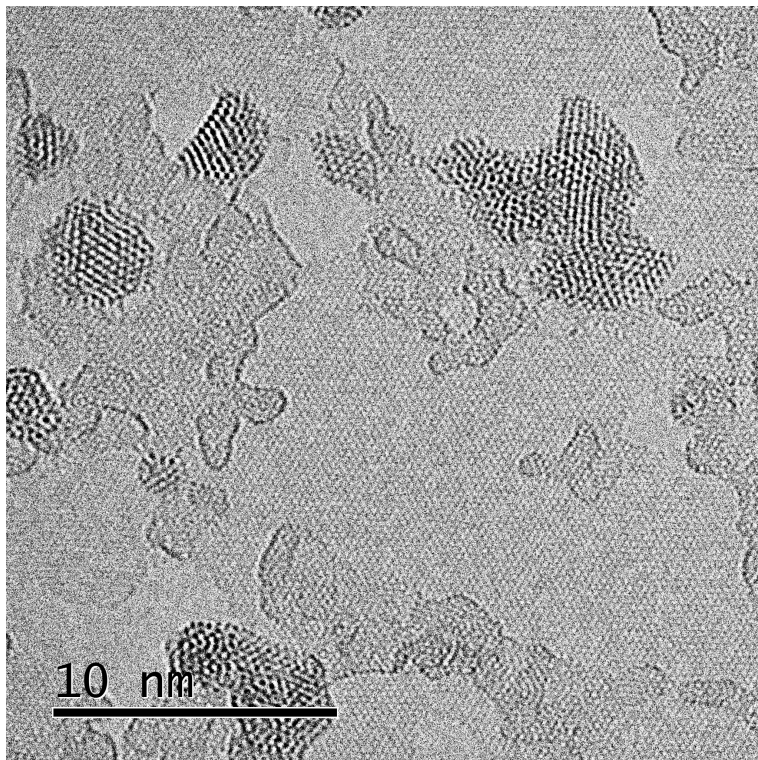Norwegian University of Science and Technology
Department of Physics

Chemical Vapour Deposition and Electron Microscopy Analysis of Graphene

Master Thesis
Trond Rypdal Henninen
June 21, 2016

10 nm

Front image: HRTEM image of a graphene monolayer with some holes, fragments of additional graphene layers and iron oxide nanoparticles on top. Taken at 80 kV with a JEOL ARM200F.

Abstract

Graphene is a promising material for many applications, including electronics, energy technologies, chemical filters and mechanical materials. In this work, graphene has been grown by chemical vapour deposition (CVD) on Cu foil. The as-grown foils were studied by scanning electron microscopy (SEM), before the Cu was etched and the graphene transferred, without the use of polymers, onto Si wafers for further SEM study. For further transmission electron microscopy (TEM) study, the graphene was instead transferred onto TEM grids. The samples were contaminated by SiO_2 nanoparticles from the CVD chamber walls, and iron oxide nanoparticles from the Fe-based etch.

For rapid structural analysis, SEM was found to be highly useful at low voltage of around 1 kV. This gave high contrast of the upper atomic layers of the surface, enabling study of details of graphene, like wrinkles, directly on the Cu surface. Transferring onto Si wafer also proved useful, as then grain boundaries in graphene could be studied in SEM. TEM was useful for determining the thickness of the graphene. Aberration corrected TEM enabled the study of defects in the graphene, while carbon mapping of the C-k peak by electron energy loss spectroscopy (EELS) gave monolayered thickness contrast of the graphene. High-angle annular dark-field scanning transmission electron microscope (HAADF-STEM) was used with high precision energy-dispersive X-ray spectroscopy (EDX) to chemically identify the nanoparticle contaminations.

A process for growing graphene directly on Si was also attempted, by first depositing 100 nm of Cu on the Si wafer, then graphene was grown by CVD and the Cu was evaporated. However, the graphene covering the Cu limited the evaporation of Cu, making it difficult to evaporate it completely. In this process the SiO_2 particles formed only on control Cu-foil samples, and were absent from the deposited Cu thin film on Si. This suggests the particles form due to unknown features of the Cu foil.

Sammendrag

Grafén er et lovende materiale for mange bruksområder som elektronikk, energiteknologi, kjemiske filtre og mekaniske materialer. I denne avhandlingen har grafén blitt grodd med kjemisk dampdeposisjon (CVD) på kobberfolie. Etter prosessen ble disse prøvene studert med sveipeelektronmikroskopi (SEM), før kobberet ble etset bort og grafénet ble overført, uten bruk av polymerer, til biter av silisiumskiver for videre SEM-studie. For å kunne studeres med transmisjonselektronmikroskopi (TEM), ble grafénet istedet overført til TEM-grids. Prøvene viste seg å være kontaminerte med SiO_2-nanopartikler fra veggene til CVD-kammeret, og jernoksidnanopartikler fra den jernbaserte etsen.

For rask ananlyse av overflaten var SEM svært nyttig ved lav akselerasjonsspenning på rundt 1 kV. Dette gav høy kontrast for de øverste atomlagene av overflaten til prøven, noe som gjorde det mulig å studere detaljer ved grafénet, slik som rynker, direkte på kobberfolieoverflaten. Å studere grafén på silisiumoverflaten viste seg også å være nyttig, ettersom korngrenser til grafén da ble synlig i SEM. TEM var nyttig for å finne tykkelsen til grafénet. Aberrasjonskorrigert TEM gjorde det mulig å studere defekter i grafénet, mens karbonmapping av Ck-toppen med elektronenergitapsspektroskopi (EELS) gav tykkelseskontrast med monolagsoppløsning av grafénet. Høyvinkelannularmørkefeltssveipetransmisjonselektronmikroskopi (HAADF-STEM) gjorde det mulig å gjøre energidispersiv røntgensprektroskopi (EDX) med høy presisjon, for å kjemisk identifisere nanopartikkelkontaminasjonen.

Det ble også prøvd en prosess for å gro grafén direkte på biter av silisiumskriver, ved først å deponere 100 nm med kobber på silisiumet. Deretter ble grafén grodd med CVD og kobberet fordampet vekk. Derimot begrenset grafénet som dekket kobberoverflaten, fordampingen av kobber, noe som gjorde det vanskelig å fjerne det fullstendig. I denne prosessen ble SiO_2-partikler bare funnet på kontrollprøven med kobberfolie, og ikke på kobbertynnfilmen på silisium. Dette indikerer at partiklene skapes grunnet en ukjent egenskap til kobberfolien.

Preface

This master thesis was done at the Norwegian University of Science and Technology (NTNU), at the Department of Physics (IFY), under supervision of prof. Ton van Helvoort, with Vidar Fauske as co-adviser. All the lab work was done at the NTNU NanoLab cleanroom, and TEMs were used at TEM Gemini Centre, NTNU.

Trond Rypdal Henninen
MTNANO
NTNU, Trondheim
June 21, 2016

Abbreviations

ADF	Annular dark-field
BF	Bright-field
BFP	Back focal plane
BSE	Backscattered electrons
CVD	Chemical vapour deposition
DF	Dark-field
EBD	Electron beam deposition
EDX	Energy-dispersive X-ray spectroscopy
EELS	Electron energy loss spectroscopy
FE(G)	Field emission (gun)
FFT	Fast Fourier transform
FLG	Few-layered graphene
LA-BSE	Low angle backscattered electrons
h-BN	Hexagonal boron nitride
HAADF	High-angle annular dark-field
HRTEM	High resolution transmission electron microscope
HT	High tension
MBE	Molecular beam epitaxy
SA	Selected area
SAD	Selected area diffraction
SADP	Selected area diffraction pattern
SE	Secondary electrons

SEM	Scanning electron microscope
STEM	Scanning transmission electron microscope
TEM	Transmission electron microscope
TF	Thin film
YAG	Yttrium aluminium garnet (detector material)

Contents

Chapter 1

Introduction

Graphene, a hexagonal monolayer of carbon atoms, was first observed in 1962 by Boehm et al.,[1] but was forgotten until its successful isolation and characterization in 2004,[2] by Andre Geim and Konstantin Novoselov. Due to the material's exceptional mechanical and electrical properties, the two received the Nobel prize in Physics in 2010 *"for groundbreaking experiments regarding the two-dimensional material graphene"*.[3] This has led to an incredible research effort internationally, making graphene and other similar two-dimensional materials, like h-BN and MoS_2 one of the hottest areas in today's scientific research.

Graphene's special combination of good mechanical, optical, electronical and chemical properties,[4,5] has led researchers to propose many different applications such as chemical membranes,[6] supercapacitors[7] and batteries.[8] Also noteworthy is its special quantum physical properties, such as room temperature quantum hall effect[9,10] and ballistic conduction,[11,12] and the possibility of high temperature superconductivity,[13,14] which has also made graphene a popular material for research into fundamental physics. However, due to its exceptionally high electron mobility, most research focus on use in various electronic devices, where high frequency nanoscale transistors is the ultimate goal, replacing silicon for future processing.[4,15,16]

Large scale industrial use seems to be in the not-so-distant future, as there have recently been breakthroughs is mass production, with large scale roll-to-roll mass production of high quality monolayer graphene by chemical vapour deposition (CVD),[17] and cheap large scale production of few-layer graphene in dispersion, by shear exfoliation of graphite.[18] Especially important is also the very recent demonstration of wafer-scale CVD growth of defect-free monocrystalline graphene on Ge, and its transfer onto an arbitrary substrate without introducing significant defects or impurities,[19] which has been required for integration into fabrication processes for high performance electronic components.

A new CVD system was recently installed in NTNU Nanolab, intended for growth of graphene, and few at NTNU has much experience with CVD growth of graphene. Therefore, the first important part of this thesis has been to work towards growing high quality, defect and contaminant free graphene. For effective optimization of the CVD process, rapid feedback of the quality of the as-grown graphene is important. The standard method for this is Raman spectrometry, which can quickly identify one or more layers of graphene.[20] However, such a device has not been available for this work. Instead scanning electron microscopy (SEM) has been explored as a method for easy characterization of the as-grown graphene. Thus, a large part of this thesis is dedicated to analysis of SEM images of graphene.

For more in-depth analysis of the material, compared to Raman and SEM, transmission electron microscopy (TEM) has been used. Three new TEMs have also recently been installed at the TEM Gemini Center at NTNU, so the second part of this work has been to figure out what are the capabilities for studying graphene using these microscopes. TEM enables high resolution imaging, analysis of the crystal structure through diffraction patterns, and detailed chemical analysis by energy-dispersive X-ray spectroscopy (EDX) and electron energy loss spectroscopy (EELS).

A third part of this thesis has been working towards future applications of graphene. In that regard, we have cooperated with others at NTNU, specifically the group of professors Bjørn-Ove Fimland and Helge Weman, that are growing GaAs and other III-V semiconductor nanowires on graphene using molecular beam epitaxy (MBE), combining the unique properties of both material systems, for use in optoelectronic devices.[21,22] In this project, co-adviser Vidar Fauske has studied cross-sections of the graphene/GaAs interface by atomic resolution TEM,[21] requiring high quality, uniform graphene without organic or particle contaminations. This has in the past been difficult to achieve, as the CVD growth and handling often leaves particles on the graphene. Additionally, the common liquid phase processes for transferring graphene from the growth substrate to a substrate,[23] has until recently been problematic, either introducing cracks and tears in the graphene due to capillary forces, or organic contamination from spin coated polymers used on the transfer process. Due to this, based on work by Ismach et al.,[24] an attempt was made to grow graphene on a 100 nm Cu thin film, followed by evaporation of the Cu, leaving graphene on the Si substrate below.

Chapter 2

Theory

2.1 Structure and Properties of Graphene

Graphene is a single layered 2D sheet of carbon atoms, making graphene the basis for the other allotropes of carbon, fullerenes, carbon nanotubes and graphite, but not diamond. This correlation is illustrated in figure 2.1a, where it is shown that 60 atoms on a graphene sheet can fold into a C-60 fullerene, a rectangle of graphene folds into a carbon nanotube, and many sheets of graphene stack into graphite. The carbon atoms in these graphene-based allotropes are sp^2-bonded, like a network of connected benzene rings, resulting in each atom having a loosely bound electron, and are thus electrically conducting. In comparison, the atoms in diamond are sp^3-bonded, and having no free electrons, are electrically insulating.

Multiple layers of graphene connect weakly between the layers, by van der Waals bonds between the layers, as shown in figure 2.1b. The crystal of graphene is a hexagonal lattice with two carbon atoms in the basis, as shown by the blue and white coloured atoms in the upper layer of figure 2.1b. Despite the two atoms being the same by symmetry, in regards to crystallography of the material, it is often convenient to consider them as two different atoms. In this crystal, we see that there are three different lattice distances, the distance between two nearest neighbours of carbon atoms of 1.42 Å (distance between a white and blue atom), the distance between two second nearest neighbours, of 2.46 Å (distance between two white or two blue atoms), and the interlayer distance of multiple stacked layers of 3.4 Å (slightly more than that of graphite). Multi-layer graphene typically stack in an alternating AB-structure, with blue atoms in one layer atop the white atoms in the layer below, as illustrated in the figure. Many layers of AB-stacked graphene are considered to be graphite, and as the number of layers increase, the material properties gradually change from the exceptional properties of the monolayer graphene, to the regular properties of bulk graphite.
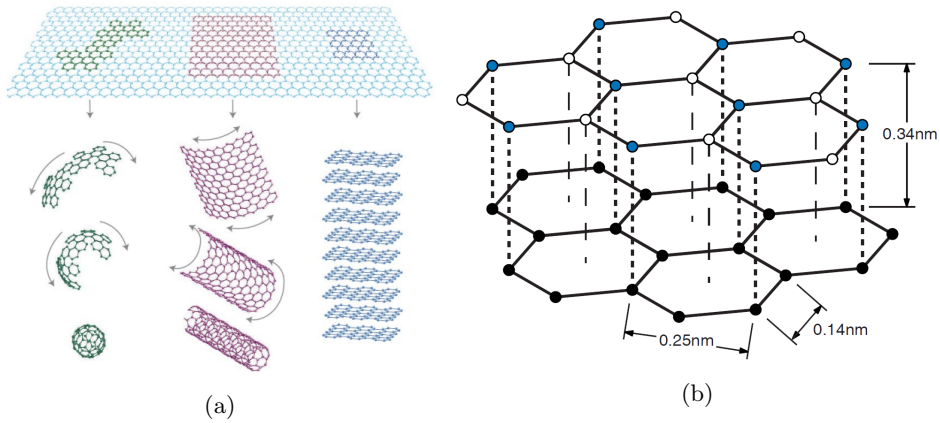
Figure 2.1: **(a)** Graphene sheets are the foundation of other allotropes of carbon, fullerenes, carbon nanotubes and graphite. From Geim and Novoselov.[4] **(b)** Atomic structure of two layers of graphene, with the characteristic lattice spacings: nearest neighbour - 0.14 nm, second nearest neighbour - 0.25 nm, both within the monolayer, and interlayer distance for typical AB-stacked graphene - 0.34 nm.[25]

The mechanical properties of the material is especially exceptional, with a breaking strength of 42 Nm^{-1} and a Young's modulus of E = 1.0 TPa,[26] it has a specific strength over 100 times that of steel.[27] It can also be elastically stretched up to 10 - 20%, which is also more than any other crystal.[28] This makes graphene not only the strongest material ever measured, but it also has the unusual combination of properties, being both strong and stiff, fracturing in a brittle manner, while still being very elastic. This has caused interest for using graphene to mechanically reinforce composite materials[29,30] and for NEMS application,[31,32] amongst other mechanical applications.

The electronic band structure of graphene is seen in figure 2.2. Here we see that the valence and conduction bands are in connection, but not overlapping at six points, called Dirac points. As the bands are connected but not overlapping, the material is typically referred to as a zero-bandgap semiconductor, as lattice strain, doping, nanopatterning, stacking two layers of graphene, or applying a bias voltage, all open a gap in the bandstructure.[16,33,34]

Near the Dirac points, as is seen in the enlarged figure on the right, energy is linearly dependent on the wavevector k. Behaviour of electrons are usually described by the Schrödinger equation. However, the Dirac points are so named because due to the linearity, electron behaviour is equivalent to the Dirac equation, where the electrons behave as if they move relativistically and without are mass.[14]
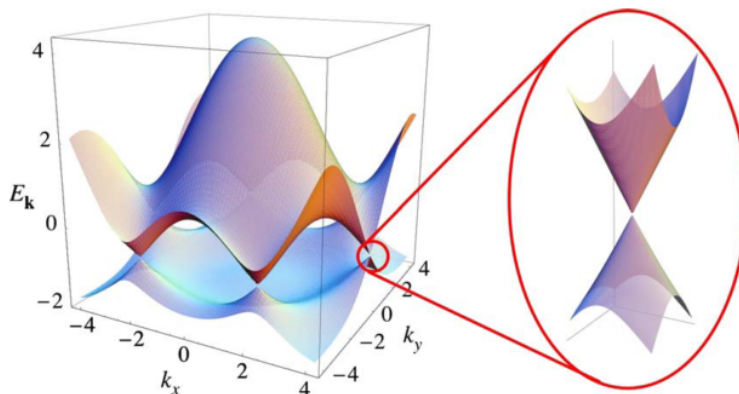
Figure 2.2: Band structure of graphene.[14] Note the hexagonal symmetry in the k_x-k_y plane, by 60° rotation, and that the bands are connected at six Dirac points, one of which is enlarged on the right.

This unique behaviour of the electron gives the material notably good electrical properties and a series of uncommon electrical and quantum electrodynamical effects.[4] As the electrons easily move through the materials this gives an uncommonly high electron mobility, theoretically limited at 200000 $\text{cm}^2\text{V}^{-1}\text{s}^{-1}$ due to intrinsical electron-acoustic phonon scattering. In comparison, Si has a mobility of 1400 $\text{cm}^2\text{V}^{-1}\text{s}^{-1}$, and GaAs 8500 $\text{cm}^2\text{V}^{-1}\text{s}^{-1}$. However, this is in practice limited to lower values if graphene in on a substrate, because of scattering due to interaction with the substrate.[35] The ideal mobility has been realized in suspended graphene,[36] while a mobility of about 63000 $\text{cm}^2\text{V}^{-1}\text{s}^{-1}$ has been realized in graphene on h-BN.[37] This gives the material a good conductivity, sometimes even better than silver, and thus a wide potential of electrical applications. Much research is directed into utilizing the good electrical properties at nanoscale for future nanoelectronic devices, as graphene is a good candidate for making smaller and faster transistors than used in today's technology.[38,39]

Another consequence of the unusual band structure is the special optical properties of graphene. A monolayer of graphene absorbs a constant 2.3% of light passing through it, largely independent of wavelength in the ultraviolet-to-infrared part of the spectrum.[40,41] A monolayer is thus highly transparent, with a slight purple colour. But the very high opacity means graphene transmits only a small fraction of light at a thickness of 100 layers, and thus assumes a gray graphitic appearance. The high transparency combined with the high electrical conductance of few-layered graphene, makes the material a good candidate for replacing indium tin oxide as a transparent conductor in solar cells and touchscreens.[17,42,43] The high absorbance also makes it useful for making efficient photodetectors[44] as well as making detectors and cameras simultaneously detecting in UV to far-IR at room temperature, which is not possible with today's conventional materials.[45]

2D materials like graphene, hold the special property of having all its atoms on the surface, behaving like two surfaces with no bulk in between. This gives exceptionally high chemical reactivity and selectivity, making it a potential material for future catalysis and membrane systems.[5,46] For example, graphene-based membranes have been shown to be highly efficient at liquid phase separation like water filtration and desalination,[6,47,48] while functionalization of the surface can give high selectivity, e.g. for extracting arsenic.[49]

2.2 Synthesis of Graphene

A monolayer of graphene was first isolated and characterized by mechanical exfoliation from crystalline graphite by Novoselov and Geim in 2004.[2] This technique, popularly known as the "Scotch Tape" method, consists of repeatedly exfoliating multiple layers from the graphite using sticky tape. After many exfoliations micrometer sized flakes of mono- and few-layered graphene can eventually be found amongst thin flakes of graphite. This method produces layers of high crystalline quality and can also be used for exfoliating other 2D-materials from their 3D-layered crystals,[50,51] and is useful for demonstrating devices based on these materials.[52,53]

While mechanical exfoliation is suitable for research and laboratory prototyping, applying 2D materials on industrial scale requires large quantities of monolayers have to be produced. Multiple techniques have been developed to exfoliate large volumes of graphite to graphene by dispersing it in a liquid phase. A typical method is chemically oxidizing graphite to graphite oxide, dispersing it in a solvent as graphene oxide.[54,55] Such dispersions can be filtered to a paper-like material, largely preserving the good monolayer mechanical properties in a 3D material.[56] However, graphene oxide is electrically insulating requiring chemical or thermal reduction to partially regain the good electrical properties of graphene.[57] To avoid the deteriorating effect the redox reactions has on graphene's electrical conduction, graphite can also be directly shear exfoliated in liquid using a blender.[18]

The size of graphene flakes produced by liquid phase methods are limited to the size of the initial graphite grains, meaning µm to mm sized flakes. These dispersions are also unsuitable to produce homogeneous and continuous large-area thin films with monolayer to few-nanometer thickness. Such thin films can be produced fron SiC by sublimating Si at high temperature and low pressure, leaving excess carbon to form a high quality thin film of mono- to few-layered graphene at the surface of the material.[58]

2.2.1 Chemical Vapour Deposition

In this work, thermal chemical vapour deposition (CVD), a more common approach than the previously mentioned, is used to grow graphene monolayers. CVD is popular because it is simple and cheap relative to other thin film techniques, and therefore also used extensively in industry. CVD is performed in a temperature controlled chamber (typically 500 - 1100°C) at ambient pressure with a controlled atmosphere (e.g. inert Ar gas), or low vacuum. A gaseous carbon precursor, typically CH_4, is introduced into the chamber whereupon contact with a catalytic metal substrate surface (typically Cu), it decomposes due to the high temperature, as per the equilibrium reaction:

$$CH_4(g) \longleftrightarrow C(s) + 2H_2(g) \tag{2.1}$$
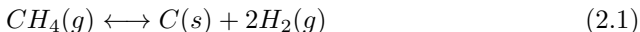
Where the C is deposited on the surface as adatoms, while H_2 and leftover CH_4 gas diffuse towards the gas outlet of the chamber. In addition to CH_4, H_2 gas is added to precisely control the equilibrium reaction. Depending on conditions at the surface (see section 2.2.1), the C adatoms either diffuse down into the catalyst metal or solidifies into amorphous carbon, carbon nanotubes, diamond, or as preferred here, graphene.

The graphene growth process is illustrated in figure 2.3a. Initially as the chamber is being heated, H_2 is supplied. During this high temperature annealing stage, H_2 reduces the surface oxide layer of the Cu foil to reveal a clean Cu surface. Then CH_4 is inlet causing an increasing concentration of C adatoms at the surface, which diffuse along the surface keeping the concentration even. At a critical level of supersaturation, stable nuclei of graphene forms at high surface energy sites of the Cu, typically edges and grain boundaries.[59] Nucleation and growth of the crystallites depletes the surrounding adatom carbon, hindering further nucleation. At this point, the growth continues as the C concentration is reduced until the surface adatoms, graphene and CH_4/H_2 are at equilibrium. Finally, the growth continues until the monolayer is complete or the reaction is stopped by ending the gas flow of CH_4, forming an incomplete layer.

The CVD equipment used in the present work is a Graphene Square thermal CVD system TA100 which is seen in figure 2.3b, and a schematic of it is given in figure 2.3c. The CVD consists of a quartz tube, into which the sample is inserted and placed in the center of the tube. The sealed tube can be pumped down to a pressure of $5 \cdot 10^{-4}$ torr, with operating pressure below 10 torr. H_2, CH_4 and Ar gases are let into the chamber, controlled by a mass flow controller so the partial pressures of the gases can be precisely controlled. N_2 gas is used to ventilate the chamber to ambient pressure after operation. During operation, the tube is heated by a resistively heating oven up to 1000°C. The oven, seen in blue in figure 2.3b, is in two parts that clamp around the tube. It is mounted on wheels so it can be moved away from the part of the tube containing the specimen, for rapid cooling after deposition.
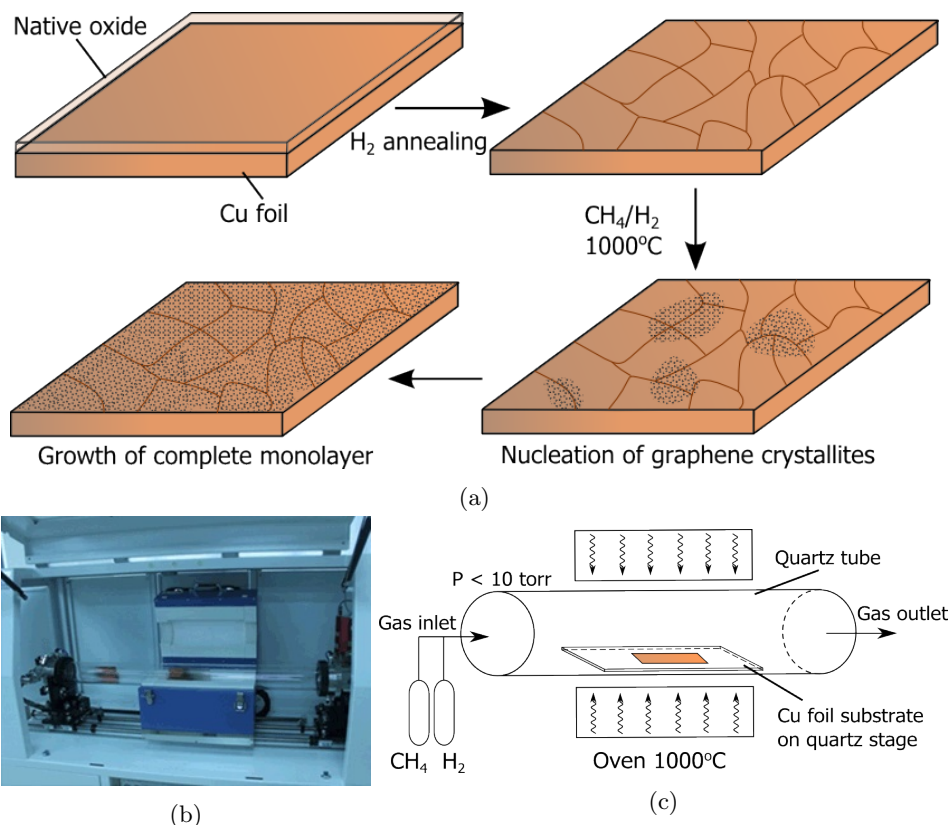
Figure 2.3: **(a)** CVD process of graphene. **(b)** Graphene Square thermal CVD system.[60] **(c)** Schematic of the CVD system.

CVD Growth Parameters

Parameters such as partial pressure of gases, temperature and surface features affects the behaviour of the carbon adatoms as they form graphene. Many applications of graphene rely on its high electrical mobility, which is limited by defects such as grain boundaries and wrinkles.[19,61] Optimally, CVD growth should therefore grow a continuous single-grain monolayer without growth of a second layer on top. This can be done by self-limited growth, where first a low nucleation density is promoted. And once initial nuclei have formed, growth dominates and nucleation of a second layer on top of graphene is energetically unfavourable. In this case growth ends once the whole surface of copper has been covered by graphene. Therefore control of nucleation density is essential for optimizing graphene growth.

The mechanics determining nucleation density is the competition between the rates of nucleus growth by C adatom capture, surface diffusion of C species, and desorption of C adatoms.[59] These rates are largely determined by the equilibrium in equation 2.1 and therefore the partial pressures of the inlet gases CH_4 and H_2.

CH_4 partial pressure act to increase initial C concentration on the surface, promoting nucleation, as well as growth rate after nucleation. To reduce nucleation density, a low CH_4 pressure is necessary, and gradually increasing the partial pressure during growth can increase growth rate without affecting nucleation density.[62] It is also important to keep a low CH_4 pressure to prevent the nucleation of additional layers, ensuring the growth is self-limiting.[63] Hydrogen partial pressure serves a dual purpose, first to reduce and clean the substrate surface. A high H_2 partial pressure also promotes the reverse of the reaction in equation 2.1, where H_2 combines with C adatoms on the surface to form CH_4.[64] This reduces the nucleation density, and also the growth rate. But very high H_2 pressure can also etch any graphene forming, stopping or reversing growth, as well as increasing the nucleation density..[62] The total background pressure also affect the reaction. Low pressure promotes self-terminating growth.[63] Low pressure also increases the high temperature evaporation of the metal surface, which further reduces nucleation density.[62]

A high temperature is also important, first to activate the dissociation of CH_4, but also to increase surface diffusion of C adatoms, to promote growth instead of nucleation, lowering nucleation density while increasing growth rate.[59] The temperature is best kept close to the melting point of the substrate, i.e. around $1000°C$ for Cu, to increase evaporation of the catalyst, reducing nucleation.[62] A high temperature near the melting point of the substrate also increases the solubility of C in the substrate, where some of the C adatoms will diffuse into the surface. During cooldown the dissolved carbon precipitates on the surface forming additional layers of graphene.[65] To prevent this, a substrate with low carbon solubility at high temperature is preferred.

The most commonly used substrate for graphene growth is polycrystalline Cu foil. Such a polycrystalline foil will from processing have surface roughness, grain boundary grooves, stepped terraces, as well as grains in different orientations, all which affects the growth mechanics and acting as nucleation sites, increase nucleation density.[59] It has been shown that Cu(100) surfaces have a higher nucleation density than Cu(111).[66] These surface features are affected by the high temperature annealing before growth, which will increase grain size by inducing grain growth, smooth surface roughness, and promote transformation of high energy facets like (100) to low energy (111). Notably, roughnesses such as scratches have been observed to form nanoparticles after annealing, which also acted as nucleation sites for graphene.[67] Overall, surface features should be smoothed and a large grain size is preferred. Ideally, the substrate should have a smooth monocrystalline surface.

A summary of parameters effecting graphene growth is given in table 2.1.

Table 2.1: Summary of parameter optimization for reducing nucleation density

Partial pressure of CH_4	Minimize
Partial pressure of H_2	Maximize
Total background pressure	Minimize
Temperature	Maximize
Substrate surface roughness	Minimize
Substrate grain size	Maximize

2.2.2 Substrate Materials and Transfer

As previously mentioned in section 2.1, the substrate material is important for the electrical properties of graphene, but it is also very important for CVD growth. Most research has been focused on CVD on transition metal substrates, for their catalytic properties. Early CVD graphene growth used Ni substrates, however this mostly gave few-layered graphene, as Ni has a high solubility of C at high temperature.[68,69] The dissolved C precipitates as additional graphene upon cooldown, making growing monolayers difficult.[65] Due to its very low solubility of C, Cu foils were found to be suitable as a substrate.[70] It has since been the most popular substrate for CVD growth of graphene. Another benefit of Cu compared to Ni is the weak substrate-graphene interaction, which enables graphene grains to grow over surface features, where for Ni, such features gives nucleation sites.[63]

However, for most applications of CVD grown graphene, utilizing its electrical properties cannot be done if the material is on a metal substrate, it must be on a semiconducting or insulating substrate. This issue is usually remedied by transferring the graphene from the metallic substrate to a useful substrate, e.g. a Si wafer. This is most easily done by floating the substrate in an etchant bath (e.g. $Fe(NO_3)_3$ for Cu), leaving the graphene floating on the surface, to be scooped up by the new substrate. However, this process is problematic as it introduces cracks, wrinkles and folds in the graphene, all deteriorating its electrical properties, as well as contaminates it with metallic nanoparticles.[71] Many alternative techniques have been developed.[23,37,72,73,74] These typically involve spin coating the graphene with a polymer like PMMA or PDMS, transfer onto a substrate, then dissolve the polymer with acetone. But this leaves the graphene polymer contaminated, which also deteriorates its electrical properties, and it has proven difficult to clean it properly.[75] An additional technique that avoids many of these problems are demonstrated by Ismach et al.,[24] where before CVD a thin film of Cu is grown on Si, which is evaporated after CVD, leaving graphene on the Si. This method is attempted replicated in this work.

2.3 Scanning Electron Microscopy

In scanning electron microscopy (SEM) an image is formed from signal created by a focused beam of accelerated electrons scanned across the specimen. The beam is emitted from an electron gun, and is focused using electromagnetic lenses, then scanned using electromagnetic scan coils in a raster pattern across the specimen. Various signals emitted from the surface can be simultaneously detected and processed into an image.

2.3.1 Components

The SEM used in this work, a Hitachi S-5500 FE-SEM, is shown in figure 2.4a. This model is unusual in that is can also operate in scanning transmission electron microscopy (STEM) mode (see section 2.4 for details about TEM).

The electron emitter is made out of W or LaB_6 (thermoionic filaments), or a field emission tip, the latter giving a narrower and brighter beam. in the S-5500 a field emission gun (FEG) is used. This tip is held at several negative kilovolt (0.5 - 30 kV), accelerating the electrons towards the positive anodes down the SEM column. The tip is enclosed in a cylinder of even higher negative voltage, concentrating the emitted electrons into a narrow beam downwards to the opening of the cylinder, towards the following lenses and specimen.

In optical microscopes light is focused by optical lenses. In comparison, in electron microscopes the electrons interact with a magnetic field in electromagnetic lenses, as given by the Lorentz force in equation 2.2:

$$\mathbf{F} = q(\mathbf{E} + \mathbf{v} \times \mathbf{B}) \tag{2.2}$$

Where $\mathbf{F}$ is force upon an electron, q is the electron charge, $\mathbf{E}$ is the electric field accelerating the electron, $\mathbf{v}$ is the velocity of the electron, and $\mathbf{B}$ is the magnetic field. The direction of the vectors are given by the right hand rule, and makes the electrons spiral through the beam in a helical trajectory. This magnetic field is generated by multiple electromagnets constructed radial symmetrically around the beam, where the field is lead by soft magnetic materials into polepieces separated by a short distance, thus creating a high magnetic field. This makes the lens work similar to a convex optical lens. The lenses are used for focusing electrons from the emitter into a narrow beam. In contrast to optical lenses where focus is changed by moving the lens up or down, in electronic lenses, the focus is shifted by changing the current through the electromagnets, changing the magnetic field.

The SEM has three different sets of lenses. First two condenser lenses that concentrates the beam from the gun into a narrow beam of parallel electrons. The third is an objective lens, and is used to focus the parallel beam into a narrow spot that strikes the surface of the specimen, hence controlling the focus. Above the objective lens, there are two sets of electromagnetic scan coils. These coils tilts

the beam and shifts it horizontally, and is used primarily for raster scanning the beam spot on the specimen, but also for shifting the image horizontally. The SEM also has two apertures, which are placed in the path of the beam, and are used for controlling convergence and divergence of the beam, and reduce aberration. The aperture limits the collection angle of a lens, affecting resolution (per Rayleigh's principle, see eq. 2.3), depth of field, depth of focus, image contrast, but also reduce the brightness somewhat. The first aperture is above the condenser lenses and reduces the divergence of the beam. The second aperture is above the scan coils above the objective lens, and blocks electrons that have diverged from the center of the beam, thereby reducing the negative effects of chromatic aberration in the system. The specimen is placed inside the objective lens, to have as short a working distance as possible, giving a high magnetic field from the lens focusing the beam into a narrow spot, enabling high resolution imaging.

As the beam strikes the specimen surface, different signals are produced (see section 2.3.3). These signals are detected by various detectors, as detailed in the S-5500 schematic in figure 2.4b. The system has a detector (SED) for secondary electrons (SE), above the objective lens and the specimen holder. This detector can also be used to detect backscattered electrons (BSE), using Hitachi's SE-BSE mixing technology, selecting a section of the emitted electrons (see figure 2.8). Below the specimen, there is a BF-STEM detector and a moveable ADF detector for imaging at different scattering angles (see section 2.4.4). The S-5500 used in this work also has an insertable in-lens YAG ring detector for BSE detection and an insertable EDX detector above the objective lens, that are not shown in the figure.

2.3.2 Resolution

The resolution in optical microscopes is limited by the wavelength of light, enabling imaging of details down to a few hundred nanometers, as per equation 2.3:

$$\delta = \frac{0.61 \cdot \lambda}{NA} \tag{2.3}$$

Where, δ is the smallest resolvable spacial detail, λ is the wavelength, and NA is the numerical aperture of the optical system. In comparison, SEMs are generally not limited in resolution by the wavelength of the emitted electrons. Magnification is given by the scan distances, with high magnification resulting from short scan distance. The resolution is therefore limited by the narrowness of the focused beam spot. The size of the spot is dependent on the electron-optical components, especially the objective lens and the wavelength. Optical systems has a high NA due to nearly perfectly shaped lenses, while NA is lower in electron microscopes, as it is more difficult to make optimal electromagnetic lenses. The de Broglie-wavelength of the electrons, as resulting of the acceleration voltage, is given in equation 2.4:

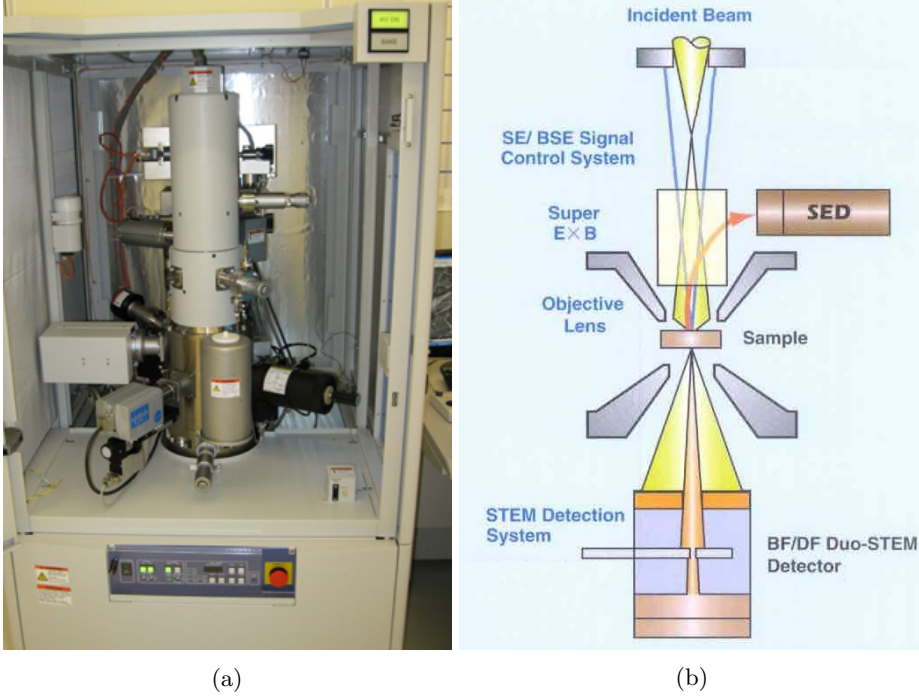$$\lambda = \frac{h}{p} = \frac{h}{\sqrt{2m_0 eV}} \tag{2.4}$$

Figure 2.4: **(a)** The Hitachi S-5500 FE-SEM.[76] **(b)** Schematics of the SEM, modified from Hitachi.[77]

Where λ is the de Broglie-wavelength, h is Planck's constant, p is the electron's momentum, m_0 is the rest electron mass, e is the electron charge, and V is the acceleration voltage. Values for the de Broglie-wavelength of the electrons at common acceleration voltages in a SEM (and in TEM) is given in table 2.2. As we see, compared to the wavelengths of visible light, the wavelength of the electrons are much shorter giving a higher magnification, typically around 1 nm, limited by other parameters than the wavelength. Note that high energy electron travel at speeds in the relativistic regime giving shorter wavelengths, so that above 100 kV, the wavelengths are noticeably shorter. The current highest resolution achieved without aberration correction is 0.4 nm at 30 kV in the Hitachi SU9000,[78] and 0.08 nm with correction in the Hitachi HD-2700C.[79]

Table 2.2: Non-relativistic de Broglie-wavelengths for electrons at common acceleration voltages in SEM and TEM.

Acceleration voltage [kV]:	0.5	1	5	15	30	80	120	200
de Broglie-wavelength [pm]:	54.9	38.9	17.3	10	7.08	4.34	3.54	2.72

2.3.3 Interaction

When the incident electron beam strikes the specimen material, various different signals are produced that can be interpreted for analysis of the material.[80] These signals are schematically illustrated in in figure 2.5a, where the interaction with the material cause emittance of both photons and electron signals from the surface. This is due to the incident electrons scattering both elastically and inelastically in various ways.

A small fraction of the primary electrons of the beam is, by repeated nearly elastic scattering by the atoms of the specimen material, deflected to a high angle of $> 90°$ compared to the optical axis, causing them to eject from the surface. These backscattered electrons (BSE) retains much of their high kinetic energy, and can be used for imaging of the specimen. The rest of the primary electrons are repeatedly inelastically scattered at small angles by the outer-shell electrons of the atoms, gradually loosing energy until they are eventually brought to rest. These electrons are absorbed into the material, and makes it necessary for the specimen material to be able to conduct the electrons away, otherwise charge will collect, eventually distorting the incident beam. This is known as charge-up, and is a significant problem with high resolution imaging of samples with low conductivity, e.g. organic and ceramic materials. The energy absorbed by the atoms by inelastic scattering is released as photons, mostly X-ray bremsstrahlung, but also characteristic X-rays and for some materials UV and visible wavelengths (cathodoluminescence), that correspond to interband transitions of excited electrons in the atoms of the material. This characteristic radiation can be analysed for chemical information of the sample (see EDX, section 2.3.5).

Additionally, electron excitation (from both inelastic scattering of electrons and X-rays photoelectrons) ionizes atoms, releasing low-energy electrons generally called secondary electrons (SE), that in turn are scattered. Most of these fall to rest and are absorbed again, but SE very close to the surface are often ejected from the specimen. The SE can also be caused by ejected BSE. There are three types of SE signals; from the primary beam (SE1), from the BSE as they are leaving the surface (SE2) and BSE striking other surfaces in the SEM chamber (SE3). The SE1 are ejected from a small volume close (< 50 nm) to the surface where the incident beam strikes. Therefore, this signal is suited for high resolution imaging using an in-lens detector, as in the present study. If the SE is emitted from an inner shell of the atom, a third outer electron will relax into the inner shell, releasing energy. This energy is usually emitted as a characteristic X-ray, but if sufficiently energetic, a fourth electron (Auger electron) can be excited from the outer shell, ejecting from the atom. Its energy correspond to the energy difference of the relaxed third electron, making Auger electrons (AE) SE with characteristic energy, also suitable for spectroscopic detection of chemical information of the material. However, AE can only be detected from very near the surface (< 10 Å), requiring the surfaces to be cleaned inside the vacuum, and is thus typically used in a dedicated Auger-electron spectroscopy (AES) system.

Most of the different signals are absorbed into the sample, but for analysis by detectors, the signals have to escape the surface. The pear-shaped volume around the primary beam from where the signals can escape, varies for each signal as shown in figure 2.5b. The low energy Auger electrons and secondary electrons are typically emitted from down to a depth up to 1 nanometer and a few nanometers, respectively. These width of these volumes are about as narrow as the primary beam, enabling imaging with a resolution determined by the narrowness of the beam, down to below 1 nm. In comparison, the volume from which backscattered electrons and X-rays escape goes much deeper (down to hundreds of nanometers) and is much wider, due to the comparatively higher energy of the BSEs and the lower absorption of X-rays in the material. This results in the resolution being lower with typically below 10 nm for BSE and above 10 nm for EDX.

The size of the escape volumes and penetration depth also greatly depends on two additional factors, the atomic number (Z) of the material and the energy of the primary electrons (E_0), as shown in figure 2.6. Heavier atoms scatter more than lighter atoms, reducing the volume. High energy primary electrons retains higher energy deeper into the material, and thus cause emittance of signals with high enough energy to escape at lower depths, therefore increasing the escape volume.
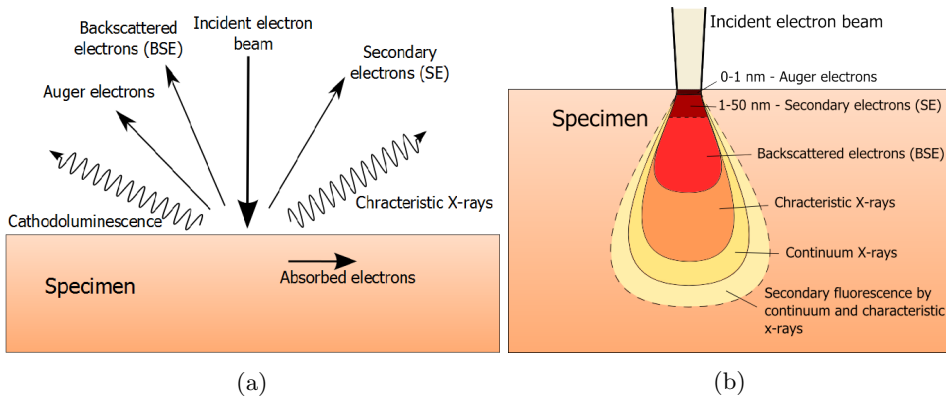

Figure 2.5: **(a)** Illustration of signals coming from a beam in SEM. **(b)** The electron beam specimen interaction volume for the various signals in a SEM.
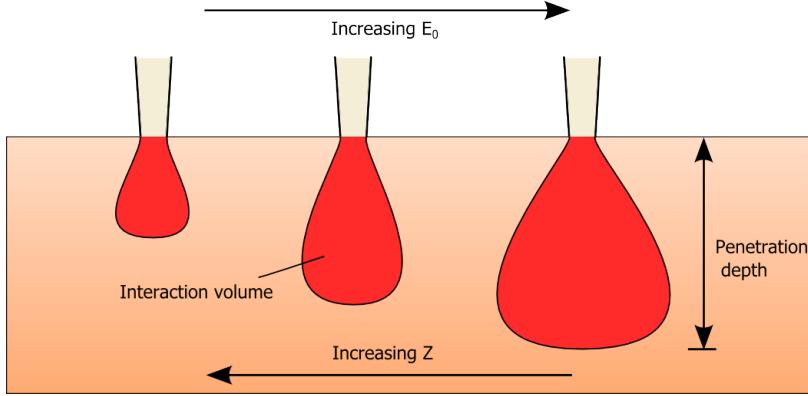
Figure 2.6: While high energy (E_0) electrons increase the interaction volume, higher atomic number (Z) material reduces it.

2.3.4 SEM Techniques

Secondary Electron Imaging

As mentioned, SE are most commonly used for SEM imaging due to high resolution, caused by SEs ejected as a strong signal from a shallow depth below the surface in a small escape volume. Comparing the SE signal to BSE and AE in figure 2.7a, we see that the SE have a very low energy, < 50 eV, but a much higher yield, as one electron in the primary beam can often produce more than one secondary electron. The low energy also makes it easy to attract the electrons to a detector by applying a positive bias, so that the detector can be placed very close to the specimen surface giving a clear signal. The S-5500 has an in-lens detector, seen as SED in figure 2.4b. as compared to a conventional Everhart Thornley-detector placed farther away from the sample, that also collects SE2 and SE3.

An important feature of SE imaging is the high topological contrast. The low penetration depth depth of the SEs results in the amount electrons escaping being very sensitive of edges and other topological features, as illustrated in figure 2.7b. For such features, more electrons escape giving a very bright signal compared to flat areas of the specimen. This contrast increases at lower acceleration voltage, due to the reduced penetration depth, so topological resolution below 1 nm can be achieved sacrificing lateral resolution. Imaging with very low voltage electrons (10 - 50 V), a technique called low energy electron microscopy, enables Ångström-topological resolution, with contrast between individual atomic layers. For imaging of graphene, being a monolayer material, this contrast is obviously important, so imaging at very low voltage is useful. This has been utilized successfully to study the formation of monolayer graphene and other 2D materials.[81,82,83,84] Note that carbon, being atomic number 6 scatters little, reducing this contrast.
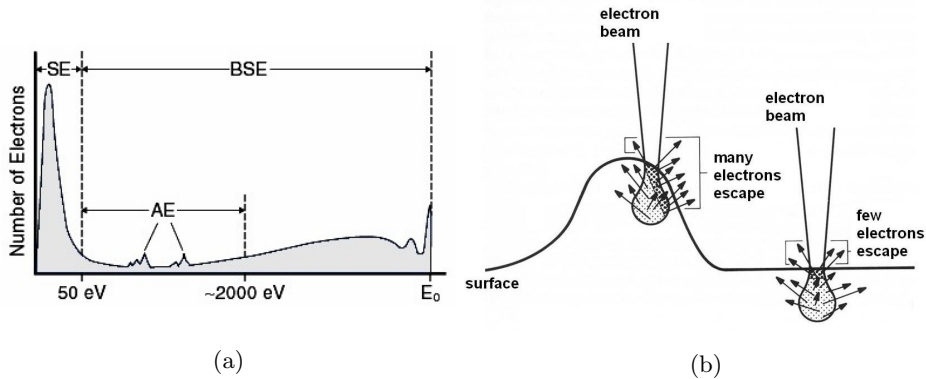
Figure 2.7: **(a)** Comparison of signals from an edge and on a flat surface, where the increased escape of electrons from a surface causes topological contrast.[85] **(b)** Energy spectra of the electron signals in a SEM, SE has a strong signal at < 50 eV, Auger electrons (AE) give weak but distinct peaks < 2000 eV, and BSE signal form over a large energy range, but give the strongest signal > 2000 eV.[86]

Backscattered Electron Imaging

Compared to SE, BSE imaging has a lower resolution of about one order of magnitude, due to the larger escape volume, and thus wider area around the beam where the BSEs are ejected from the surface, as illustrated in figure 2.5b. Also, as compared in figure 2.7a, the BSE has a much weaker signal with a higher energy spread out over a wide energy distribution. Therefore BSE imaging is best done at high acceleration voltage to increase the yield of the signal. However, the high energy of the BSE reduces the possibility of attracting the electrons to the detector by a positive bias voltage, limiting the signal intensity. The most important feature of the BSE signal is its high contrast for the atomic number (Z) of atoms in the specimen. This is due to increased backscattering in heavier elements giving a brighter signal. Good topological contrast can also be achieved by using an asymmetrical detector, giving a shadow-like contrast, however the edge contrast is less bright than for SE.

In the S-5500 used in this work there is also an imaging mode for detection of low-angle backscattered electrons (LA-BSE) by the detector for SE. In this mode, BSEs of relatively low energy are decelerated by electrodes in the objective lens, then attracted to the positively biased SE detector, as shown in figure 2.8. By altering the voltage at deceleration electrodes the SE and BSE signals can be mixed ranging from completely SE to completely BSE. Also notable is that this BSE mode has got a high signal yield also at low acceleration voltage of the primary beam.
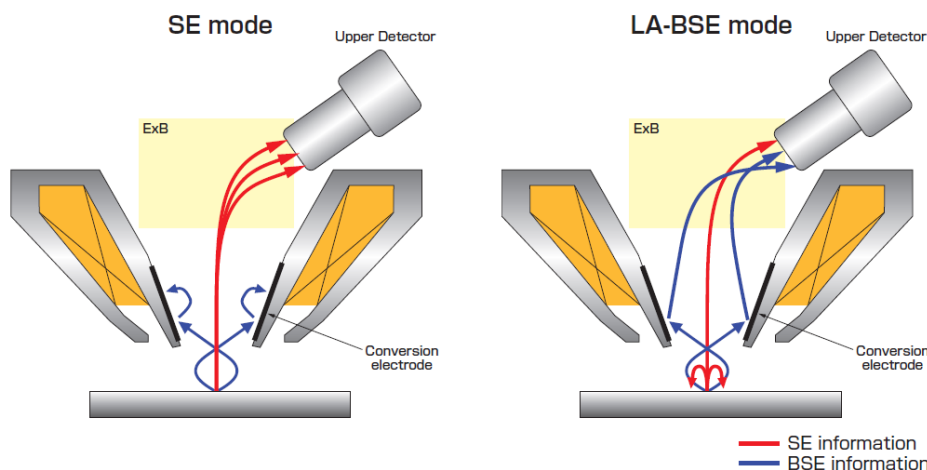
17

Figure 2.8: Detection of SE or LA-BSE, by SE-BSE mixing in the Hitachi S-5500.[87]

2.3.5 Energy-dispersive X-ray Spectroscopy

Energy-dispersive X-ray Spectroscopy (EDX) is an analytical technique for identifying elements in the specimen by recognition of characteristic signals in the X-rays emitted from the sample. As previously mentioned, a background signal of bremsstrahlung X-rays is emitted due to absorption of energy from inelastic scattering of primary electrons. Additionally, if an electron in an atom's inner shell is exited, the following relaxation from a different band causes the emission of X-rays which have specific energy corresponding to the difference in energy between the bands. This gives a series of distinct signals that are unique for the different elements, giving characteristic sets of peak in a measured X-ray spectrum.

The spectrum can be found by using an energy-dispersive spectrometer that counts ionization of atoms by absorbing the X-rays, causing electron-hole pairs. The number of electron-hole pairs is related to the energy of the incoming X-ray into the detector. Such a detector is typically added to a SEM or TEM system as an insertable detector above the specimen. Being inserted from the side, this position is often asymmetrical with regards to the center of the beam. This leads to a shadow-like effect, where surfaces pointing towards the spectrometer give a much stronger signal, as the X-rays are emitted directly towards the spectrometer instead of in other directions. This is especially for low energy X-rays that can easily be absorbed before counted.

Example of an acquired spectrum is seen in figure 2.9, where we see that there are multiple peaks corresponding to different energies for various elements. Looking at the Cu peaks, we see that there are two large peaks to the right in the spectrum,

where the largest correspond to a transition between the $n = 2$ level in the p-orbital to $n = 1$ in the s-orbital, named K_α, and the smaller is the $n = 3$ in p to the $n = 1$, K_β. Additionally, there are also multiple overlapping Cu-peaks around 1 keV corresponding to the transitions between the three p-orbitals, L_α, L_β, L_γ. However, analysing the EDX spectra is not always straight forward, as the peaks can be wrongly labelled. In the used EDX-SEM there was a set of peaks around 3.5 keV that are wrongly recognized as In, but in reality are reflections at double the energy of the peaks around 1.5 keV. Also, some elements can be difficult to detect, e.g. low atomic number elements like C which give weak signals that are difficult to distinguish from other low energy signals, but in this case is detected due to large amounts of carbon. Signals also come from other surfaces that are not in the scanned image, e.g. Fe-peaks are also typically present due to the signal from steel surfaces in the chamber, here giving the unmarked peak at 8.5 keV, while the Cu signal come from the Cu TEM grid.

The spectrometer can, additionally to measuring of an average spectra of the imaging area, also be used for line scanning and elemental mapping of an area of the surface. This is done by analysing the spectra while the beam if scanning, identifying e.g. different particles or phases of the specimen. The resolution for such mapping is however, much lower than for SE or BSE imaging. This is due to the comparatively much wider escape volume of the X-rays, as seen in figure 2.5b, typically giving a resolution around 10 nm. This can be less of a problem in TEM specimen with a thickness less that the penetration depth, resulting in emission only from a shallower depth of the escape volume that is less wide, hence higher resolution. By comparing the intensity of the different signals, quantification of the elements can also be done, but this is often not very exact.
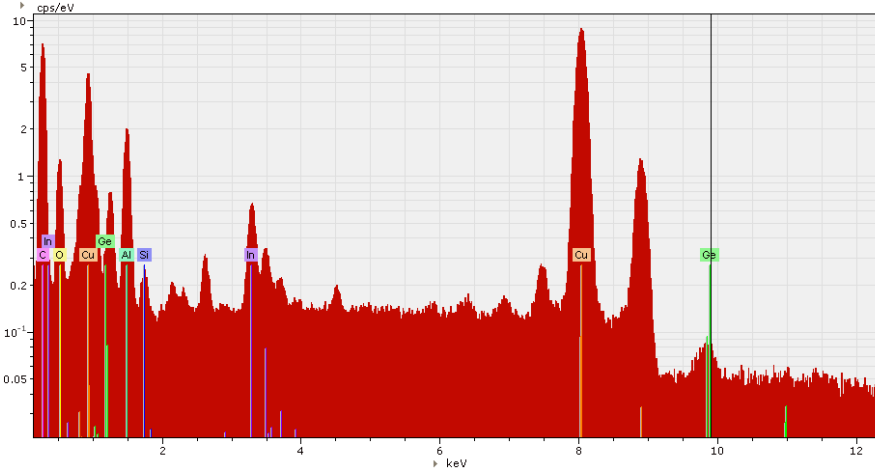

Figure 2.9: Sample EDX spectra from the S-5500, of a sample of graphene on Si and Ge, on a carbon film covered Cu TEM grid.

2.4 Transmission Electron Microscopy

In transmission electron microscopy (TEM), an image is formed from a beam of accelerated electrons (80 - 400 kV), passing through a thin sample (typically < 100 nm).[88] This invention from 1931 resulted in the Nobel prize in physics for Ernst Ruska in 1986. The technique is analogue to transmission optical microscopy, in that a beam passes through the sample, forming an image. The system is similar to a SEM in that generally the same components are used, only TEMs are generally more complex, with additional and stronger lenses, can achieve a higher resolution, and obtain highly detailed crystallographic information in diffraction mode. In regular TEM mode, the beam is not scanned, but a focused beam can also be operated in scanning transmission electron microscopy mode (STEM).

2.4.1 Components

The TEM mostly used in this work in the JEOL 2100 JEM shown in figure 2.10a, with its schematic illustrated in figure 2.10b. TEMs use the same type of guns as SEMs, and this 2100 has got a LaB_6 thermoionic gun, while the JEOL JEM-ARM200F also used, has got a field emitter gun.

The TEMs have three condenser lenses and one mini lens, used to condense the beam from the gun and guide the beam into striking the sample in two different modes. A parallel beam, where the electrons move approximately parallel to each other, is used for bright-field (BF) and dark-field (DF) imaging, and selected-area diffraction (SAD). A convergent beam, where the electrons are focused into a spot of as narrow diameter as possible, is used for STEM, convergent beam electron diffraction (CBED), energy-dispersive X-ray spectroscopy (EDX), and electron energy loss spectroscopy (EELS). Scan coils before the specimen stage enables tilting and translation of the beam, used in STEM and centred dark-field.

Apertures are placed in the optical path, and are used for controlling convergence and divergence of the beam, reduce aberration, and selecting beams (scattering angles), giving different images and diffraction patterns. The aperture limits the collection angle, β of a lens, controlling resolution (through Rayleigh's principle), depth of field, depth of focus, image contrast, angular resolution of DP and the collection angle of EELS. The TEMs have three apertures, the condenser aperture below the condenser lens, the objective aperture, in the back focal plane in the lower polepiece of the objective lens, and the selected area (SA) aperture in an image plane within the intermediate lens system. The SA aperture can limit the area of the specimen from which a diffraction pattern is taken (to area of ca. 100 nm due to mistilt of the beam and spherical aberrations).

There are one objective lens and a mini lens, which are the most important lenses as they form the image and diffraction pattern. For optimal magnification, the specimen must be as close to the plane of the lens as possible, and is thus placed

in-lens. The objective lens is very strong and is made of two separated polepieces to make room for the specimen holder and an aperture in between, see figure 2.10b. Both the condenser lenses and the objective lens is used for controlling the magnification, but the objective lens is the most important.
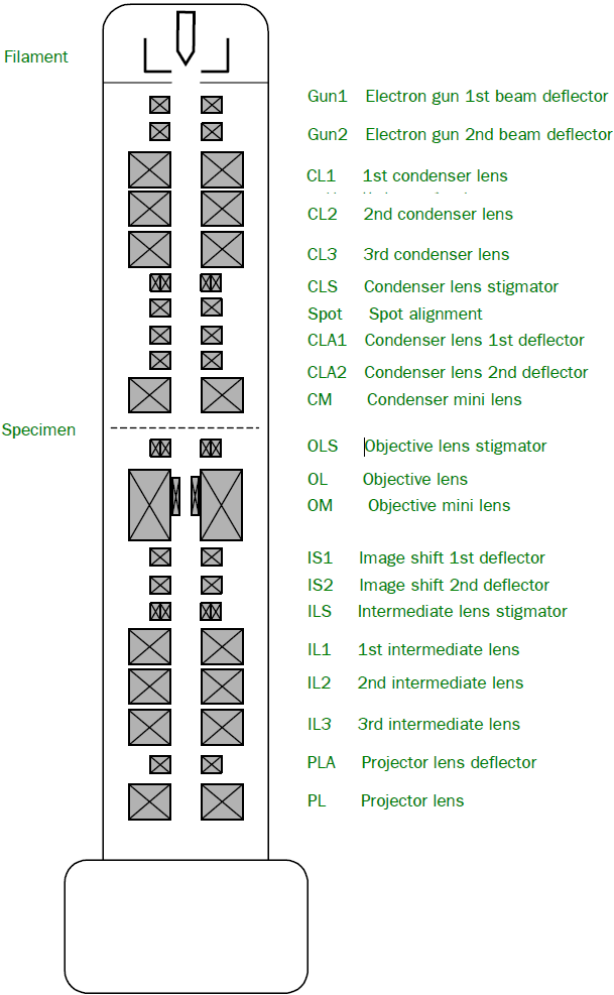
Figure 2.10: **(a)** The JEOL 2100 JEM used for material characterization (modified from Gemeni Center[89]). **(b)** Schematic of a TEM (from JEOL 2100 Instruction Manual[90]).

To insert specimen into a TEM, special specimen holders are used, that are inserted into the goniometer passing the sample through airlocks, into the object lens in the high vacuum chamber. These holders hold one or more of the 3 mm diameter ring supports of metal (typically Cu) with the specimen on it, and the holder features piezoelectric control in xyz-directions and tilting angles alpha & beta relative to the incoming beam. Above the specimen, an insertable EDX detector is mounted.

To see the image formed by the electron beam after the objective lens, three intermediate lenses and one projection lens are used to form the image onto a ZnS viewing screen. The intermediate lenses are also used to select projecting either the image or the diffraction pattern. ZnS is fluorescent, meaning incident electrons make the screen glow of visible wavelengths of light, usually $450 - 550$ nm, and the viewing screen is view through leaded glass that blocks X-rays. For acquiring a digital image, high resolution CCD detectors are nowadays used to detect and record the image of the electron beam directly. The viewing screen can also be opened, to let the beam be detected by the EELS mounted at the bottom of the microscope.

To tilt and deflect the beam, there are sets of deflection coils above and below the condenser lenses, and above and below the intermediate lenses. In STEM mode, the condenser lens deflectors are used for scanning the focused beam. All the sets of lenses, except the projection lens, have got stigmators to correct astigmatism from imperfections in the lenses.

High vacuum is required in a TEM to allow electrons passing a distance of more than a meter (from the gun to the screen) unhindered through the column. For such a long mean free path, a vacuum higher than 10^{-4} Pa is required. This requires at least two stages of pumping, first a mechanical roughing pump down to a low vacuum of 10^{-3} Pa, followed by a one or more of turbo-, cryo-, diffusion or ion pumps to get a high vacuum. Typically, different sections require different pressure, e.g. if the TEM has a FEG, which requires a UHV closer to 10^{-7} Pa for operation.

2.4.2 Resolution

Compared to optical microscopes, TEMs are not limited in resolution by the wavelength of visible light. In an optical microscope, it is possible to image details down to a few hundred nanometers, while in a TEM, the de Broglie-wavelength (see equation 2.4) of the electrons is given by the acceleration voltage of the electron source, and as we see from table 2.2, the wavelengths are far shorter than the diameter of atoms ($\sim$1 Å).

The point-to-point resolution of a TEM is typically around 2 Å at 200 kV, though new models with aberration correction image at down to below 0.05 nm resolution. When imaging in bright-field mode, the resolution is determined by the objective lens' ability to image the object. If the resolution is higher than the interatomic distances in the crystal lattice of the sample, the structure of the lattice itself can also be seen, and it is also possible to see lattice fringes (see section 2.4.5).

The electromagnetic lenses have positive spherical aberration because of electrons closer to the centre being deflected less than electrons closer to the magnet, due to the magnetic field being stronger close to the magnets. This is especially problematic in the objective lens, as the lenses below magnifies the aberration from this lens. This limits the cross section area of the image plane of least confusion to a disk with radius given in equation 2.5:

$$r_{sph} = C_s \beta^3 \tag{2.5}$$

Where r_{sph} is the radius of the disk, C_s is the aberration correction, and β is the collection angle. Spherical aberration is typically limiting the resolution for samples with a thickness of a few nanometers or below. This problem can be reduced by modern aberration correction systems.

Chromatic aberration of the image is due to electrons of different energy, being diffracted unevenly by a lens. Lower energy electrons are diffracted more than high energy electrons, making it more difficult to focus the beam, widening the plane of least confusion. This is given by equation 2.6:

$$r_{chr} = C_c \beta \frac{\Delta E}{E_0} \tag{2.6}$$

Where r_{chr} is the radius of the disk of least confusion, C_c is the aberration correction, ΔE is the energy difference, E_0 is the average electron energy. The difference in energy originates from the electron gun, where the energy difference of the beam varies around about 0.3 eV for cold FEGs and about 1.5 eV for LaB_6. This aberration can be reduced by filtering electrons of different energies by an aperture. Chromatic aberration is typically limiting resolution if the sample is thick, as spread in energy is introduced from inelastic scattering by electrons colliding with the sample, thus loosing some energy. Lenses below the specimen then cause aberration of the beam. Because of this, having very thin samples are required to get as good resolution as possible.

Imperfect radial symmetry of the electromagnetic lenses causes an asymmetrical magnetic field (astigmatism) in the lenses. This asymmetry is due to manufacturing imperfections. This astigmatism can be easily be compensated for by the operator, using stigmator coils. For the best imaging quality, stigmation in the objective lens system is most crucial, where in focused beam techniques the condenser system stigmation is determinant.

In practice, the highest possible resolution is limited by spherical aberration, which combined with the Rayleigh criteria gives equation 2.7:

$$r_{min} = 0.91(C_s\lambda^3)^{1/4} \tag{2.7}$$

2.4.3 Interaction

The same signals as in SEM (section 2.3.3) are also generated by the beam interacting with the specimen in a TEM, but more importantly due to the thinness of the sample (< 100 nm), most of the electrons pass through without scattering. But there are also additional signals emitted from the bottom of the sample from the beam scattering both elastically and inelastically, as seen in figure 2.11. Cathodoluminescence, Auger electrons, BSE, SE, and bremsstrahlung X-rays, are not analysed in conventional TEM, where the two scatted transmitted signals are the most important. The BF image is contained in the transmitted electrons wave, while the DP is given by the elastically diffracted beams. DF is seen by excluding the center beam, looking at the electron wave in one or more of the elastically diffracted beams.

Additionally, due to the thin specimen studied in TEM combined with the high energy of the electrons, beam damage of the material can be very significant in TEM. This knock-on damage (kind of sputtering) happens at acceleration voltage > 50 kV, so is not apparent in SEM. The rate of damage increases with higher voltage and the electron density of the beam, so the damage happens rapidly at high magnification. The rate is also material specific. The damage can turn crystals amorphous and increases the rate of diffusion of species on surfaces and defects within the material. For graphene, being a monolayer, this rapidly creates holes in the material and eventually rips it apart. For perfect graphene, the knock-on damage threshold is ca 90 kV.[91] Note that radiolysis and melting can happen.
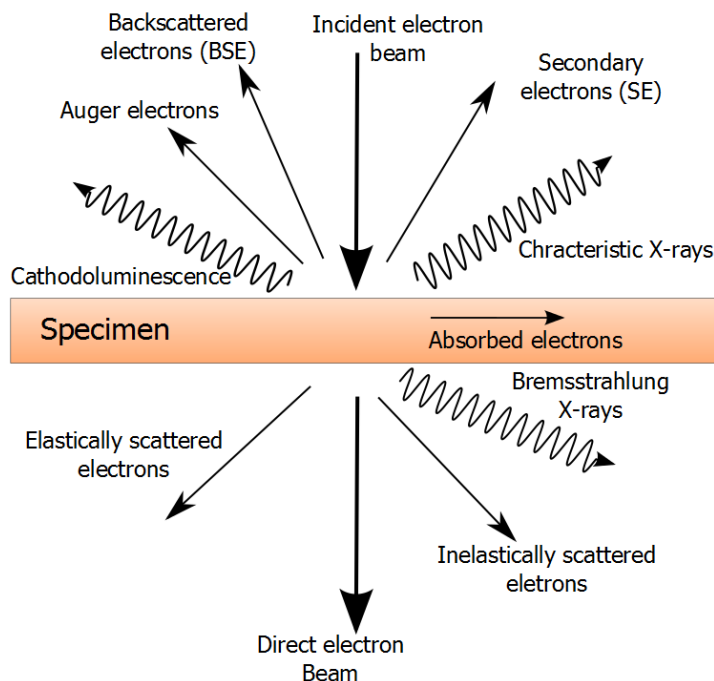
Figure 2.11: Different signals resulting from the electron beam interacting with the specimen in a TEM.

2.4.4 TEM Techniques

Bright Field Imaging

Bright field (BF) is the standard imaging technique in TEM. In this mode, a parallel beam is used and all the transmitted signals used to form the image, but most of the information comes from the direct beam. The intermediate lens is adjusted to so the image plane of the objective lens is in the object plane is the intermediate lens, and thus is projected onto the viewing screen. An objective aperture can also be placed at the focal distance of the objective lens, the back focal plane (BFP), to increase the imaging contrast. A ray diagram of this setup is shown to the right in figure 2.12. Here we see that the projected final image is a magnified of the image formed at the intermediate image plane 1. The contrast in BF is due to both mass-thickness and diffraction contrast (see section 2.4.5).
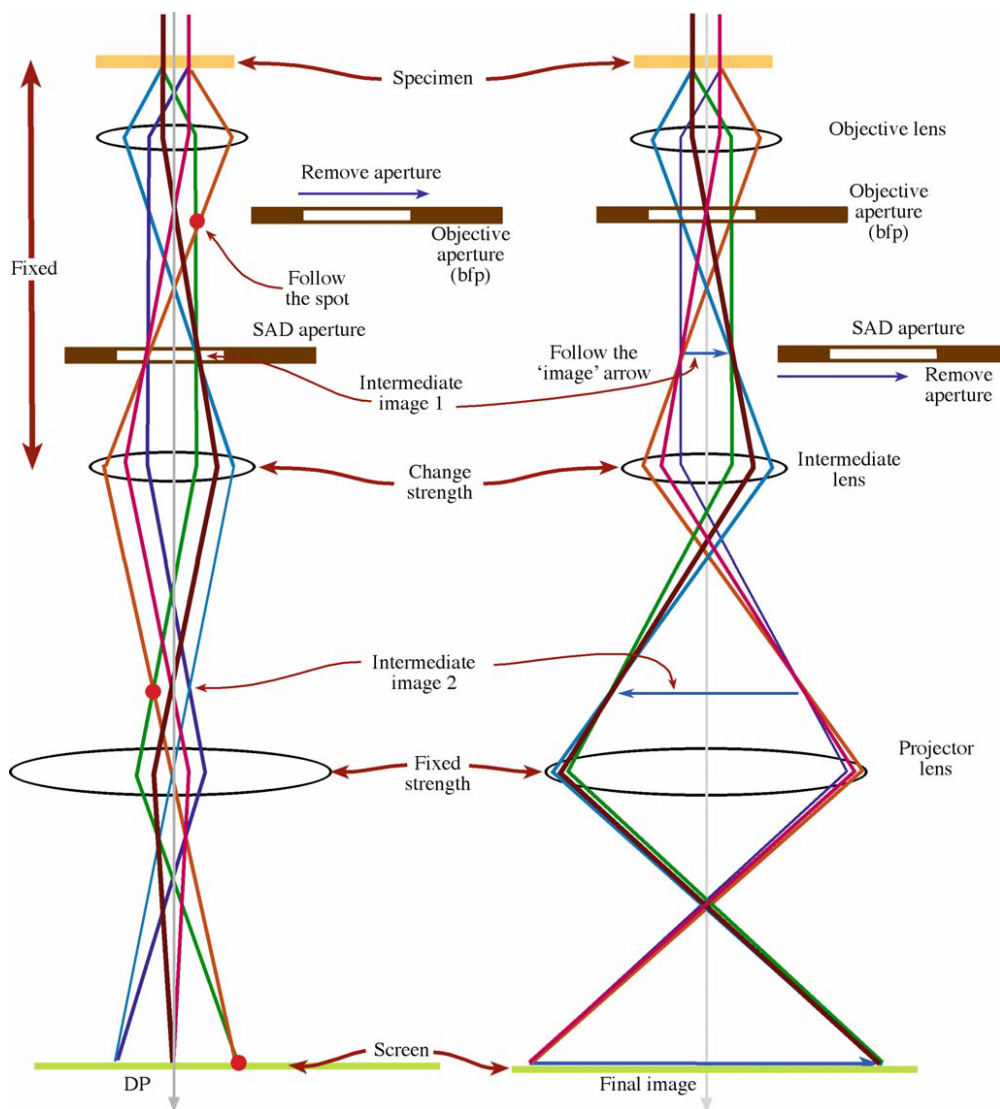
Figure 2.12: Ray diagrams for TEM operation in DP (left) and BF (right) modes, from Williams and Carter.[88]

Selected Area Diffraction Pattern

In the TEM, diffraction patterns (DP) appear in the BFP. This is due to atoms ordered in a crystal structure interacting with the electrons like a diffraction grating, resulting in diffraction spots in the BFP that are a projection of the reciprocal lattice of the crystal. The individual spots correspond to hkl-planes in the crystal structure oriented at Bragg angles, as per Bragg's law in equation 2.8:

$$\frac{2sin\theta_B}{\lambda} = \frac{n}{d_{hkl}} = |\mathbf{K}| \tag{2.8}$$

Where θ_B corresponds to the Bragg angles, λ is the wavelength of the electrons, n is an integer, d_{hkl} is the interplane distance of any plane hkl, $\mathbf{K}$ is the difference of the wave vector of the incident wave and the diffracted wave $\mathbf{K} = \mathbf{k}_D - \mathbf{k}_l$.

Diffraction patterns give information about the crystallinity, grain morphology and size, crystal structure, orientation and lattice parameter of the material. To see the DP you have to adjust the imaging-system lenses so that the BFP of the objective lens is projected onto the viewing screen. For selected area DP (SADP), a SA aperture is inserted in the intermediate image plane 1 to select an area of the sample, for example a single grain. SA is important due to specimen typically being polycrystalline or inhomogeneous at long ranges, so limiting the area gives simpler DPs that are easier to analyse. A ray diagram of this setup is shown to the left in figure 2.12. Here we see that the final projected image is magnified of the diffraction pattern formed in the BFP. A sample DP is given in figure 2.13. The direct beam is much more intense than the diffracted beams around, that comes from a hexagonal C lattice. Also seen are two amorphous rings of C, at a distance from the center that matches the six nearest and the six second nearest spots.
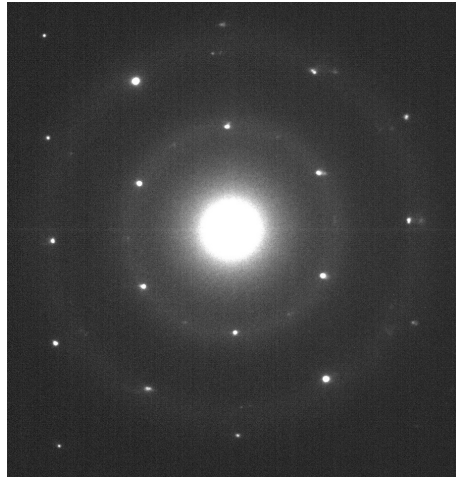

Figure 2.13: Sample DP of hexagonal many-layered graphene on amorphous lacey carbon.

Dark-field Imaging

Where the direct beam is used to form a BF image, for dark-field (DF) imaging, the direct beam is excluded, and one or more of the diffracted beams (see the DP in figure 2.13), are selected to form the image. The objective aperture is used for selecting beams for DF as shown in figure 2.14. Here we see that selecting the direct beam forms a BF image, and moving the objective aperture to an off axis diffracted beam forms a DF image. More commonly, the aperture is centred and the incident beam is tilted so that a diffracted beam is on the optical axis.

In BF, areas which scatter electrons become darker. In comparison, in DF the contrast in negative to BF, where the areas which diffract into the selected beam becomes bright and the rest is dark. This makes it possible to image areas with a specific crystal orientation. However, a problem with DF is that because only a small part of the beam is used to form the image, the amplitude of the signal is often very low, making it difficult to see on the viewing screen. In stead a long exposure time with the CCD can be used, often several minutes, but this can blur the image due to specimen drift, beam damage or diffusion in the sample.
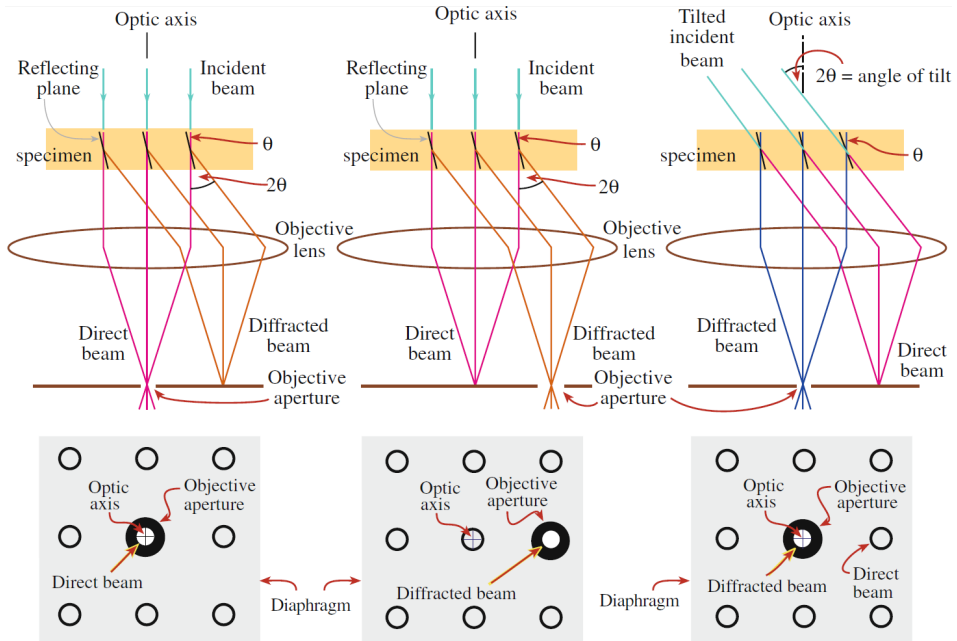

Figure 2.14: Ray diagrams illustrating the use of the objective aperture to select the direct beam for BF (left). Selecting a diffracted beam for DF by moving the objective aperture (center). Tilting a diffracted beam into the centred objective aperture for DF (right). The position of the objective aperture in the DP is shown below the ray diagrams. From Williams and Carter.[88]

Scanning TEM

Scanning transmission electron microscopy (STEM) is a technique where imaging is done by focusing the electrons into a narrow converging beam (probe), that is raster scanned across the surface using scan coils. A ray diagram for this is shown in figure 2.15a, where the condenser lenses are used to form the probe and the double condenser scan coils scans the probe while keeping it parallel to the optical axis. In contrast to TEM mode, no actual image is formed directly, but during scanning the intensity of the transmitted beam at a certain point (x,y) is measured by detectors (BF, annular DF (ADF) and high-angle ADF (HAADF)) placed in a plane conjugate to the BFP, where a DP is formed. A ray diagram for this is given in figure 2.15b, where the convergent probe is transmitted as a diverging cone detected as BF. Hollow cones of diffracted electrons gives rings in the DP that can be detected by a low-angle annular detector forming ADF, and high angles diffraction is detected with a HAADF detector. These detectors gives contrast depending on how much of the beam is scattered. The contrast of BF is essentially the same as in TEM mode. A comparison of a STEM-BF and an ADF image of the same sample is shown in figures 2.15c, 2.15d, where ADF has negative contrast of BF. Magnification is not determined by lenses as in TEM, but by the scan dimensions. The resolution is determined by the probe size (as formed by the lenses) and how high current can be focused in as small a probe as possible.

An advantage of STEM is that ADF and HAADF detectors enables the capture of more electrons compared to TEM-DF, due to DF being limited by the aperture size. Also, because the scattering at high angles is highly sensitive to the atomic number of the atoms, this enables high (atomic) resolution imaging with high Z-contrast (see 2.4.5). This technique allows simultaneous EELS and EDX measurements for the same pixels/specimen points. HAADF is also generally unaffected by small defocus and specimen thickness. Another advantage is that no lenses are used to form the image coming from the sample, reducing the aberrations, although aberrations from the gun and probe-forming lenses are still present. This makes HAADF generally the technique with the highest resolution.

High-resolution Imaging

High-resolution TEM (HRTEM) is not a distinct technique in itself, but is about applying phase contrast (see section 2.4.5) in BF or HAADF to image details at point resolution < 2 Å (200 kV uncorrected TEM), meaning atomically resolved lattice imaging. Higher resolution is possible when corrected for spherical aberrations of the objective lens as is possible on the JEOL ARM200F. The phase contrast is not straight forward to interpret due to contrast reversal from defocus or thickness variations, so e.g. for graphene, the holes in the benzene rings may look like atoms. Therefore, for analysis of HRTEM images below point resolution, a simulation of a TEM image of the atomic structure is often used to predict how
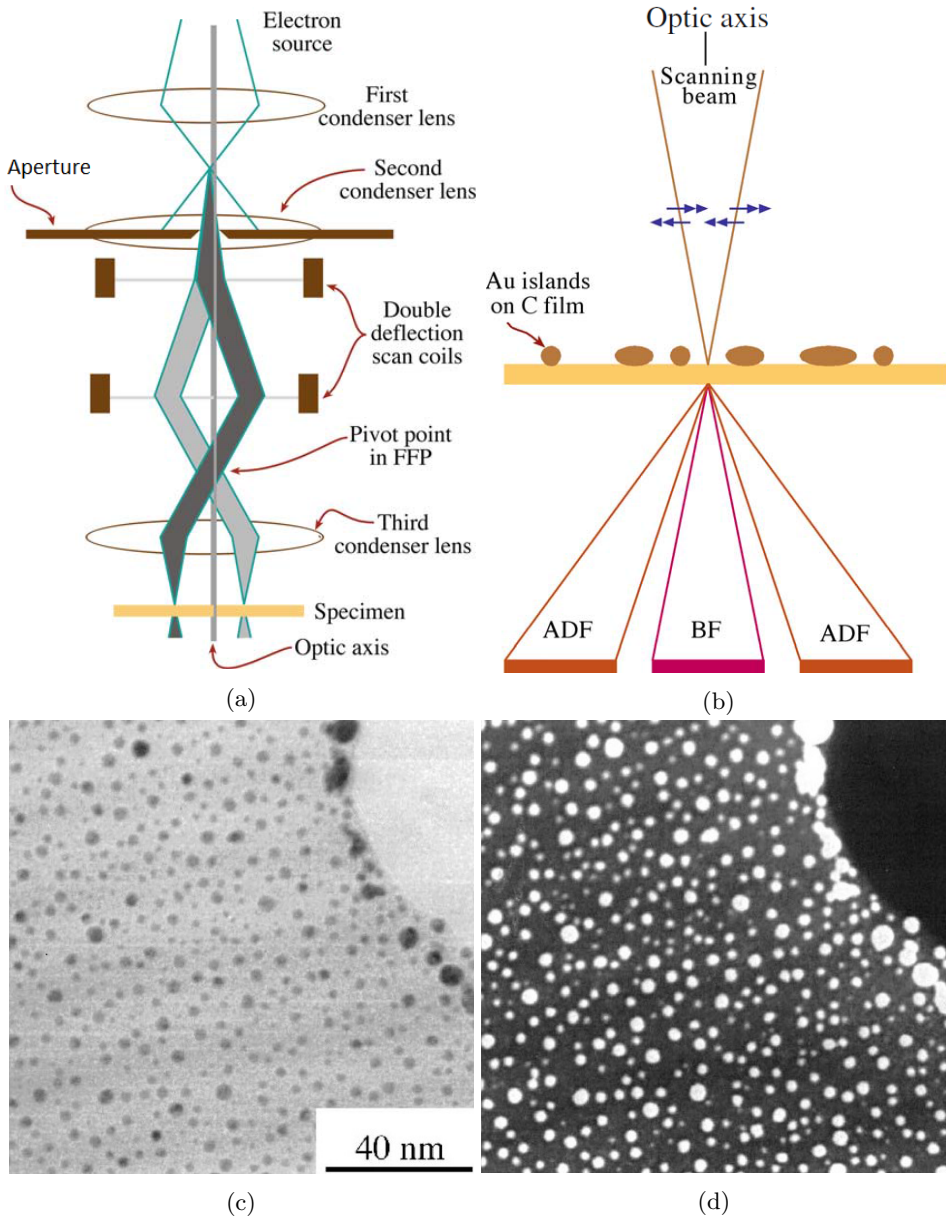
Figure 2.15: **(a)** Ray diagram of probe focusing by the condenser lenses. Scanning parallel to the optical axis is done by the two condenser scan coils. **(b)** Ray diagram for the signals transmitted during STEM. A diverging cone is detected as BF and a hollow cone is detected as rings in the DP for ADF. **(c)** STEM-BF image of Au island on a C film. **(d)** Corresponding ADF image of the same sample. All figures are from Williams and Carter.[88]

the HRTEM image will look. Here only the lattice spacing (with some error) and angles between planes are interpreted, which can be done without simulations.[88] For HRTEM imaging in modern TEMs, the microscope is equipped with a FEG (due to highest coherency) and aberration correctors to correct for the imperfections in the lenses. Both for the probe-forming condenser lenses and the image-forming objective lenses, corrector systems are added for spherical and chromatic aberrations. This increases the resolution with about one order of magnitude, down to below 0.5 Å.

Electron Energy Loss Spectroscopy

An electron energy loss spectroscope (EELS) is often placed at the bottom of the TEM column, and can give further information about the material in the specimen. Similar to EDX, EELS can identify the chemical composition of the material by identifying the elements. While EDX works best with heavier elements, EELS works best at low atomic number elements, due to the distinct difference in energy levels. It can measure detailed information about the crystal, like valence and coordination number, and identify ligands. Using EELS, it is also possible to measure local thickness of the sample.

The instrument works by dispersing the energy distribution of the electrons after inelastic scattering within the sample. The inelastic scattering between electrons in the sample and electrons in the beam cause energy from the beam to be transferred, exciting electrons in the sample, transferring the electrons to an available state above the Fermi level. This is element specific and fine variations in the energy hold information about the bonding of that element within the specimen. The amount of energy transferred by the collision is uniquely characteristic to different materials. Following the beam passing through the sample, the electrons pass through a magnetic prism, spreading out over a distance ordered by kinetic energy. This enables measuring of a spectrum of high energy resolution, from which analysis can reveal the highly detailed information the material structure. In newer STEM systems, this technique can also be scanned with sub-nanometer resolution to create a highly detailed line scan or mapping of the material.

2.4.5 Contrast

In TEM and STEM images there are various types of contrast that require some knowledge for interpretation.[88] The contrast in the amplitude of the BF image is due to two types of contrast, mass-thickness contrast and diffraction contrast, where mass-thickness contrast usually dominates in non-crystalline specimen. Diffraction contrast dominates when the specimen is crystalline. Interference between differently scattered electrons waves (i.e. more than one beam passes the objective aperture), give rise to phase contrast. HRTEM is one example of this. The phase variations are due to the recording principles transformed into amplitude contrast. Beside phase contrast giving lattice fringes, it can also give coarser Moiré fringes which holds crystallographic information, but can easily be interpreted incorrectly.

Mass and Thickness

Mass-thickness contrast is due to incoherent elastic Rutherford scattering. The amount of scattering is strongly dependent on the atomic number of the elements in the specimen (Z) and the thickness. The scattering spreads the electrons out from the optical axis, making areas of the sample that scatter, darker in BF images. This is detected as brighter areas in DF and ADF images. Using larger aperture increase the amount of scattered electrons contributing to the BF image, hence reducing the contrast. Using lower kV increase the scattering angle and cross section, increasing the contrast.

Z-contrast (STEM)

At higher angles (>50 mrad at 200 kV) out from the axis, mass contrast start dominating over thickness contrast. Therefore in HAADF-STEM, the contrast is almost completely mass contrast, also called Z-contrast. By changing the angle of the HAADF detector, the contrast changes for different elements, so qualitative detection is to a certain degree possible. The Z-contrast is largely unaffected by objective lens defocus and specimen thickness, which makes HAADF images directly interpretable at atomic resolution.

Diffraction Contrast

Diffraction contrast is due to elastic Bragg scattering, as previously explained in section 2.4.4. The diffracted electrons form beams that is seen as spots along a circles around the direct beam in the DP. These can be detected as mass-thickness contrast in ADF, or single spots can be used to form DF images. The contrast gives dark areas in BF and bright areas in (A)DF. Diffraction contrast is controlled by crystal structure and orientation. If tilted to two-beam condition, where only one diffraction beam is strong, this give a high contrast in both BF and DF modes, so it is possible to see grains of specific orientations. This also gives good contrast showing strain and dislocations.

Thickness fringes and Bend Contours

If a specimen has an uneven thickness, certain thicknesses will fulfil Bragg's condition for diffraction, creating a band of diffraction contrast. With thickness gradients these fringes are often seen as periodically stripes of alternating dark and bright contrast in BF or DF. Similarly looking bend contours also arise from bending on the specimen. This is due to a bend crystal at periodical angles fulfils Bragg's condition, causing dark and bright lines in the image. Both of these effects changes with tilting of the specimen, which looks like the fringes and contours move as the specimen is tilted.

Phase Contrast

Electron scattering cause difference in the phase of the electron waves, but this is difficult to interpret as the phase of the wave can not be measured directly. The phase contrast is dependent on thickness, orientation, scattering factor, defocus and astigmatism, and these have to be tweaked to illustrate the phase contrast as amplitude contrast in the image. More than one diffracted beam is selected to give the image, and more beams gives a higher resolution, up to the highest resolutions today for BF images, around 0.5 Å.

The phase contrast transfer function gives how the phase contrast results in an amplitude contrast image. The function is often optimised for the smallest point that can be interpreted without simulations, i.e. all distance larger than this point have the same contrast. This is done by defocusing according to Scherzer as given in equation 2.9:

$$\Delta f_{Sch} = 1.2(C_s \lambda)^{1/2} \tag{2.9}$$

Lattice Fringes

The interference of the different beams cause lattice fringes (as in HRTEM), that if analysed correctly, give information about the lattice structure of the sample. These fringes look like crystal planes, but are not a direct image of the structure and analysis might lead to incorrect information about the structure. The fringes are seen as parallel periodic lines with both lattice spacing and crystal direction matching the crystal plane, but contrast can be bright or dark. These sets of visible fringes also corresponds to a spots in the DP, but can be from a smaller area than can be isolated by the selected area aperture. These fringes are particularly visible at edge of the crystal. For 2D layered crystals like graphene, these fringes at the edge are important for crystallographic analysis, as it has got a spacing matching the interlayer distance, and it is possible to count the number of stacked layers.

Moiré Fringes

Moiré patterns are also often visible in TEM images, caused by interfering sets of mismatched lattice fringes with similar periodicity. These patterns are illustrated in figure 2.16, where the patterns are seen to arise from translational mismatch, rotational mismatch or both. The periodicity of the pattern is inverse of the mismatch, meaning a small mismatch gives a large periodicity. These can be analysed to find defects and interfaces. If the interfering lattices are of the same crystal, e.g. two layers of graphene but with slightly different orientation, the patterns can be seen as a magnification of the crystal structure. This means the Ångström-structured lattice becomes visible at nanometer scale, even if the TEM does not have a high enough resolution for lattice imaging.
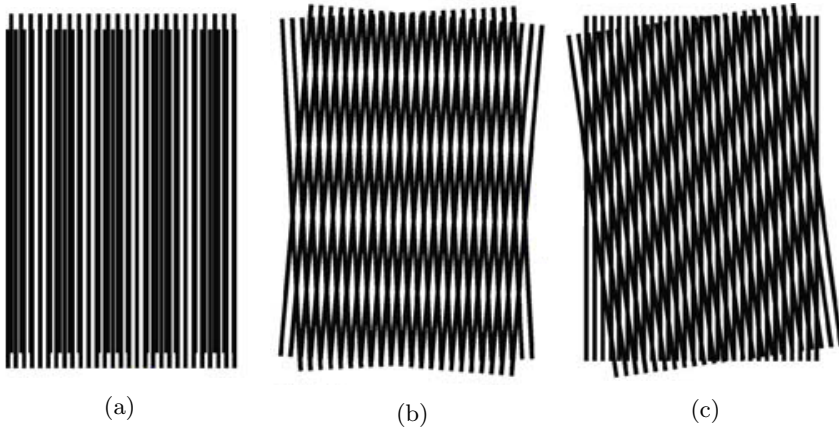

(a) (b) (c)

Figure 2.16: Periodic Moiré fringes: **(a)** Due to translation of the lattice. **(b)** Due to rotation of the lattice. **(c)** Due to both translation and rotation.[88]

Chapter 3

Methods

In this chapter, the experimental methods for synthesis, transfer and characterization of graphene is described. Graphene was grown by chemical vapour deposition (CVD) on two different substrates: copper foil and copper thin film (Cu-TF) on silicon. The TF were deposited by electron beam deposition (EBD). A profilometer was used to measure the thickness and surface roughness of the Cu-TFs after CVD. The as-grown samples were studied by scanning electron microscopy (SEM) and, after transfer to TEM grids, further studied by transmission electron microscopy (TEM) and scanning transmission electron microscopy (STEM), to determine the grain structure, crystallinity and contaminants of the produced graphene. Energy-dispersive X-ray spectroscopy in the SEM and TEM was used for elemental analysis.

3.1   Synthesis

3.1.1   Graphene on Copper Foil

To synthesize graphene, a newly installed TA100 quartz tube thermal CVD system from Graphene Square was used. The CVD chamber consisted of 6" diameter outer quartz tube with 1.5" inner tubes for holding samples, and was operated at a chamber pressure down to 0.5 mtorr. CH_4 was used as precursor gas for the CVD reaction, along with H_2. 4-8 pieces of approximately 3x3 mm Cu foil from GrapheneSquare, were used as a catalyst substrate for the growth. First, the CVD was run with the default parameters, as provided by GrapheneSquare: 5 torr pressure, 1000°C temperature, 5 sccm H_2 gas flow, 45 sccm CH_4 gas flow, giving a CH_4:H_2-ratio of 9:1.

The procedure for the process is illustrated in figure 3.1, and is as follows:

1. Ventilate and load samples into chamber.

2. Pump down chamber to pressure < 1 mtorr (0-20 min).

3. Start H_2 gas flow of 5 sccm.

4. Heat from room temperature to $1000°C$ with heating rate of $25°C/min$ (20-60 min).

5. Stabilize temperature (60-80 min).

6. Start CVD-reaction by starting CH_4 gas flow og 45 sccm and increasing the champer pressure to 5 torr (80-110 min).

7. Stop CH_4 gas flow and turn off heating.

8. When the temperature cools to around $500°C$, open the latches on the furnace to increase the cooling rate, and stop the H_2 gas flow to pump down to pressure $< 1·10^{-3}$ torr (110-160 min).

9. When the temperature cools to around $400°C$, open the lid of the furnace completely, further increasing the cooling rate (160-170 min).

10. When the temperature cools to around $200°C$, ventilate and remove the sample(190 min).
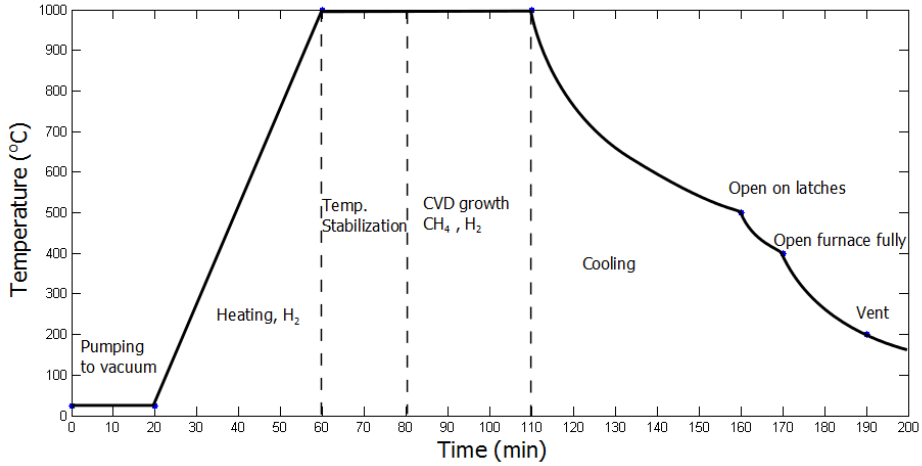

Figure 3.1: Schematic of the CVD growth procedure.

To further improve the graphene growth, a total of 5 batch with varied parameters were attempted, as seen in table 3.1. In all these, the temperature was at 1000°C, and H_2 gas flow was 5 sccm, as the CH_4 gas flow was varied to change the ratio.

Table 3.1: Parameters used for CVD growth of graphene on Cu foil.

Batch [#]	Pressure [torr]	CH_4:H_2-ratio	Growth time [min]
1	5	9:1	30
2	5	9:1	25
3	10	9:1	10
4	1	1:5	10
5	5	4:1	10

3.1.2 Graphene on Copper Thin Film

Similar to what has previously been demonstrated,[24] it was also attempted to grow graphene on an arbitrary substrate material. Using e-beam deposition (EBD) of a thin film of Cu on a (111) Si wafer, followed by CVD growth of graphene and evaporation of the Cu-TF, which leaves the graphene on the Si.

Electron Beam Deposition of Copper Thin Film

For the EBD of Cu a Pfeiffer Vacuum Classic 500 e-beam deposition system was used. It operates at a chamber pressure of $5 \cdot 10^{-11}$ bar and uses a 8 kV acceleration voltage to evaporate various materials, which deposit as an amorphous TF on the substrate. As substrates for deposition, pieces of (111) Si wafer sized a few mm^2 were used without any treatment or cleaning beforehand. A Cu-TF with 100 nm thickness was deposited by the following procedure:

1. Ventilate and load samples into load lock.

2. Pump down load lock to a pressure $< 10^{-7}$ bar and transfer the samples into the chamber.

3. Start rotation of the sample holder, to ensure even deposition.

4. Start the e-beam, and adjust beam current for a stable deposition rate of 1 Å/s.

5. Open the shutter covering the sample.

6. Deposition for 1000 s, giving a TF of approximately 100 nm.

7. Turn off the e-beam and sample rotation, and cool down for 15 min.

8. Transfer the samples to the load lock.

9. Ventilate and unload the samples.

Chemical Vapour Deposition and Evaporation of Copper

For CVD growth of graphene on the Cu-TF, modified parameters from growth batch 3 in table 3.1, were used. For evaporating the Cu, after step 7 in the CVD process in 3.1.1, H_2 gas flow was stopped, chamber pumped down to pressure < 1 mtorr, temperature increased to $1030°C$, and held for 10 minutes before cooling. For comparison, 4 pieces of Cu foil was also in the chamber during this experiment.

3.2 Specimen Preparation

Without further preaparation, the as-grown samples were studied in SEM, but for further in-depth analysis by SEM and TEM, the graphene on Cu foil was transferred onto other substrates. For higher contrast SEM imaging, the graphene were transferred onto pieces of (111) Si wafer, and for STEM and TEM imaging, onto Cu TEM grids.

3.2.1 Transfer of Graphene From Copper Foil

Transfer from the Cu foil was done by etching the Cu in a bath of 50 g/L $Fe(NO_3)_3$, as shown in figure 3.2. Before etching, samples from batches 3 and 5 were put in a Diener Femto plasma cleaner for 60 seconds in O_2 plasma, with the bottom side of the Cu foil up. This was to remove any graphene or particle contaminants after the CVD growth on underside on the foil, as otherwise this ended up at the graphene from the upper side of the foil after the etch.

One piece of cleaned Cu foil was put in a bath of $Fe(NO_3)_3$, floating on the surface with the graphene side up, as shown in figure 3.2a. After 12 hours, the Cu foil had been etched away, leaving the graphene floating on the surface, as shown in figure 3.2b, due to it being hydrophobic. The etching reaction is:

$$Cu(s) + Fe^{3+}(aq) \rightarrow Fe(s) + Cu^{2+}(aq) \tag{3.1}$$
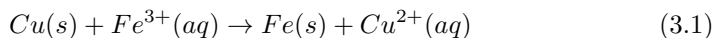
This reaction also leaves some Fe contamination on the floating graphene. To clean away these contaminants, the graphene was transferred to a DI water bath. As seen in figure 3.2b, the fairly clean monolayer of graphene was almost invisible, which made this transfer difficult. Using a tweezer, the graphene was scooped onto a quartz glass slide, as shown in figure 3.2c. In this transfer of the free-floating graphene, it was essential with extremely careful handling of the tweezer, to avoid tearing up the graphene. The graphene was then put into the DI water, separating from the quartz glass and floating on the surface. Then, the cleaned graphene was scooped up with a 2000 mesh Cu TEM grid, as shown in figure 3.2d. This step is very difficult, as the graphene is repelled from the TEM grid, having to be pushed towards the edge of the glass to get it onto the TEM grid,

and additionally, the graphene is now even more difficult to see, being cleaner the previously. Finally, the TEM grid is dried slowly in ambient atmosphere, to reduce capillary forces creating cracks in the graphene. Immidiately before insertion into the TEM column, samples in batches 3 and 5 were also O_2 plasma cleaned twice for 10 s in a Fischione 2010 plasma cleaner with a shielding holder, to remove hydrocarbon contamination.[92]
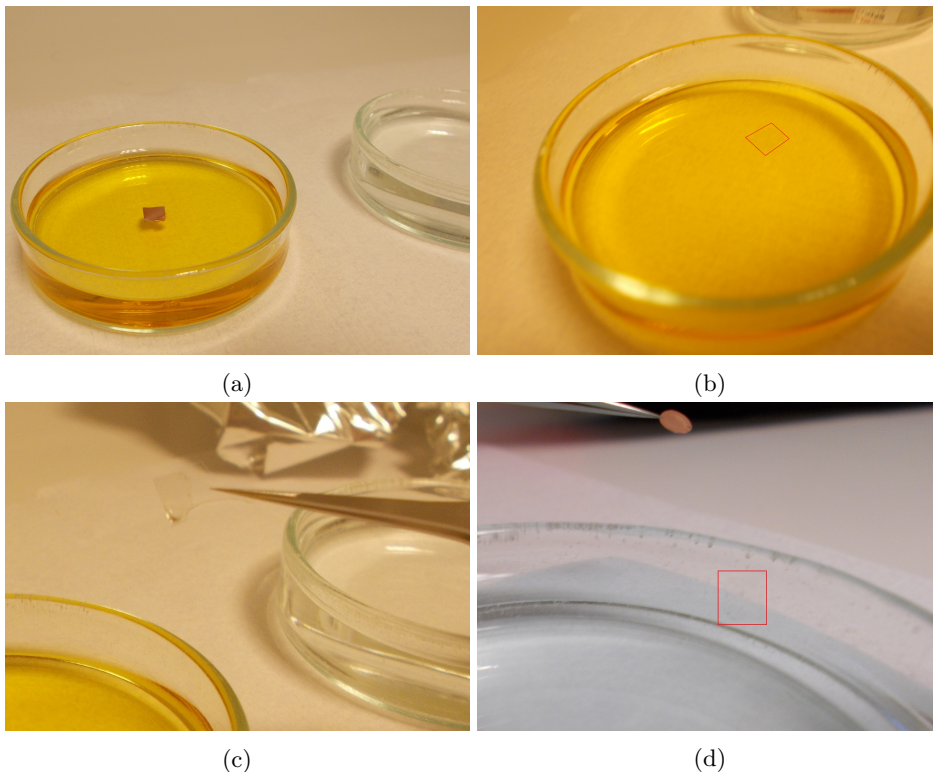

Figure 3.2: Photographs of graphene transfer: **(a)** A piece of Cu foil floating in $Fe(NO_3)_3$ etchant bath. **(b)** A nearly invisible flake of graphene, marked in red, free-floating on the surface of the bath after the Cu foil has been etched. **(c)** Graphene flake on a quartz glass slide, held by a tweezer, after having been scooped out of the $Fe(NO_3)_3$ solution. **(d)** A nearly invisible flake of graphene, marked in red, free-floating on the surface of a DI water bath, after having been dipped into the water. To be scooped onto a Cu TEM grid, held by a tweezer.

A sample from the batch 3 in table 3.1 was also scoped onto pieces of (111) Si wafer instead of TEM grids, as it is a very good substrates for SEM imaging. This is due to the flatness of the Si surface making it easy to differentiate the topography of Si and graphene, as compared to graphene on Cu foil. A sample from batch 2 was transferred to a quartz glass substrate for SEM imaging, but this sample was difficult to image due to charge up, even after it was sputtered with 10 nm gold (Cressington 208 HR B Sputter Coater), to increase the surface conductivity.

3.3   Material Characterization

To determine the thickness and surface roughness of the deposited TFs, a profilometer was used. For studying the as-grown graphene, to determine crystallinity, number of layers, and contaminants after CVD growth, a scanning electron microscopy (SEM) was used. To study the graphene and contaminants at a high resolution, and to determine the crystal structure of the graphene, transmission electron microscopy (TEM) was used.

3.3.1   Profilometry

A Veeco Dektak 150 profilometer with 12.5 µm diamond tip stylus, 1 Å maximum vertical resolution (at 6.55 µm range), was used. The surface roughness for the Cu-TF was measured after EBD. For one specimen, an area of the wafers had been covered with permanent marker before EBD, followed by lift-off using acetone and ultrasonication. This removed the TF from an area of the specimen, giving a sharp edge for an exact measurement of the thickness of the TFs with the profilometer.

3.3.2   Scanning Electron Microscopy

A Hitachi S-5500 cold field-[91]emission SEM, was used. This SEM has an in-lens detector for secondary electrons (SE) and low angle back-scattered electrons (LA-BSE), and it also has a YAG-BSE detector. If using a STEM sample holder with a TEM grid sample, is can also be operated in bright-field (BF) and dark-field (DF) STEM mode. It can use an acceleration voltage of 0.5 - 30 kV, max current of 20 µA, where 30 kV can give a resolution up to 0.4 nm. It also has an insertable Bruker XFlash SSD EDX detector, operated with Esprit software.

The as-grown graphene from the CVD was studied directly on the Cu foil. A sample from the batch 3 in table 3.1, was also studied on a (111)Si wafer substrate. A sample from batch 2 transferred to a quartz glass substrate was also studied, but charge-up made imaging difficult. After transfer to TEM grids, samples from batches 3 and 5 in table 3.1, were also studied using simultaneous SE and BF-STEM at 30 kV. The samples of graphene on Cu-TFs were also studied by SEM.

It is noteworthy that imaging at low voltage, in this case 0.6 kV (0.5 kV proved suboptimal), was especially useful, as this gave very high topological contrast for the graphene. It was also operated at voltages 1, 2, 5, 15 and 30 kV to compare the effect of the voltage. LA-BSE with 10-15% beam mixing was also used, while 30 kV was used for EDX measurements.

3.3.3 Transmission Electron Microscopy

For studying the structure of the graphene and contaminant particles from the CVD growth, a JEOL 2100 JEM was used. This TEM has a LaB_6 filament, HR pole piece, and was operated at 80, 120 and 200 kV. BF and DF imaging and DPs were captured by a Gatan 2k Orius CCD (side mounted, large view). It has an insertable Oxford X-Max 80 SDD EDX (solid angle 0.23 sr), operated by Aztek software. Image acquisition was done by Gatan GMS 1.8, 32 bit software, which was also used for image processing and analysis.

Spherical aberration corrected TEM was done to study one of the samples from batch 5 in table 3.1, to image the monolayer graphene at a higher magnification with better image quality, and to identify the contaminating nanoparticles in more detail. For this, A double corrected JEOL JEM-ARM200F was used, operated by co-advicer Vidar Fauske. This TEM has a cold-FEG with energy spread of < 0.3 eV, a HR pole piece, and Cs-probe and -image correctors. It has an insertable Centurio SDD EDX (solid angle 0.98 sr), and a 2k Orius CCD (side mounted) for recording DPs and a 2k UltraScan XP CCD (bottom mounted) for HRTEM imaging. It has detectors for BF(2x), ABF, ADF, and HAADF(2x) STEM, and a Quantum RS image filter for EELS/EFTEM. In this study only DP, HRTEM, and limited HAADF-STEM, EDX and EELS could be used due to the available time on the machine. Image recording was done using Gatan GMS 2.3, 64 bit, software.

It was operated at 80 kV to reduce knock-on beam damage, and the monolayer graphene was studied by BF and DPs, while HAADF-STEM and EDX were used to identify the composition of contaminating nanoparticles.

Chapter 4

Results

The experiments were done in two parts: first, CVD growth on Cu foil; second, CVD on an e-beam deposited Cu-TF. The growth on Cu foil was done in 5 batches of 4-8 samples. After CVD, these were studied using SEM, then transferred onto Si wafer or TEM grids for further study with STEM, TEM, HRTEM. Four samples were grown at a higher temperature of $1030°$C along with Cu-TF samples. No results from growth batch 4 is included, as the parameters resulted in the sample being completely covered with particles, and there was no graphene visible. CVD of Cu-TF was done in one batch of two samples. One sample was studied by profilometer to measure thickness and roughness of the surface. This sample was further studied by SEM.

4.1 Graphene on Copper Foil

After CVD, samples from the batches were first studied by SEM, and are shown in images in section 4.1.1. These samples were further studied by TEM with results shown in section 4.1.2, and with HRTEM in section 4.1.3. Some samples from batch 2 were also transferred onto pieces of quartz glass, but this substrate had too much problems with charge-up to give any useful SEM images. There are also no SEM images from batch 4 included, as this surface was covered with small nanoparticles similar to what is seen in figure 4.1a, but with no signs of graphene present. Because of this, no samples from batch 4 were studied further.

4.1.1 Scanning Electron Microscopy

Batch 1

Images of a samples from batch 1 in table 3.1 are given in figure 4.1. These surfaces were largely contaminated due to the stainless steel stage holding the samples. The remaining batches were grown without this steel stage. In figures 4.1a and 4.1b, hexagonally faceted rods are seen, typically sized a few hundred nanometers long. A higher magnification of the base of one such rod is also seen in the upper right corner of 4.1c. These were identified by EDX to be of Cr, originating from the stainless steel.
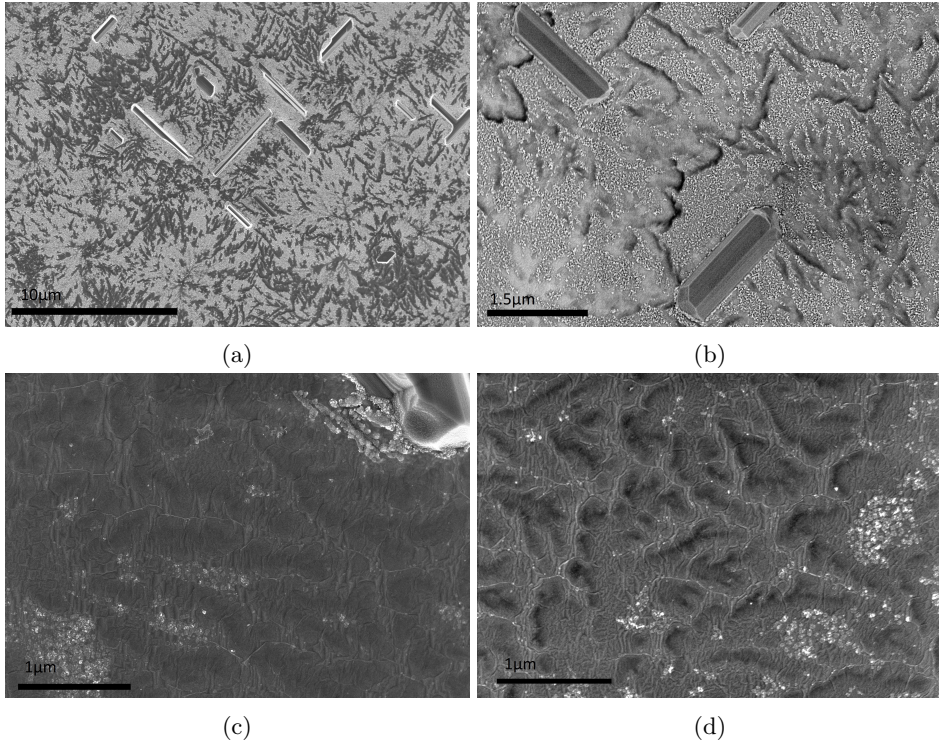

(a)

(b)

(c)

(d)

Figure 4.1: SEM images from the first CVD batch. **(a)** Overview showing the Cu surface covered by nanoparticles and hexagonal Cr nanorods. Note the Cr rods' 90° orientation relative to each other. **(b)** A higher magnification LA-BSE image of an area with three Cr rods. Note the hexagonal facets of the rods. **(c)** An area with less nanoparticles beside a Cr rod, showing graphene wrinkles as thin bright lines. Two such are marked. Image taken at 5 kV. **(d)** Image taken at 1.5 kV of an area nearby (c).

Batches 2, 3 and 5

A SEM image from batch 2 is seen in figure 4.2. This figure is an overview representative of how the surface of batches 2, 3 and 5 looked. These are shown more in detail in figure 4.3. In figure 4.3, details are shown about how graphene was typically identified on the Cu surface. In figures 4.3a and 4.3d, graphene is seen as present due to its wrinkles. In figure 4.3d the wrinkles are seen to have aligned relative to the stepped structure of the Cu surface. In figure 4.3b, domains of a secondary graphene layer are seen to have a round or hexagonally angled shape.
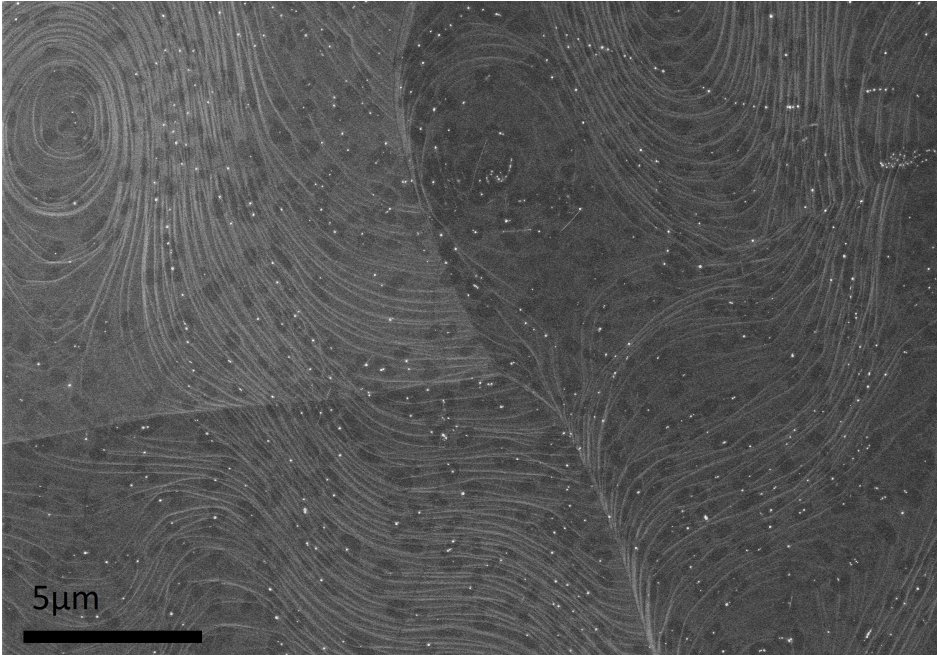

Figure 4.2: A SEM image representative of how the Cu surfaces of samples 2, 3 and 5 looked after CVD. In the centre is a grain boundary between three Cu grains in the right half, upper left (brighter area) and lower left of the image. The bright flowing lines, forming patterns similar to contour lines, are due to the Cu surface forming steps upon cooldown because of thermal shrinkage. Amongst these lines are SiO_2 nanoparticles. Underneath the particles is a monolayer of graphene, covering the entire surface, which can be found due to the presence of a few thin bright lines of wrinkles (two such are marked), that can vaguely be distinguished from the Cu step lines. Around the nanoparticles are dark domains of a second graphene layer, sized a few 100s of nanometers to 1 µm in diameter.

In these images, the effect of HT for studying graphene can be compared. In the 30 kV figure 4.3a, the 5 kV 4.2 and the 2 kV 4.3b, the Cu surface is clear. However, in the 1 kV figures 4.3c and 4.3d, the Cu surface is almost invisible, making the graphene visible.
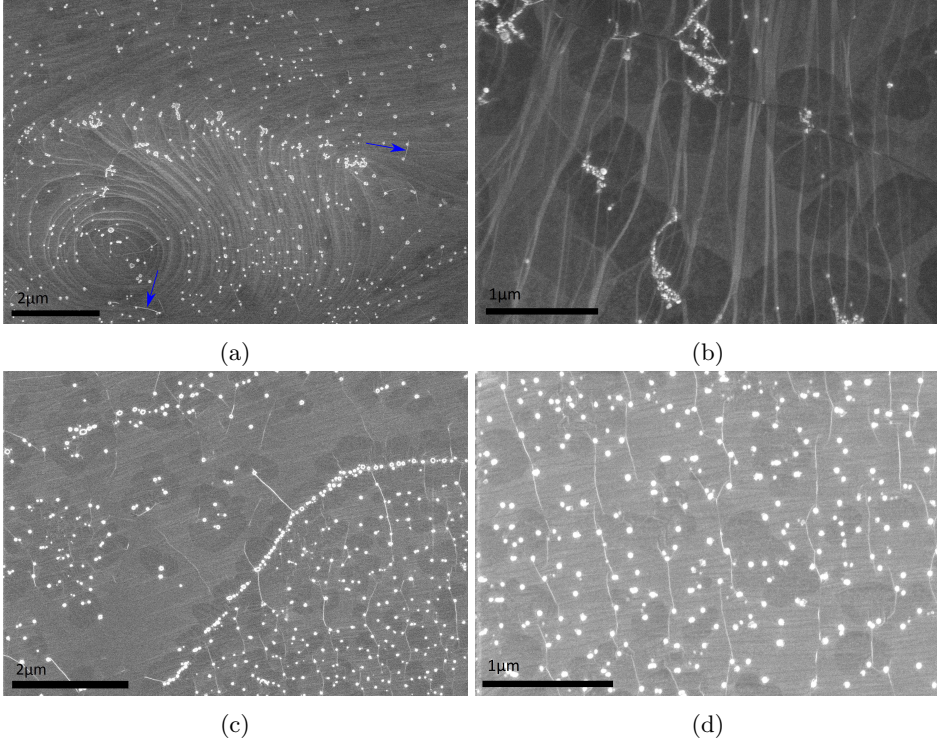

(a)

(b)

(c)

(d)

Figure 4.3: Features of graphene typically seen on the Cu surface of batches 2, 3 and 5. **(a)** An area imaged at 30 kV. Graphene wrinkles could be seen at all HT. Two such are marked. **(b)** A high magnification image of a few domains of the second graphene layer, taken at 2 kV. These domains were typically observed to have a roughly round shape, but some domains were seen to have 120° corners, as can be expected of a hexagonal lattice. **(c)** A boundary between two regions: In the upper left, some wrinkles are seen, while in the lower right region much more wrinkles can be seen. Image taken at 1 kV. **(d)** Another area similar to the lower right in (c). The wrinkles are ordered vertically, perpendicular to the step edges of the Cu surface, that are laterally oriented. The Cu step edges are difficult to see because of the low 1 kV HT.

Comparing SE and LA-BSE imaging

As explained in Theory section 2.3.4, the Hitachi S-5500 has a technique, LA-BSE, to mix SE and low energy BSE electrons, giving different contrast. The use of LA-BSE is discussed in section 5.1.4. The microscope also has a YAG-BSE ring detector, but for these samples it gave poor results compared to LA-BSE. In figure 4.4, an area has been imaged by SE (figure 4.4a) and LA-BSE (figure 4.4b). In these images, graphene wrinkles that are hardly visible in SE are clearly visible in LA-BSE. An area of graphene transferred onto a Si wafer surface was images by SE in figure 4.7c, and LA-BSE in figure 4.7d. Here we see LA-BSE emphasizes thickness and tent contrast of graphene.
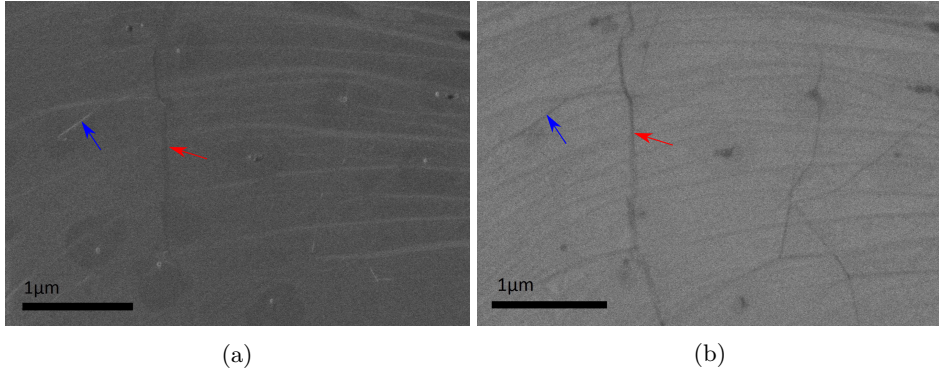

(a) (b)

Figure 4.4: SEM images comparing SE and LA-BSE imaging, both taken at 0.6 kV **(a)** SE image of a Cu surface after CVD. Two graphene wrinkles are marked, a thin in blue and a wide in red. **(b)** LA-BSE image of the same area. Where only a few wrinkles are in seen in (a), in LA-BSE many become clearly visible dark lines, as the graphene has folded double onto itself, becoming three layers thick instead on one.

Growth on the underside of the Cu foil

Due to the observation of crumpled graphene in TEM images from batch 2 (see figure 4.10), a SEM study was done on the underside of a sample from batch 3. Images from this is seen in figure 4.5. An overview is seen in figure 4.5a, showing that the concentration of secondary graphene varies significantly. A closer look in figure 4.5b, shows the local areas look similar to what has previously been seen of the upper side of the foil.

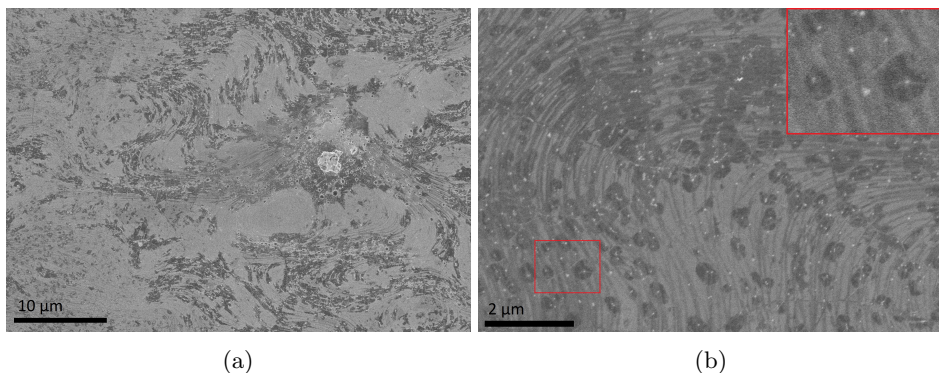|	
(a)	(b)

Figure 4.5: SEM images of the underside of a Cu substrate from batch 3. **(a)** An overview. Note the unevenness of darker areas where more secondary graphene had grown. **(b)** A higher magnification image of an area similar to the darker areas in (a). The marked area is magnified in the inset, showing a wrinkle.

Growth at 1030°C

As a control to the Cu-TF process (explained in methods section 3.1.2, results in section 4.2), pieces of Cu foil were also placed in the chamber while the CVD process ran at same parameters as batch 3 in table 3.1, but at 1030°C, with a following low pressure evaporation phase. The Cu surface resulting from this is seen in figure 4.6.

Graphene on Si wafer

In figure 4.7, the SEM images show graphene from batch 3 transferred onto a smooth Si wafer surface. From the overview in figure 4.7a, we see the transfer had caused some cracks to form, but the monolayer was largely intact. The transfer had caused graphene from the underside of the Cu foil to crumple, covering the monolayer, but also forming some larger cluster, such as the one in the crack central in the image. Imaging at 0.6 kV was important when studying graphene on a Si surface, as imaging at higher HT such as 5 kV, seen in figure 4.7b, gave significantly less contrast and detail about the graphene, compared to figure 4.7c. In figure 4.7c, we see the SiO_2 particles from the underside of the foil lies under the graphene, as indicated by the tent contrast. Comparing the SE image in 4.7c with the LA-BSE image in 4.7d, there is a clear contrast between the monolayered area and the multilayered area with crumpled graphene. LA-BSE also emphasizes the tent contrast SE. As is seen in figure 4.8, on Si surface there is a distinct difference between 1 or 2 or more layers of graphene, enabling distinction of different layered graphene. At high mag, grain boundaries are visible, enabling clear study of graphene grain size. These were observed to be a few 100s to 1 µm in size.
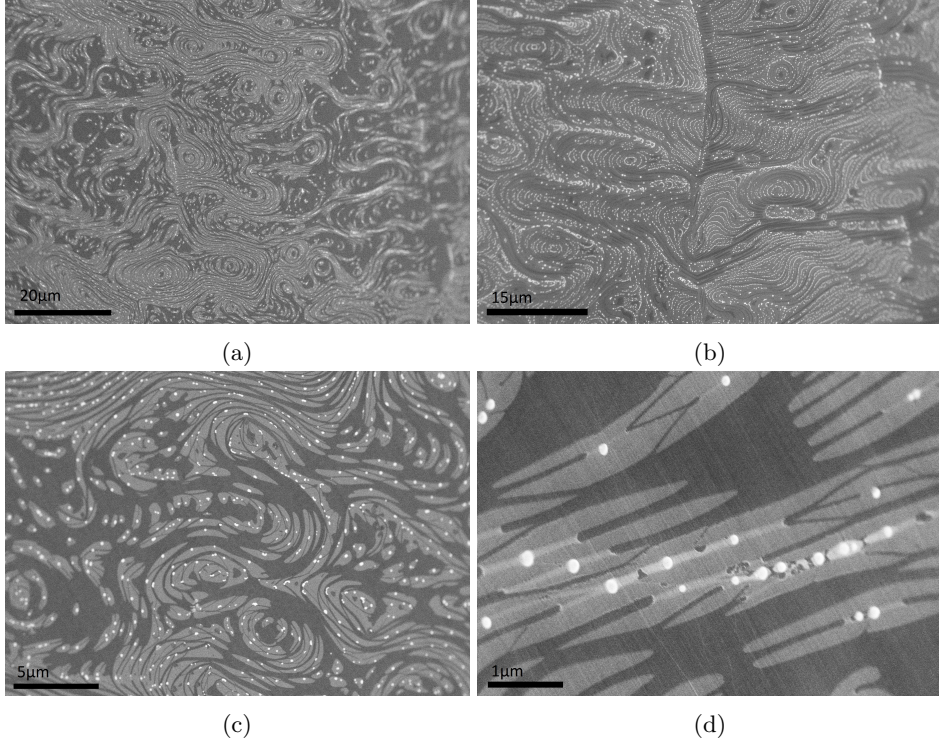
(a)　　　　　　　　　　　　　(b)

(c)　　　　　　　　　　　　　(d)

Figure 4.6: SEM images of the surface of the Cu substrates that were in the Cu-TF process at 1030°C. **(a)** An overview of the surface showing swirling fluid patterns in the Cu surface. There is a significant difference in concentration of particles surrounded by bright domains, as the dark areas hold less than the bright. **(b)** A different area where the particles have organized along the steps in the Cu surface. There are also dark bands distinctly free of particles. **(c)** A closer look at an area similar to (a). The nanoparticles all seem to be placed at either the center or the edge of a domain, and all domains seem to have at least one particle. **(d)** At a higher magnification. two different types of bright domains can be seen. In the gaps between the primary domains, surrounding the particles there seem to be domains of a slightly brighter colour. The contrast is likely due to different thickness of the graphene.
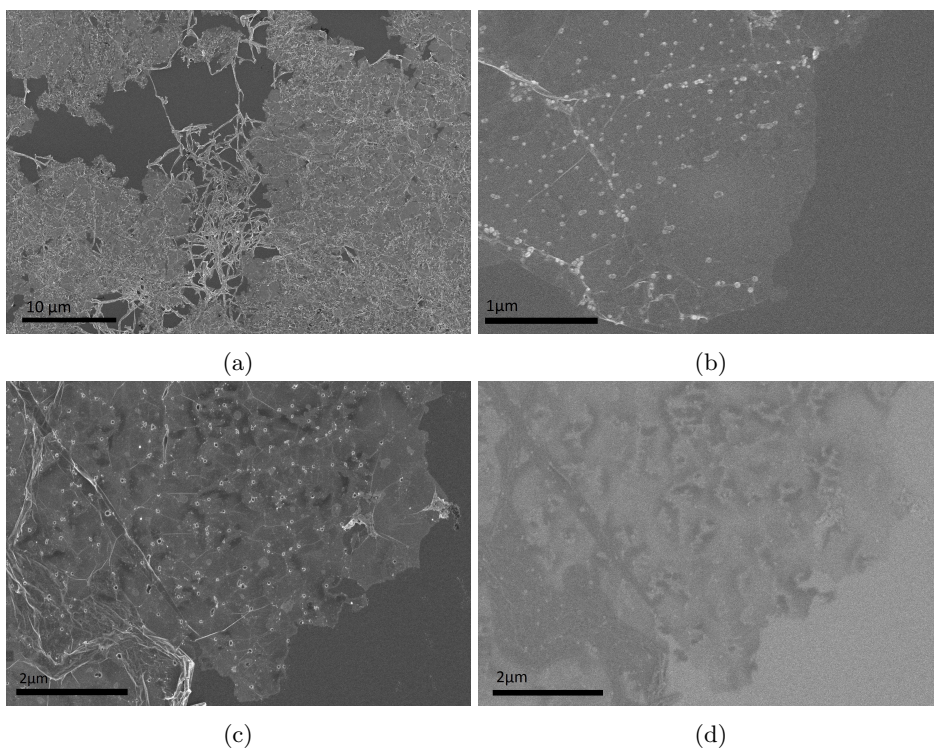
49

(a)

(b)

(c)

(d)

Figure 4.7: SEM images of graphene from batch 3 transferred to Si. All images taken at 0.6 kV except (b). **(a)** Overview, showing monolayered graphene with cracks and crumpled graphene. **(b)** Image of a largely monolayered area taken at 5 kV. **(c)**The edge of a graphene covered area. Most of the area is covered by monolayered graphene. The secondary graphene domains appear bright coloured. Two such domains are marked in blue. The tent contrast, as is seen in the red marked area, indicates many of the particles are underneath the graphene, while the particles not surrounded by tent contrast are on top of the graphene. In the bottom left corner is crumpled graphene from the underside of the Cu foil. **(d)** LA-BSE image of the same area as (c).
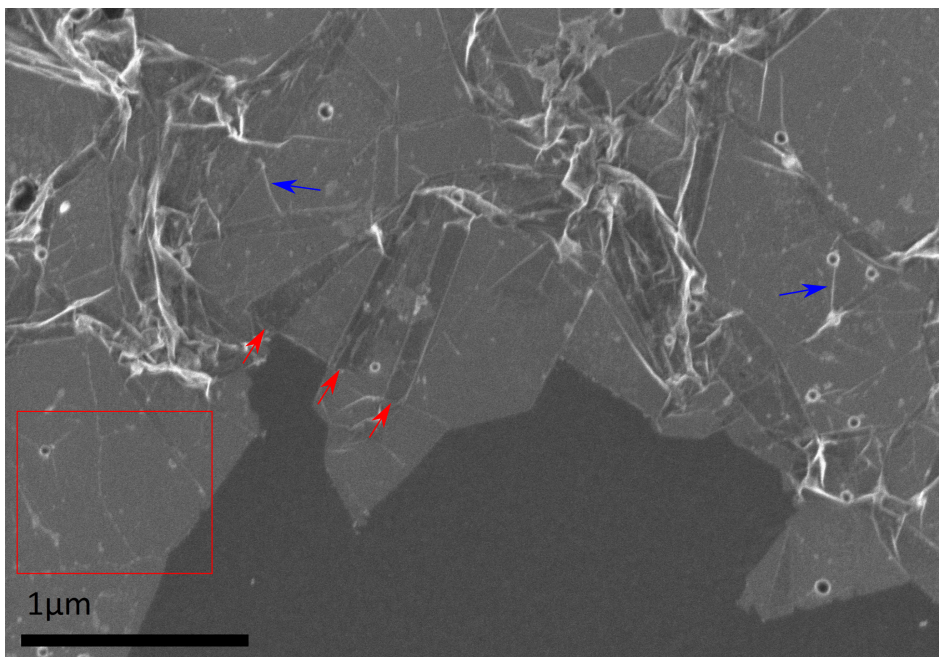
Figure 4.8: An area seen at higher magnification. Note the straight edges and angles at the edge. In the marked area individual graphene grain boundaries are clearly visible. Three wider type of wrinkles are marked where the monolayer graphene has folded triple, showing distinctly different contrast. For comparison, thin wrinkles are also marked in blue.

4.1.2 Transmission Electron Microscopy

BF-STEM

The Hitachi S-5500 was also capable of imaging in BF- and DF-STEM modes. BF images of graphene transferred onto a TEM grid is seen in figure 4.9. In the overview in figure 4.9a, thickness contrast makes it possible to differentiate the monolayered area, the triple layered are of the wide wrinkle, and the crumpled graphene of varying thickness. The high resolution image in figure 4.9b is distorted by carbon contamination, but a grain boundary in the monolayered graphene and iron oxide nanoparticles are seen. DF-STEM was also attempted, but due to low contrast and contamination, it was not possible to get any good images.
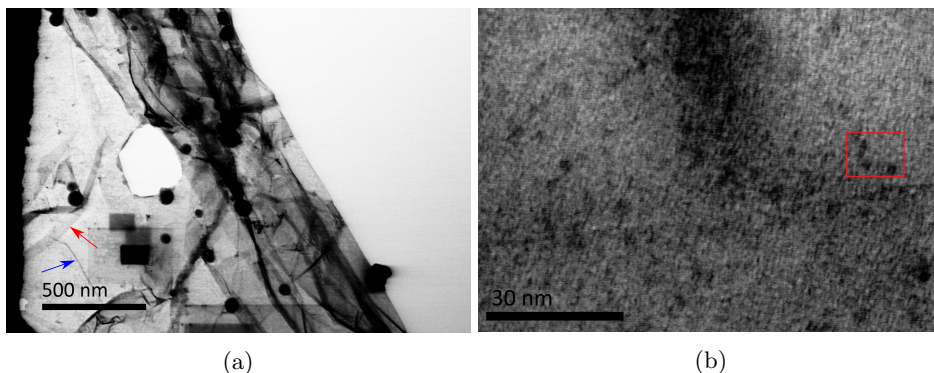
Figure 4.9: BF-STEM images. **(a)** Overview of graphene suspended from the corner of a square of the TEM grid. Much of the graphene has crumpled, but close to the edge of the TEM grid on the left is mostly monolayered graphene. In the monolayered area, a thin and a wide wrinkle are marked. There are areas with dark rectangles of contamination are where imaging has previously been attempted. **(b)** In this high magnification image, little detail is visible due to carbon contamination, but a single grain boundary is seen going horizontally across the image. Three iron oxide nanoparticles are also marked.

Batches 2, 3 and 5

Graphene from batches 2, 3 and 5 were transferred to TEM grids for further study by TEM. In figures 4.10 and 4.11 are typical features that were seen in samples from these batches. Figure 4.10a shows how graphene from batch 2 looked after transfer suspended from a TEM grid.The surface tension of water had torn holes in the graphene. There is also crumpled graphene from the underside, which is seen closer in figure 4.10b and 4.10c. Two SiO_2 particles are seen in figure 4.10d.

Images from batch 5 are seen in figure 4.11, where there were large areas with little crumpled graphene. In these images, some additional details of the graphene could be seen. In figure 4.11a a wide and and thin wrinkle are seen, as well as two pieces of crumpled graphene, one which in one end is a flat sheet and in the other end crumpled. The other piece of is rolled up like a nanoscroll, and is seen at higher magnification in figure 4.11b. The inset SADP shows the double set of six hexagonally aligned spots, characteristic of monolayer graphene. There are also additional weaker patterns from the crumpled graphene. In figure 4.11c, the grain boundary on a monolayer is seen, with a DP for each of the two grains. When the beam was moved to the left of the image, the first pattern weakened, while the second grew stronger.
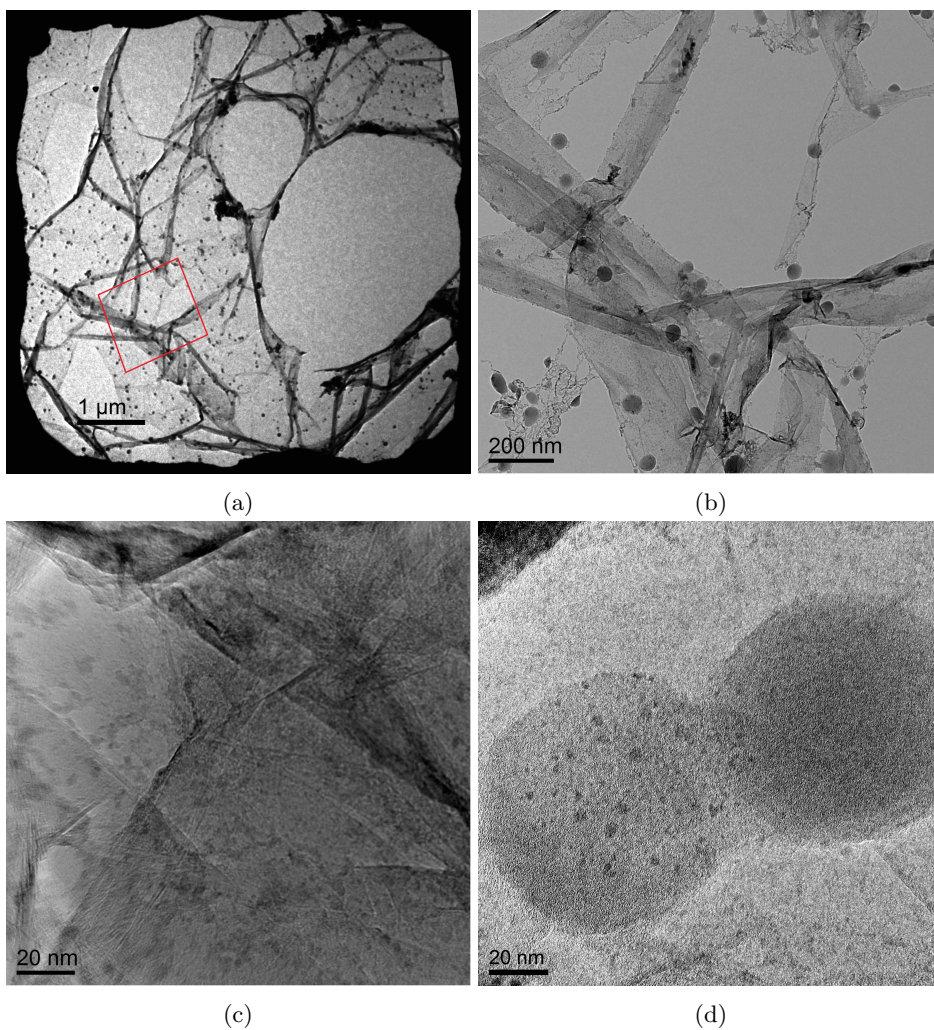
Figure 4.10: TEM images of transferred graphene. **(a)** Overview of graphene from batch 2 covering a square of a TEM grid. Most of the area is covered by a monolayer. Large holes have formed during transfer, with the graphene rolling up to form a thicker ring surrounding the holes. There is also crumpled graphene originating from the underside of the Cu foil. **(b)** Magnified image of area marked in (a) showing crumpled and SiO_2 nanoparticles. **(c)** High resolution image of a cluster of crumpled graphene similar to what is in the center of (b). **(d)** BF image of two amorphous SiO_2 nanoparticles that fused under the irradiation of the e-beam.
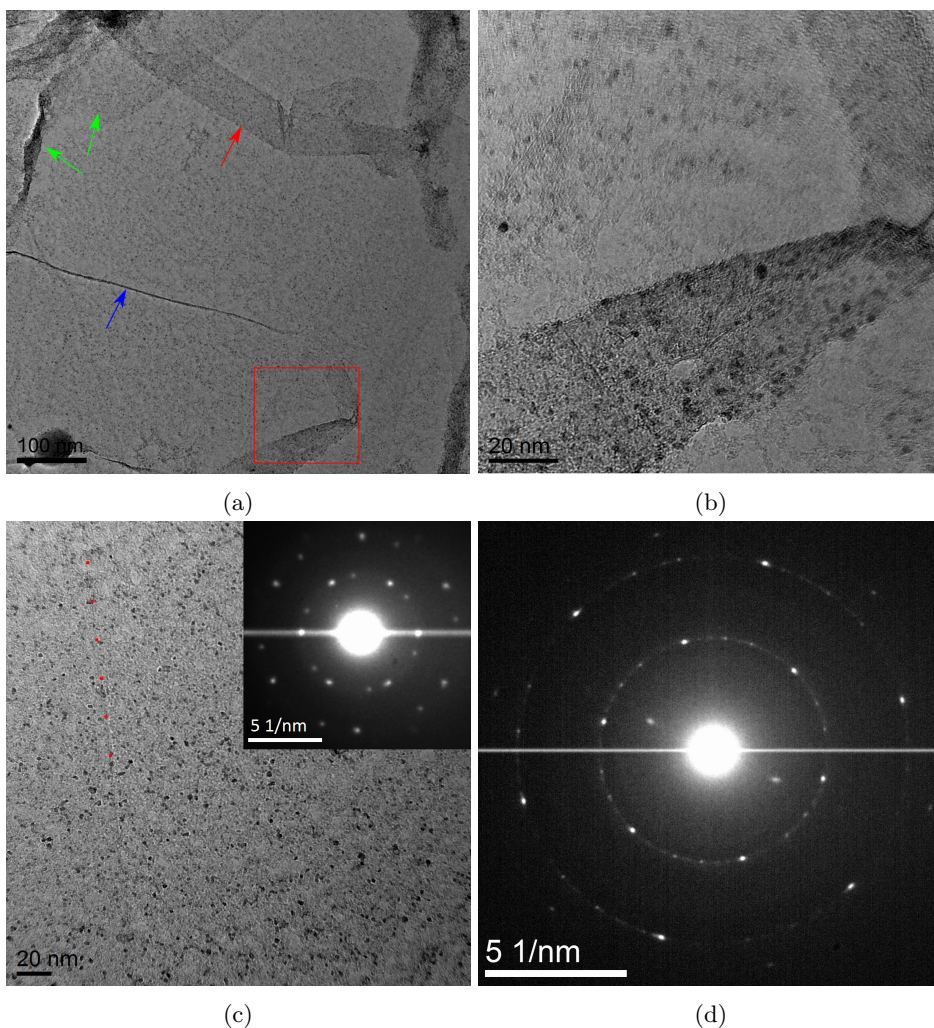
Figure 4.11: **(a)** Overview of an area from batch 5 covered by a monolayer with less crumpled graphene. On the right edge are agglomerations of iron oxide nanoparticles. Two wrinkles are marked blue and red, respectively a thin and a wide. A piece of crumpled graphene was half flat and half crumpled, marked in green. Another piece had rolled into a nanoscroll. **(b)** A higher magnification of the area marked in (a). Iron oxide nanoparticles can be seen covering the whole sample. The graphene nanoscroll is bent at an angle. **(c)** An area nearby (b), where a grain boundary is marked. In the inset SADP, the brightest pattern is from the grain on the right and the second pattern at a different angle is from the graphene grain on the left. **(d)** SADP taken from the area in (b), showing monolayer graphene. There are also two additional weaker patterns oriented at different angles, likely corresponding to two sections of crumpled graphene.

A double layer and a monolayer intersected in figure 4.12, and two few layered pieces of crumpled graphene intersect in figure 4.13. At this resolution, interlayer lattice fringes of graphene were clearly seen, and were measured to have a spacing of 3.4 Å Lattice fringes of the nanoparticles could also be seen, measured to have a spacing of 2.6 Å.
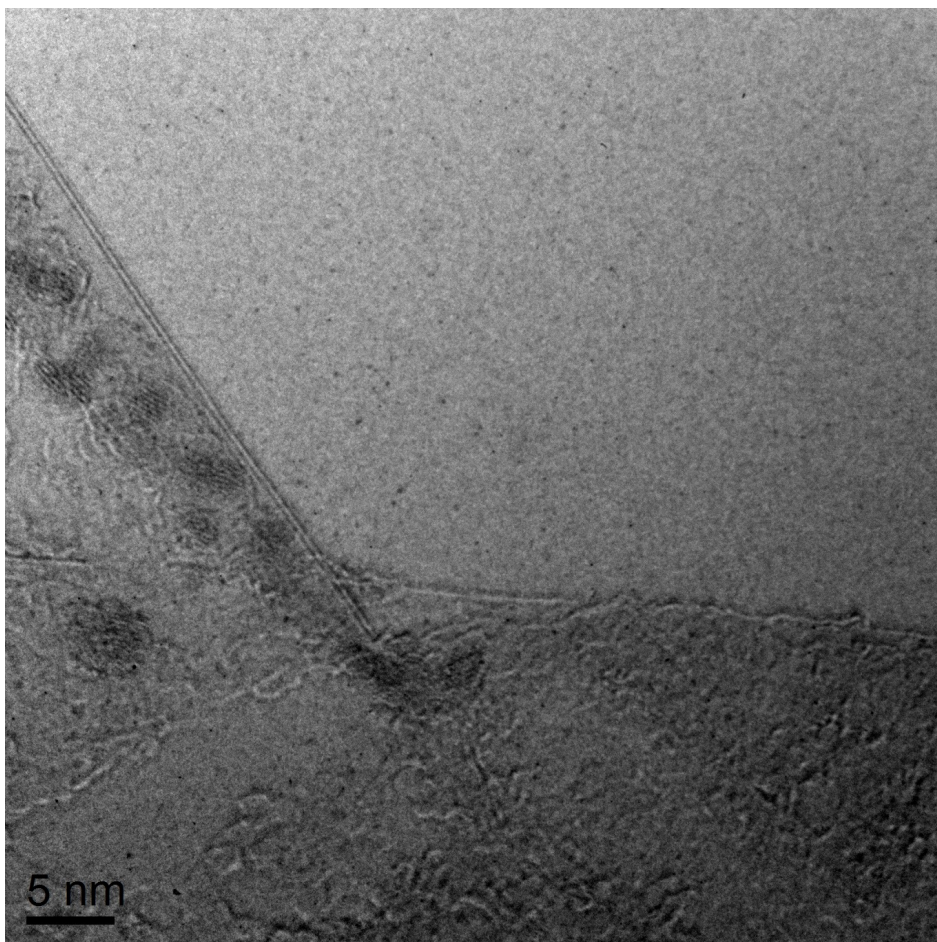
Figure 4.12: **(a)** A high resolution image of an edge of a monolayer that has folded double giving a double lattice fringe. This intersects with another monolayer.
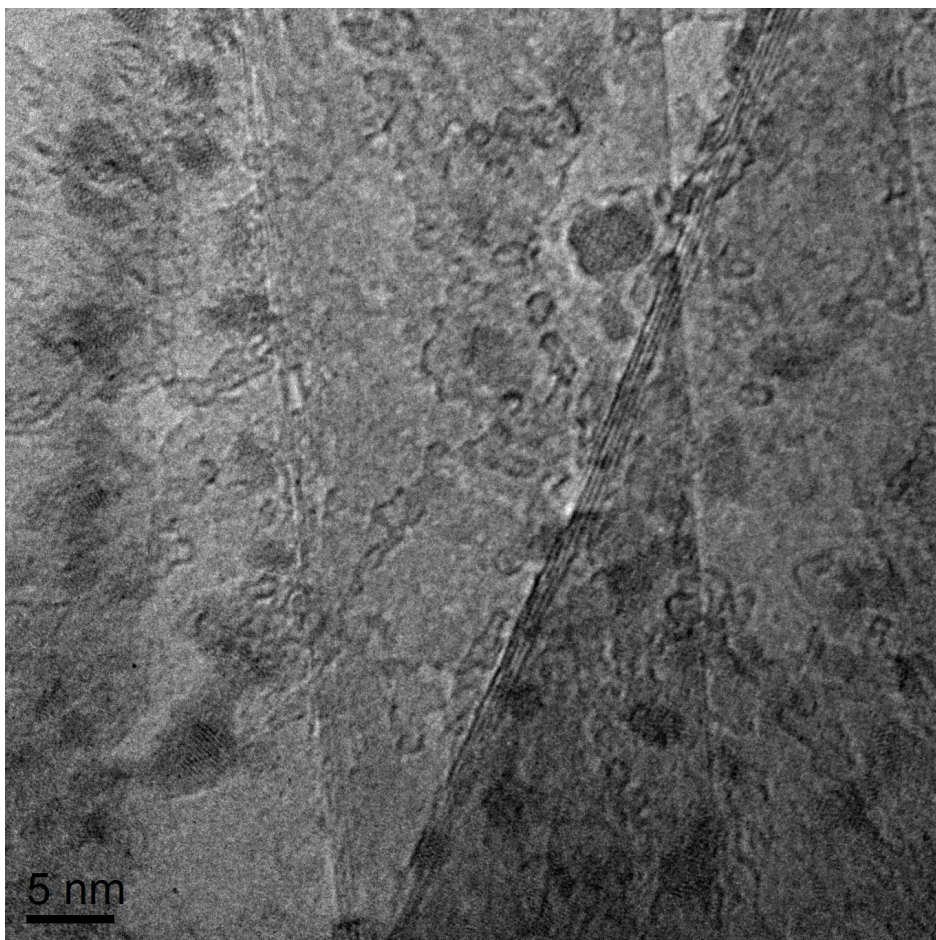
Figure 4.13: A high resolution image of two pieces of crumpled few-layer graphene intersecting atop a monolayer covered by iron oxide nanoparticles.

The effect of the irradiation from the beam on the materials can be seen in figure 4.14. In 4.14a and 4.14b, a piece of crumpled graphene had wrapped itself around nanoparticles. Along the edge of the graphene there is a clear diffraction contrast, giving bend contours. After a minute of exposure to the beam, as seen in figure 4.14b the edge has been bent, changing in brightness. At the thick graphene edge in figure 4.14c a minute of exposure to the beam made carbon contamination grow from the edge.
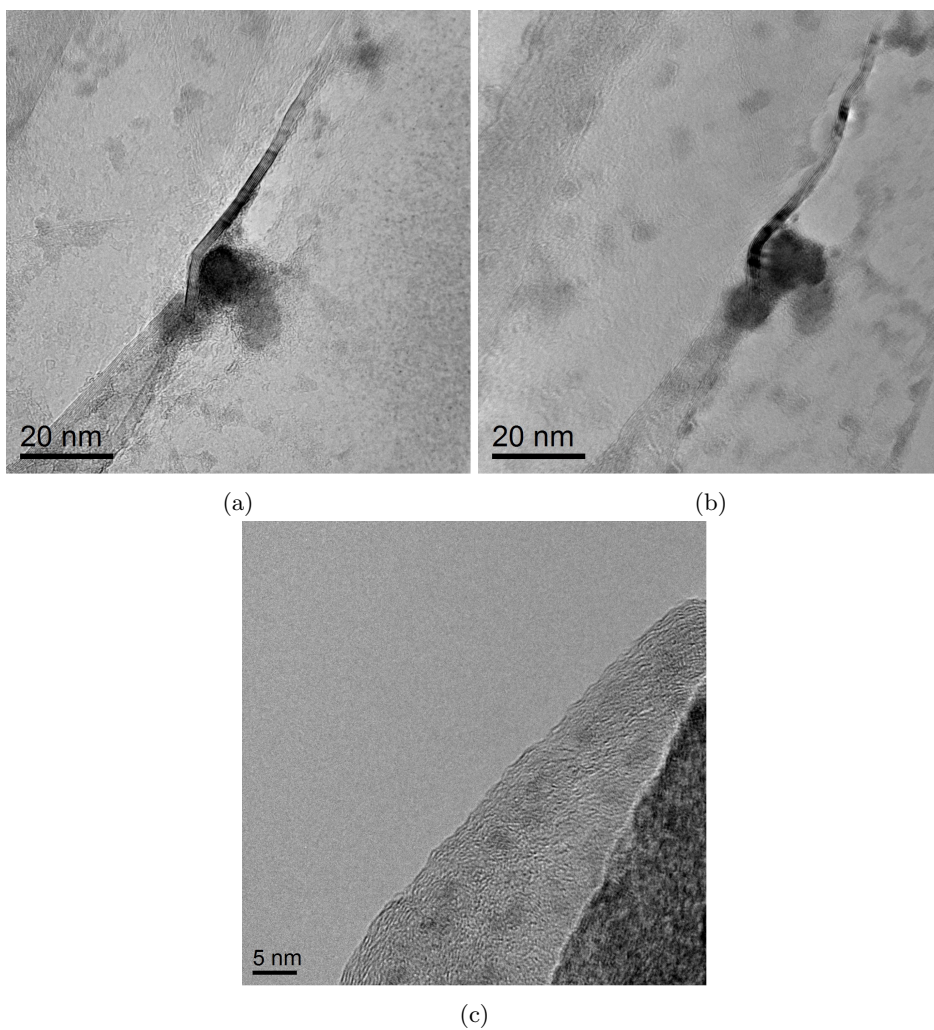
Figure 4.14: **(a)** Lattice fringes at the edge of thick (∼10 layers) crumpled graphene wrapped around what is likely three smaller ∼15 nm SiO₂ nanoparticles. Bend contours along the edge changes the colour of the edge. **(b)** Beam damage after ∼1 minute of exposure. The edge has bent significantly, changing the colour. **(c)** A thick many-layered graphene edge from which beam induced carbon contamination has started growing.

Dark Field

While studying batches 2, 3 and 5, some attempts of dark field imaging were also done. In figure 4.15 a BF image is seen, of graphene that had rolled up into a nanoscroll. Spots from its diffraction pattern were used to acquire the DF images seen in figure 4.16. In figure 4.16a, the image is formed from the spot corresponding the the interlayer distance of multilayered graphene. This gives an image of the sidewalls of the nanoscroll, but also makes some walls inside it visible. Figures 4.16b-d are taken from spots at three different orientations corresponding to the in-layer C-C distance.
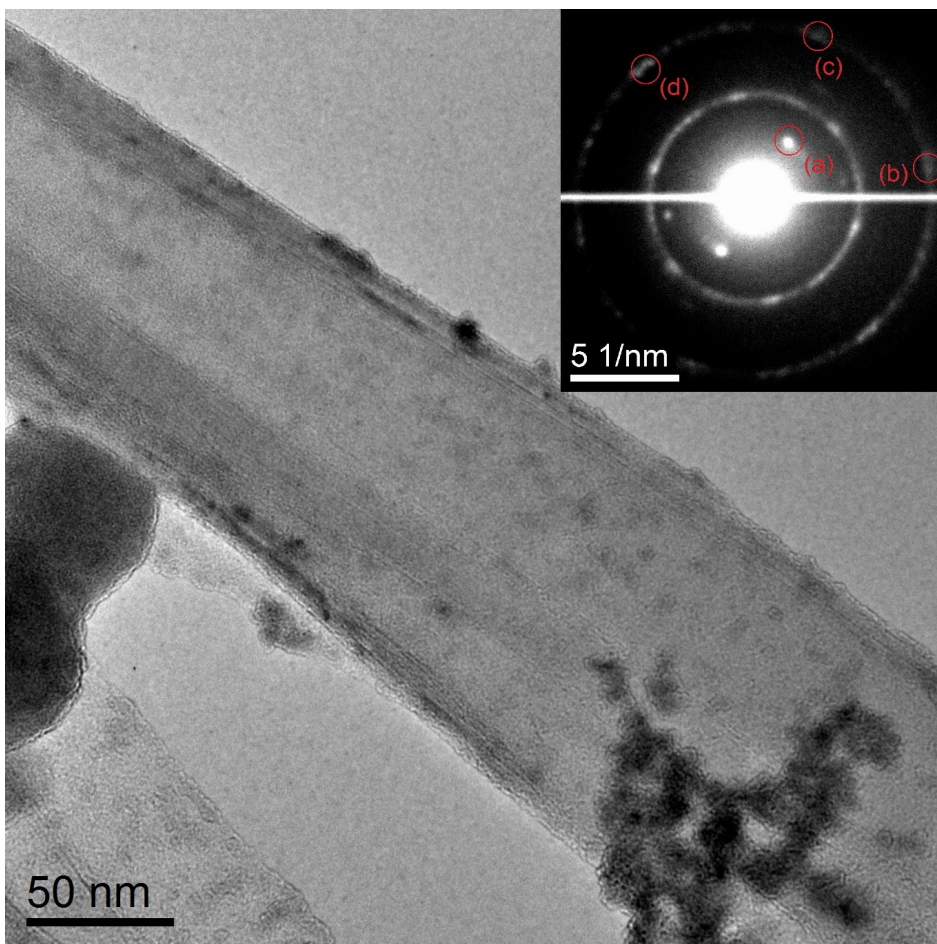
Figure 4.15: BF image of graphene that had rolled up into a carbon nanoscroll. The spots marked a-d in the inset DP from this area were used to acquire the corresponding DF images in figure 4.16.
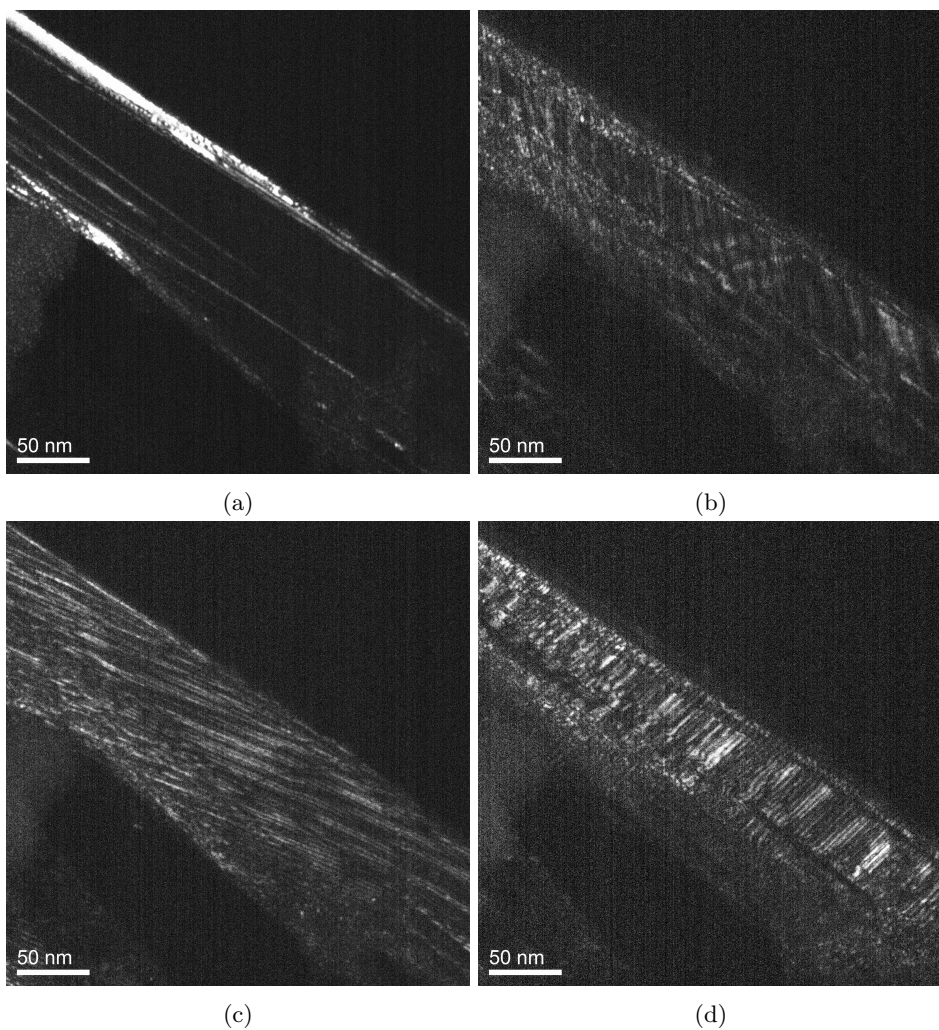
Figure 4.16: Dark field images of the nanoscroll in figure 4.15. **(a)** This DF image is taken of the walls of the nanoscroll, with the spot of the DP corresponding to the interlayer distance of 3.4 Å of multilayered graphene. **(b-d)** DF images taken of the three different orientations of the hexagonal lattice.

Growth at 1030°C

Images of graphene transferred from a Cu foil control sample in the Cu-TF experiment at 1030°C, are seen in figure 4.17. In figure 4.17a a monolayer graphene was suspended between two domains of thicker carbon. The edges of the carbon lacked the straight parallel lattice fringes seen in the monolayered and crumpled graphene. It was rather observed to have irregular fringes, varying from a few to tens of layers, and was thus likely not highly crystalline. The monolayer was seen to be full of nanometer sized holes, making the graphene very fragile.

(a) (b)
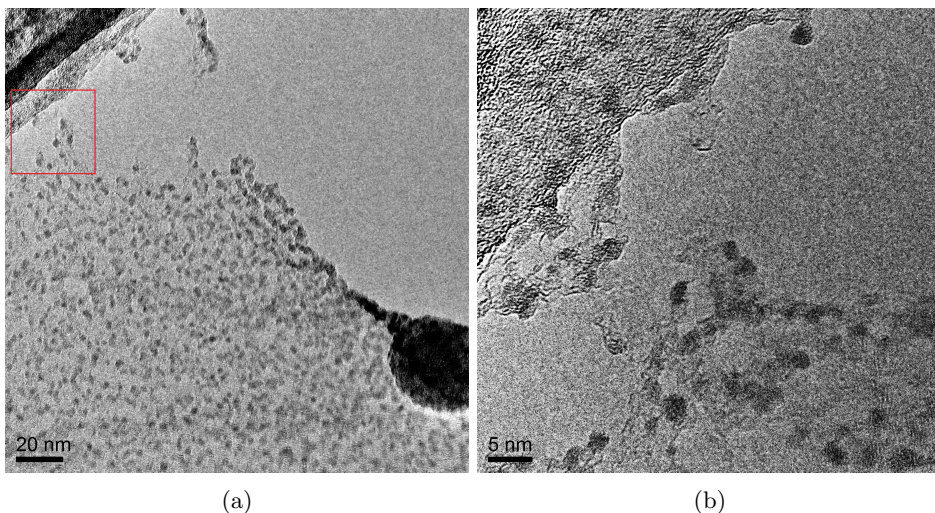
Figure 4.17: Images from the graphene grown at 1030°C. **(a)** A sheet of monolayer graphene, that had likely grown from from the SiO_2 particle, is suspended between two areas of thicker carbon. **(b)** A magnified image of the area marked in (a). A thin ribbon of graphene holding up the sheet of monolayer graphene. After 10 s exposure to the beam, the ribbon had fallen apart.

4.1.3   High Resolution Transmission Electron Microscopy

Due to its higher resolution imaging and high precision EDX and EELS capabilities, the aberration corrected TEM was used to study the nanoparticles and other nanoscale contamination of graphene from batch 5. A BF image is seen in figure 4.18. The inset SADP shows this area was covered by a monolayer. A higher magnification on the same area after 7 min of irradiation, is seen in figure 4.19. In the image, nanoscale fragments of graphene-like carbon are also seen covering the graphene. Two such areas of graphene fragments are marked in figure 4.19. One follows the orientation of the primary graphene layer and is likely AB stacked. The other seems rotated in a different orientation, causing a Moiré pattern.
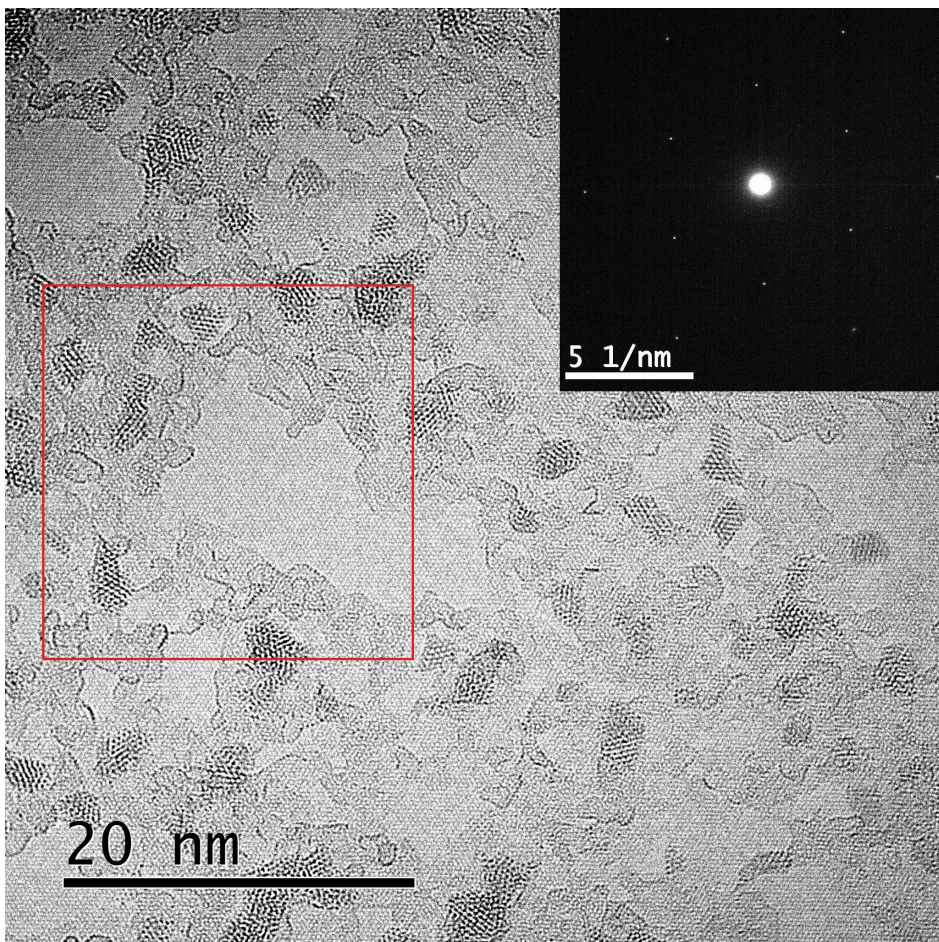
Figure 4.18: HRTEM image showing the atomic lattice of monolayer graphene and iron oxide nanoparticles. Inset is a SADP taken in this area. The marked area is shown at higher magnification in figure 4.19.

EELS mapping

In figures 4.20 and 4.21, an area was studied by EELS and EDX. A BF image of the area is in figure 4.20a. The EDX spectrum of this area in figure 4.20b, indicates the presence of C, O, Si and Fe (Cu is most likely from the TEM grid). EELS spectra are seen in figures 4.20c 4.20d, again showing C, O and Fe (Si is at a lower energy outside the range studied). Figures 4.21a and 4.21b are EELS maps of respectively C pre-peak and post-peak. Comparing these, we can see the nanoparticles clearly are not of C. The post-peak map also show the thickness of carbon, as given in the inset intensity profile. Comparing the Fe pre-peak and post-peak maps in respectively figures 4.21c and 4.21d, we clearly see the nanoparticles are of Fe.
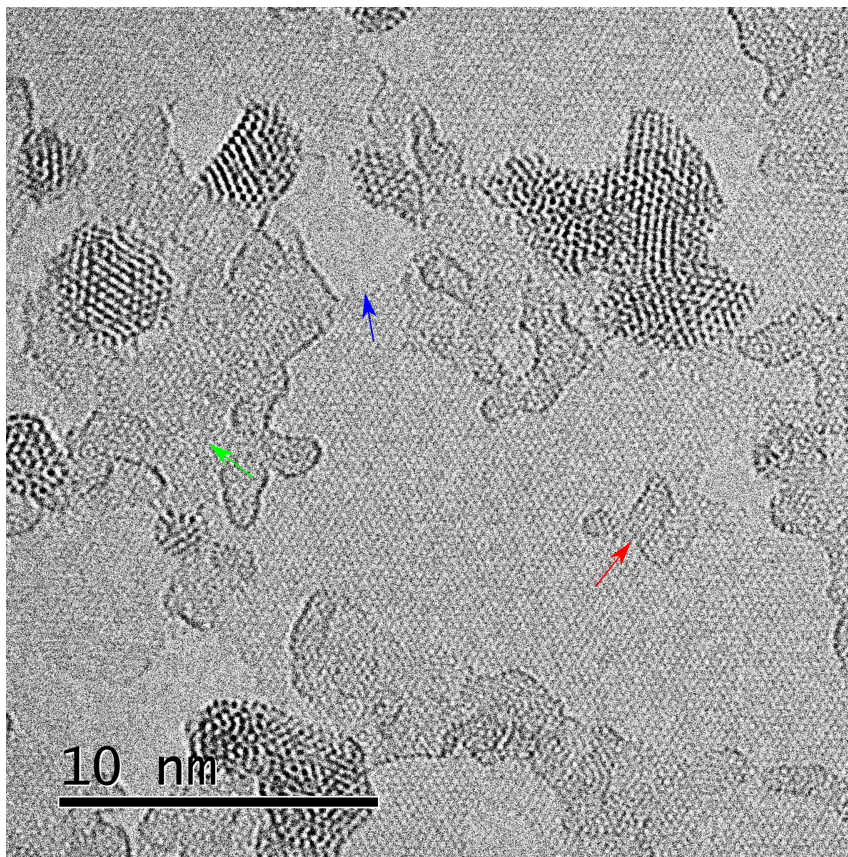
Figure 4.19: Higher magnification image of the area marked in figure 4.18. This area has been significantly altered by the e-beam. The graphene is also seen to be contaminated by small fragments of secondary graphene. A small fragment oriented along with the underlying graphene is marked red, and a larger fragment at a different orientation is marked green. A hole in the graphene is marked blue.
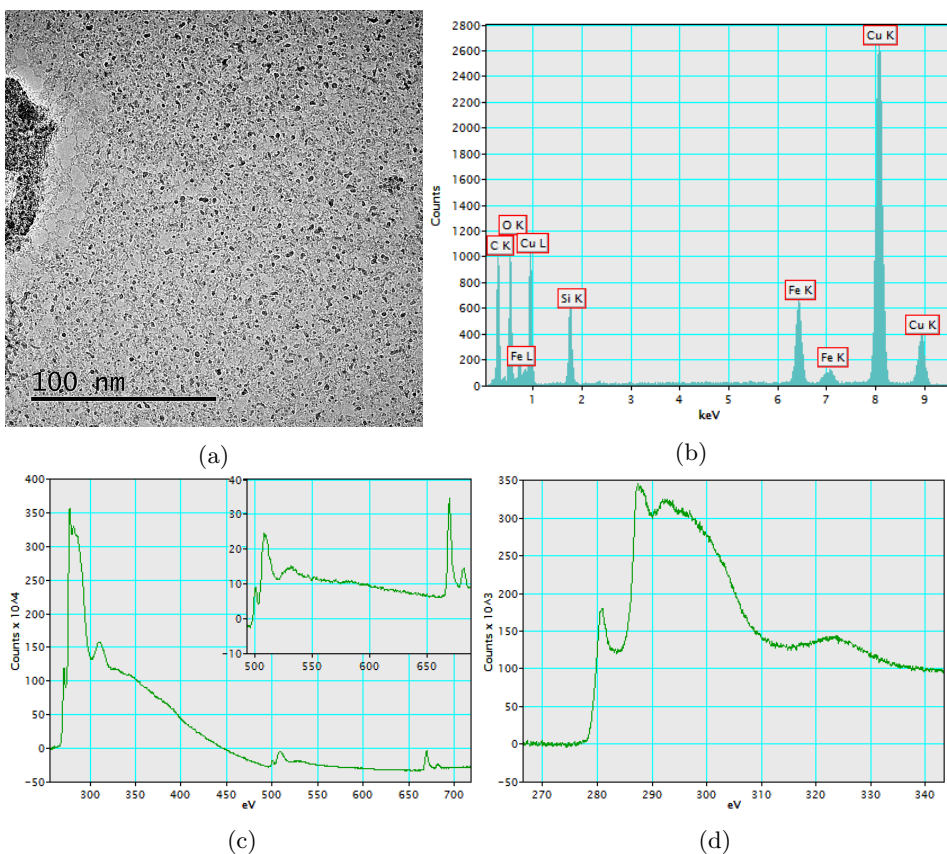
Figure 4.20: EELS and EDX measurements **(a)** BF overview of the area studied. Most of the area is a graphene monolayer with iron oxide nanoparticles. On the left edge is a SiO_2 nanoparticle. **(b)** EDX spectrum, where the C peak is from the graphene and Cu from the TEM grid. Si and O are from the particle on the left, while Fe is from the smaller nanoparticles (and likely also O). **(c)** EELS spectrum with magnified insert of the higher energy region. At 280 eV are the C peaks, at 500 are O peaks, and at 670 are Fe peaks. **(d)** Magnified C peaks at 280 eV.
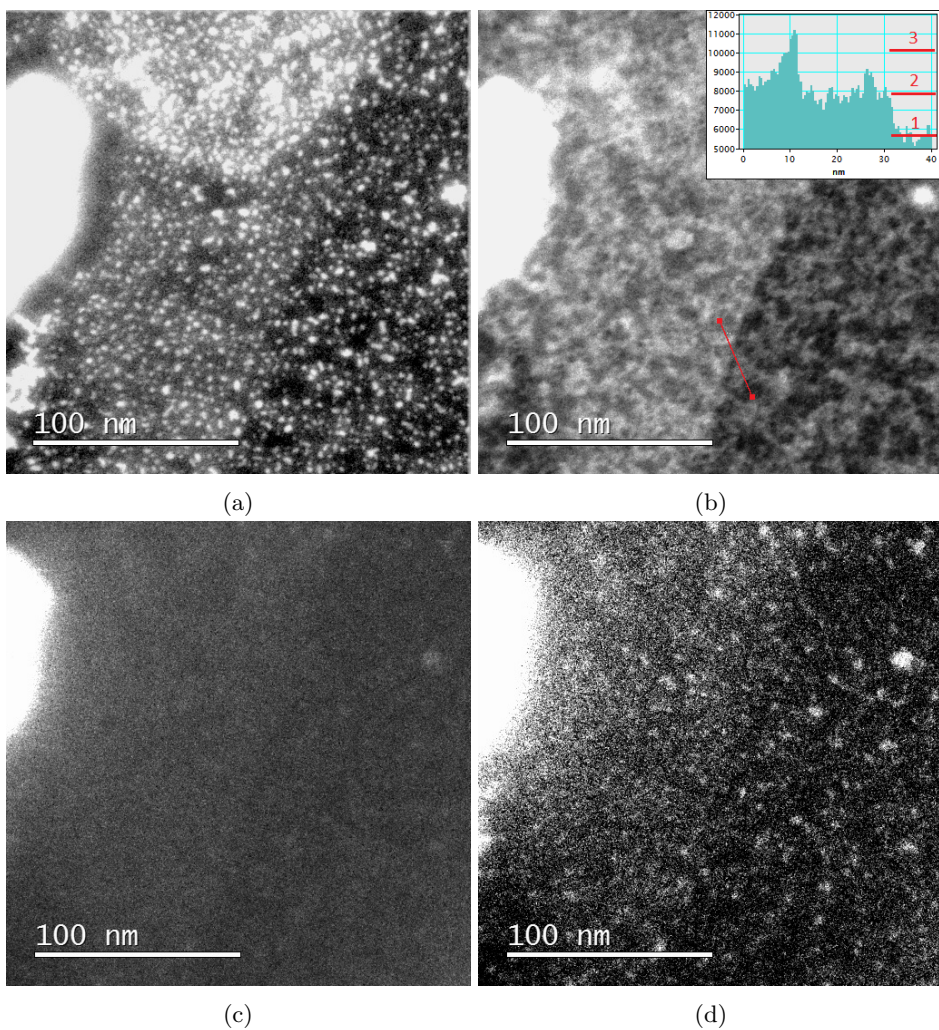
Figure 4.21: EELS mapping. The brightness of the SiO_2 particle in all images is due to its thickness. **(a)** pre-C k-peak (235-255 eV). **(b)** C-post k-peak (280-300 eV). Inset is the intensity profile along the red line, with 1, 2 and 3 layers marked. **(c)** Fe-pre k-peak (638-678 eV). **(d)** Fe-post k-peak (692-732 eV).

Scanning Transmission Electron Microscopy

The TEM was also operated in STEM mode for high precision EDX. A HAADF-STEM overview is seen in figure 4.22a. The EDX spectrum of the particle in the marked are, given in figure 4.22c, clearly show it is made of Si and O. A high resolution image showing the smaller nanoparticles, is in figure 4.22b. The point EDX measurement in figure 4.22d, show the particles to be of Fe.
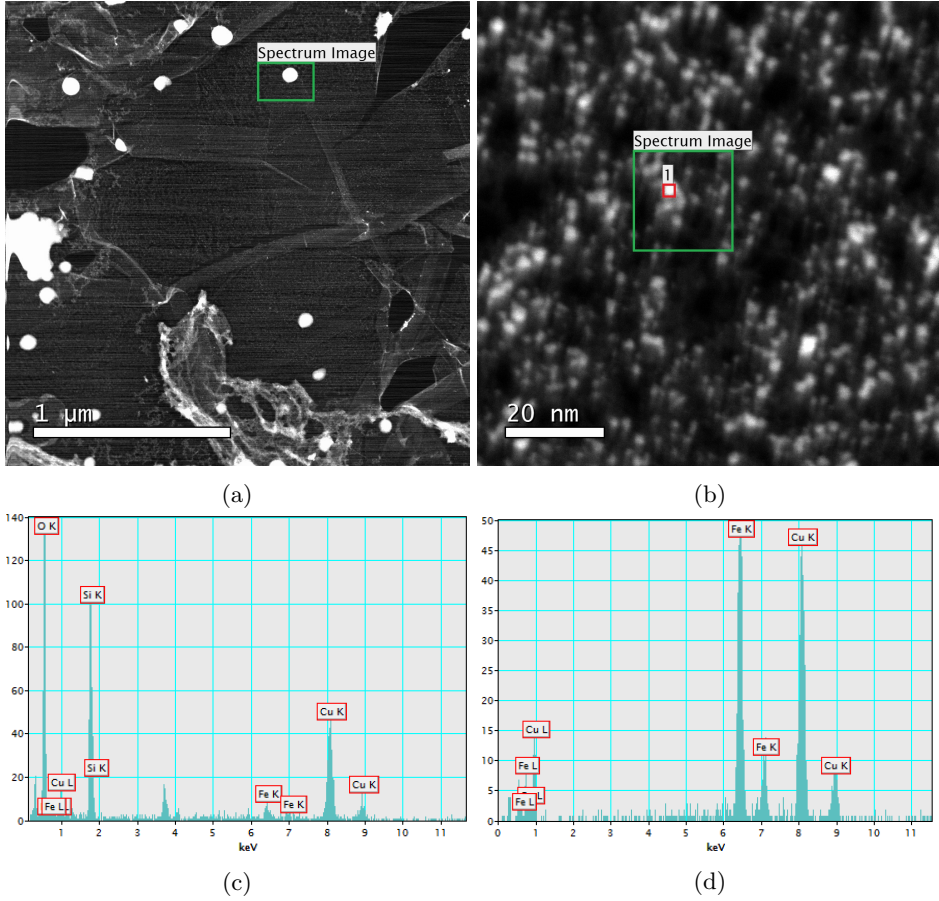
Figure 4.22: HAADF-STEM images with EDX measurements. **(a)** An overview image, where an EDX mapping was performed in the marked area. **(b)** A higher magnification image showing Fe nanoparticles. **(c)** EDX measurement extracted from the SiO_2 nanoparticle inside the mapping area in (a). **(d)** EDX measurement extracted the from particle marked "1" in (b). in both EDX measurements, the Cu signal is most likely from the TEM grid.

4.2   Graphene on Copper Thin Film

In this experiment, two pieces of Si wafer had a 100 nm Cu film e-beam deposited, before CVD (as explained in Methods section 3.1.2). One of these samples was studied by profilometer, shown in figure 4.23. To create a sharp edge for measuring the thickness of the film, an area of the Si wafer was covered by permanent marker before EBD. Then after EBD, lift off of the Cu-TF on the marked area was done by putting the sample in an acetone bath in an ultrasonicator. In the measurement of the edge in figure 4.23a, we can see the TF is about 95 nm thick. From both measurements we can see there are some nanoscale roughness, likely nanoparticles sized ∼5-30 nm.

A SEM study of the second sample was done after CVD, seen in figure 4.24. In the overviews in figures 4.24a and 4.24b, much Cu is seen to remain, but appear to have dewetted, forming a fractal branching structure. In between the Cu branches, the surface of the surface of the Si wafer is seen. In the higher magnification image in figure 4.24c, graphene wrinkles can be seen on the Si surface, indicating there is at least one layer of graphene covering the sample.

(a)   (b)
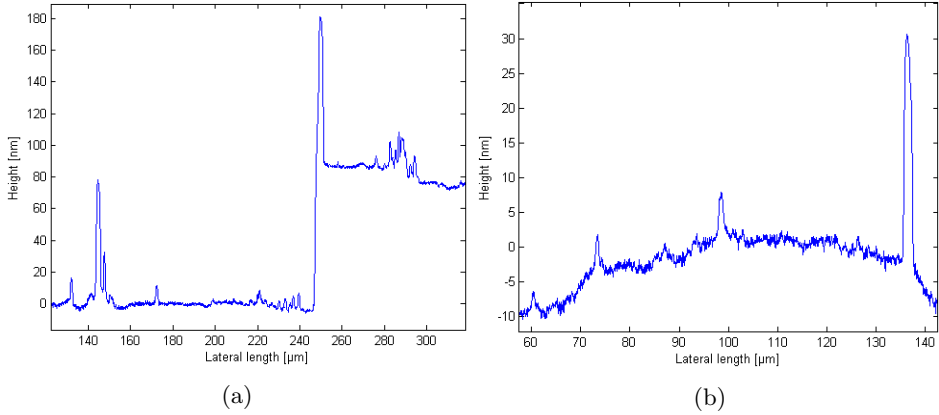
Figure 4.23: Profilometer measurements after deposition of Cu-TF, before CVD.
(a) Measurement over the edge of the TF. **(b)** Measurement at the flat surface of the TF.
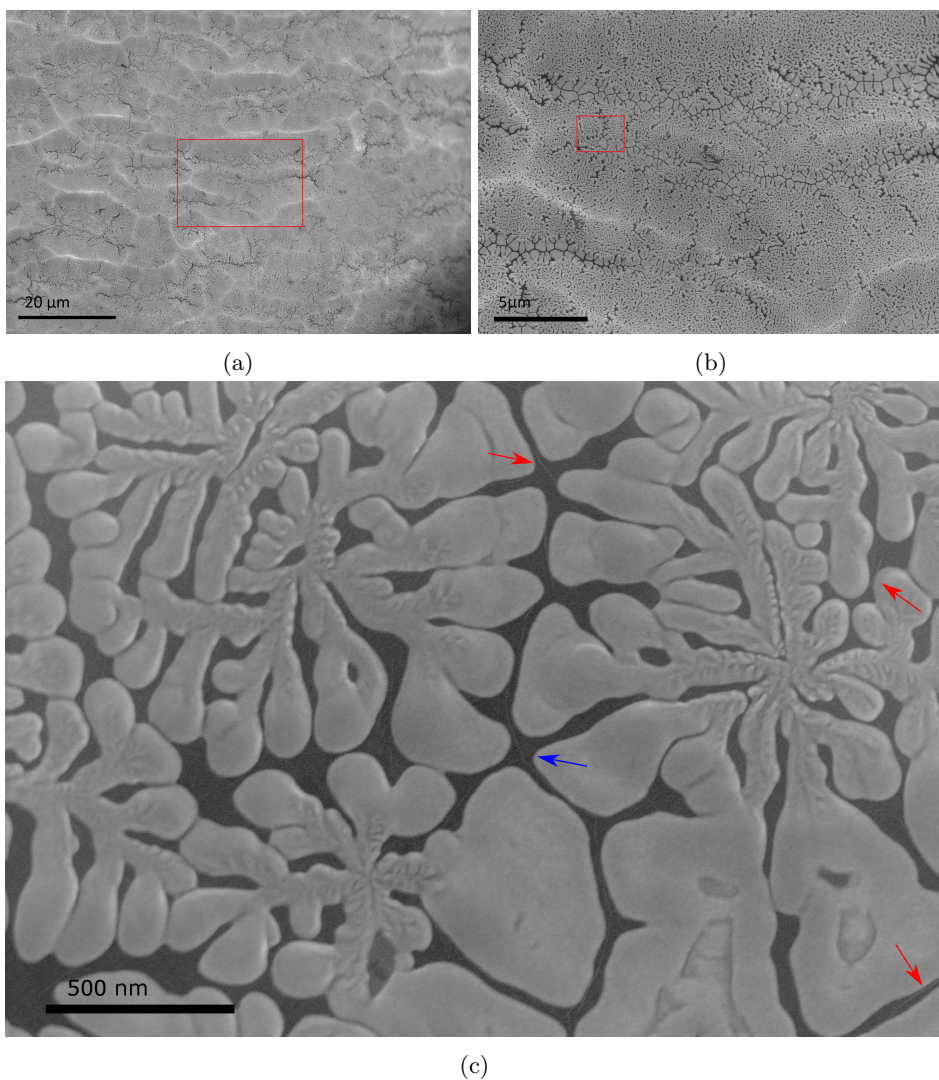
Figure 4.24: SEM images of the Cu-TF after CVD. All images taken at 30 kV. **(a)** Overview of the surface. **(b)** Magnified area marked in (a). **(c)** Magnified area marked in (b). Note the thin bright lines of graphene wrinkles in the dark gaps. Two such intersecting wrinkles are marked with the blue arrow. Three other visible wrinkles are marked in red.

Chapter 5

Discussion

The discussion is in two parts. First about CVD on Cu foil, where optimization of the CVD process, the transfer process, particle contamination, are discussed. Contrast and operation of SEM and TEM for these samples are also analysed. Secondly, the process of CVD on Cu thin film is discussed.

5.1 Graphene on Copper Foil

After CVD, samples from the 5 batches in table 3.1 have distinct differences in their appearance. Samples from batches 1 and 4 appeared matte metallic gray in colour, due to being heavily contaminated with particles. Samples from batches 2, 3, and 5 appeared similar to the original Cu foil, but were slightly darker in colour due to the presence of graphene and/or slight particle contamination. After every experiment, areas of the CVD quartz tube near the samples appeared Cu coloured, indicating a significant amount of Cu had evaporated and covered the quartz.

The study by SEM indicated that samples in batches 1, 2, 3 and 5 were covered by monolayered graphene and contaminated by particles. Considering batch 4's similarity to batch 1, there might also have been graphene present, but more likely only amorphous carbon particles. In batches 2, 3 and 5 the nanoparticles were seen to have acted as nucleation sites for a second incomplete layer of graphene.

The results demonstrate that graphene wrinkles are possible to see using SEM, but were often only partially visible. The heat treatment of the CVD process made the surface of the Cu foil restructure into a step-like pattern, that made distinguishing the features of graphene from the features of the Cu surface difficult. Transferring the graphene onto a flat Si wafer surface made the graphene grain boundaries distinctly visible, enabling study of graphene grain size, see figure 4.8.

Samples 2, 3 and 5 were studies by TEM. From SEM, it was not clear if the graphene was monolayered, but this was seen clearly in all three batches in TEM. EDX and EELS were used in the HRTEM to determine that the ∼100 nm particle contamination from CVD was SiO_2, while the ∼5 nm particles were iron oxide, remnant from the etching process, seen in figure 4.19. These could have been avoided with a better rinsing or a different etching process. In TEM and HRTEM there was also seen a significant presence of one or more additional incomplete graphene layers.

5.1.1 CVD Optimization

The purpose of the 5 CVD batches was to try to improve the procedure for CVD growth, as the CVD system was newly acquired and little experience had been built up at Nanolab to that point.

Batch 1

In batch 1 the parameters given in table 3.1 were used, as they were given by the GrapheneSquare, the manufacturer of the CVD. In addition, the samples were loaded on a stainless steel stage. SEM images from this batch are shown in figure 4.1. The surface was dominated by two types of particles. The Cr nanorods seen in figures 4.1a and 4.1b, came from the stainless steel stage holding the samples. Curiously, these rods were almost exclusively observed to grow along the surface at 90° angles relative to each other. This suggests there is a signification crystallographic interaction with the surface during growth. However, both expected surfaces, graphene and the predominant orientation of the Cu surface, (111), are hexagonally structured. At this stage it is unclear what is the cause of 90° between the contaminating Cr particles, but it is outside the scope of the present work to investigate this further. As these rods were made of Cr that had evaporated from the stainless steel due to the high temperature and low pressure, this contamination could be removed by removing the steel from the CVD chamber, as is demonstrated by the growth and characterization of the following batches.

A second type of particles, sized 10s of nanometers across, were also present covering most of the sample. These are seen to give most of the bright contrast in figures 4.1a and 4.1b. A few areas held less nanoparticles, and can be seen in figures 4.1c and 4.1d. In these images, clusters of a few particles can be seen in higher magnification, but the particles were too small to study in detail by SEM. The particles were likely amorphous C, as there was a significant carbon signal in EDX, but this might be a contribution from graphene.

In these images, indications of graphene can also be seen. In figure 4.1b, there are some dark stripes, as if shadows from elevated plateaus in the surface. The same contrast is seen more in detail as a branching pattern in figure 4.1d (also

similarly, but vaguely visible in figure 4.1c). This contrast is likely due to graphene "hanging" from the nanoparticles like a tent above the Cu surface, as is illustrated in figure 5.2. Along these branching patterns thin bright lines can be seen, which are wrinkles in the graphene. This is discussed further in section 5.1.4 below.

It is difficult to conclude how these nanoparticles have formed underneath the graphene. As this is not seen in the later batches without the steel stage, it is possible these nanoparticles are of a third type, formed of Cr or a different alloying element if the steel. A possible explanation could be that Cr had diffused into the Cu surface during the pre-CVD high temperature annealing. Then, during post-CVD cooldown, this has then segregated out from the Cu and formed nanoparticles.

Batches 2, 3 and 5

Due to the contamination from the stainless steel stage, in the remaining experiments it was replaced with a quartz glass stage. In both the following SEM and TEM studies, samples from the three batches looked very similar. A representative SEM overview image of the surface after CVD is seen in figure 4.2. Compared to the images of batch 1 in figure 4.1, we here see there are still some contamination of particles, but much less than before. These nanoparticles were identified to be SiO_2 (see section 5.1.3).

There are some indications of the surface being covered by a continuous layer of graphene, as some wrinkles in the graphene are visible. These are seen in more detail in figure 4.3. There are also dark domains of a second incomplete graphene layer, as is seen in detail in figure 4.3b. The domains were usually seen to be roughly circularly shaped, but some domains had $120°$ edges, as is typical of regularly reported hexagonal graphene.[93,94,95] These domains were seen to mostly surround the nanoparticles or have a nanoparticle at its edge, indicating the particles acted as a nucleation site for the graphene domain. But many particles were also not surrounded by a graphene domain, and many domains seem to have formed without a particle, indicating both the particles and domains can form without the other. The particles also often formed structures such as the line of particles seen in figure 4.3c, which indicates the particles have interacted with features of the Cu surface, such as scratches. The absence of a tent-like contrast such as was seen in figure 4.1d of the first batch, indicates the particles are all on top of the graphene.

Multiple subsequent growth mechanisms can explain how these features forms. The particles form first and act as a nucleation site for both the primary and secondary graphene layers. Or the complete graphene layer forms first, then the particles, which then nucleates the secondary graphene. It is also possible that both layers of graphene forms first, then the particle-forming species collects at the domains to nucleate the particles.

When the particles were first seen in batch 2, they were incorrectly thought to be of amorphous carbon, as they were too small to be precisely identified by the EDX in the Hitachi STEM (later determined to be SiO_2 by using the aberration corrected TEM). Because of this, the main purpose of batches 3 - 5 in table 3.1, was to find procedures to limit the formation of particles and secondary graphene, by reducing the growth time and CH_4 partial pressure. From the table we see that batch 3 had a growth time reduced from 25 to 10 minutes, while the CH_4 pressure was doubled, meaning the total amount of CH_4 exposed to the Cu surface was not reduced very much. In batch 4, the low CH_4:H_2 ratio likely caused amorphous carbon to form instead of graphene. Batch 5, compared to batches 2 and 3 had a much lower CH_4 flow.

Despite the different parameters, little difference was seen in the SEM study between the batches 2, 3 and 5. Within every sample, the concentration of particles and secondary graphene domains varied significantly over the sample area, where domains typically covered between 5-50% of the local surface area. This makes it difficult to quantify and compare the amount and size of particles and domains between the different batches, by a representative number. But from general SEM and TEM observation of the samples, there seemed not to be a very significant difference in neither particles nor domains between the three batches. Additionally, in the TEM studies, monolayer graphene edges, such as for example seen in figure 4.12, were most common and representative of all the three batches. This leads to the conclusion that the primary graphene growth self terminated after a complete monolayer had formed. It is likely possible to grow a continuous monolayer with significantly less CH_4 exposure to the Cu surface, through reducing one or both of the CH_4 partial pressure and growth time.

Overall, it is difficult to give a conclusion for how the optimization has affected nucleation density and grain size of the primary graphene. Neither SEM of the Cu surface or TEM were useful for studying graphene grain boundaries, as these were only clearly visible after graphene was transferred onto a Si wafer surface, seen in figure 4.7. These were observed to range from a few 100s of nm up to 1 µm in size. But this was only done for batch 3, so there is no data available for comparison from the other batches.

As for why the domains of secondary graphene did not change between the batches, this is difficult to explain, as no other reports of the graphene growth with SiO_2 particles have been found. I can possibly be explained by the domains forming not during the graphene growth period of the process, but forming from carbon accumulated at high temperature at or in the SiO_2 particles. Then during the cooldown phase, the carbon precipitates forming the graphene domains. Because the carbon accumulation would saturate at the SiO_2 particles during the growth phase, the size of the domains is only dependent on the size of the SiO_2 particle. Then, as the formation of the particles is largely not dependant on the growth time (see section 5.1.3), the size of the graphene domains should also be the same in the three batches. However, this theory is also difficult to confirm based on the

experimental results and facilities available. While the domain size is dependent on the particle size during the growth phase, the particles also keep growing after the growth phase. Therefore, the domain size, as seen in SEM images, would not match the final particles size.

Growth at 1030°C

An additional batch of samples were also exposed to very different CVD conditions, as a control to the Cu thin film experiment. See section 3.1.2 for the parameters of the experiment and section 5.2 for discussion about the effect of the parameters had on Cu. Compared to the previous batches, the CVD process was run at a temperature 30∘C higher at 1030°C, with a following evaporation phase where the chamber pressure was reduced.

SEM images of the surface of the Cu after CVD are seen in figure 4.6. Comparing the overview in figure 4.6a to the images of the previous batches seen in figures 4.2 and 4.3, we see there are similarities but also significant differences. From the fluid-like patterns seen in all the images of figure 4.6, and the particles seen in figure 4.6b having ordered in steps, it is clear that the Cu surface has formed a stepped structure like in the previous batches. But upon closer examination in figures 4.6c and 4.6d, the Cu steps are missing. It is likely the uppermost surface of the Cu foil had evaporated during the evaporation phase of the process, forming a smooth Cu phase.

However, the particles and bright domains had formed during the growth phase of the process when the steps were still present, and were thus structured by the steps. In figure 4.6d, two types of bright domains are visible. The darker of the two were most common and has not been seen before. These were highly anisotropic and there seem to be distinct gaps where such domains had not grown together. It is likely the domains grew along the edges, not being able to grow across either the edges or the valleys between the edges. In the higher resolution TEM study (figure 4.17), the thicker domains were seen to have irregular edges, varying from a few to tens of layers. It was therefore unlikely graphitized C, but rather amorphous. In figure 4.17b, a monolayered domain is seen. These were seen to be riddled with nanometer sized holes, making the graphene fragile to the 80 kV electron beam.

In figure 4.6d particles are seen to have formed between the patches, and in figure 4.6b the particles have formed lines. From this it is likely the particles have a strong preference for forming at either the edges or the valleys of the surface. During the CVD phase, the primary C domains formed with a particle at its edge, growing along the edges of the Cu surface. The second, brighter graphene domains hence formed later upon cooldown, after the Cu surface have flattened, of C segregating from the SiO_2 particles. The secondary domains fills the gap between the primary domains. In figure 4.6d, the edge of the secondary domains are seen to have a concave edge, similar to the meniscus of the surface of water in a glass. This

indicates the secondary graphene grows along the edge of the primary C domains, minimizing the surface energy.

In contrast to previous batches, there were no signs of wrinkles, a telltale sign of a continuous graphene layer. Therefore the graphene growth has likely been inhibited by a high rate of Cu evaporation. The primary carbon domains have in stead grown to become thicker layers, while the secondary domains are likely monolayered. This explains the two domains having different brightness.

Growth at the underside of the Cu foil

Crumpled graphene was observed on samples from batch 2 that were transferred onto grids for TEM studies (see figure 4.10). Following this, on one of the samples from batch 3, the underside of the Cu foil was studied in SEM for signs of graphene. This side of the Cu foil had faced down towards the quartz glass stage, in the CVD reactor. It had thus been exposed to a different environment during CVD. As the Cu substrates had an uneven surface, much of the surface was not in contact with the stage, permitting flow of CH_4 along the surface. However the gas flow to the underside was likely at a reduced rate and with the CH_4 exposure more uneven, compared to the upper side.

SEM images from the underside are shown in figure 4.5. In the overview in figure 4.5a, we see there was a highly uneven colouration due to the varying density of secondary graphene domains. This varied much more than what was observed on the upper side of the foil. At a higher magnification, for example in figure 4.5b), the local area looked very similar to how the upper side looked (as seen in figure 4.2. From this, it is reasonable to conclude that in all batches most of the surface on the underside is similar to the other side. The added particles and crumpled graphene was an unwanted contaminant in samples that had been transferred. So because of this, before etching the remaining samples from batches 3 and 5, these were plasma cleaned, with the underside facing the plasma.

5.1.2 Etch and Transfer

The purpose of the etching and transfer process was, as explained in Methods section 3.2.1, to move the graphene from the Cu substrate onto other substrates. Ideally, such a technique should transfer onto any sort of substrate, without causing tears or wrinkles in the graphene, degrading the material's properties. It should also not introduce any additional contaminants. In this work, graphene was transferred onto TEM grids, Si wafer and quartz glass.

The transfer to quartz glass and Si wafer were for studying the graphene independently from the Cu substrate in SEM. The quartz gave poor images due to charging, but SEM images of graphene transferred onto Si are shown in figure 4.7. On this sample, some cracks and many wrinkles were caused by the transfer,

but most of the wrinkles likely originated from the Cu shrinking during cooldown. There were also µm-sized areas where the graphene had folded onto itself during transfer. The most significant effect of the transfer was that the graphene from the underside of the Cu foil crumpled onto the flat graphene layer, as seen in figures 4.7a and 4.8. This was unwanted, as ideally this process should yield just an even monolayer. The transfer seemed to not have a very significant effect on the amount of SiO_2 nanoparticles. Some were likely washed away, but more were also added along with the crumpled graphene, as indicated by the presence of particles underneath the graphene.

The transfer onto TEM grids had a similar result, but as seen in figure 4.10a, micrometer sized holes had been torn in the graphene. These were likely caused by the capillary forces of the water droplets drying on the suspended graphene. Furthermore, as seen in the higher resolution figure TEM images in figures 4.18 and 4.19, the $Fe(NO_3)_3$ left Fe-based nanoparticles across all samples that were transferred.

After finding the crumpled graphene on the TEM grids and Si wafer, it was found to mainly originate from the underside of the Cu foil. The graphene on the underside, as seen in figure figure 4.5, had also grown less even and controlled. The following samples of batches 3 and 5 were therefore plasma cleaned before etching, to remove this graphene. This was done by exposing the underside of the Cu foil to 60 s of O_2 plasma. This was observed to reduce the amount of crumpled graphene, but as seen in figures 4.11a and 4.22a, there are still crumpled graphene in batch 5. Therefore, a stronger plasma clean should have been done. Samples in batches 3 and 5 were also O_2 plasma cleaned twice for 10 s in a Fischione 2010 plasma cleaner with a shielding holder, to remove hydrocarbon contamination.[92]

5.1.3   Particle Contamination

All the samples examined have been contaminated by different nanoparticles of various sizes. First seen are the particles covering the sample from CVD batch 1. In this sample there are primarily two types of particles. One type is the nanorods sized around 1 µm wide and tens of µm in length, as seen in figure 4.1a and 4.1b. The rods are hexagonally faceted, and therefore crystalline, and are seen to grow along the Cu surface at angles $90°$ relative to each other. This is indicative of the rods interacting strongly with the surface during growth, but the angle is curious considering the lowest energy surface of Cu is (111) which is hexagonal, not cubic. These rods were identified by EDX to be made of Cr. The source of Cr was found to be the stainless steel stage, onto which the Cu foil samples were placed in the CVD chamber. The smaller nanoparticles are seen in figure 4.1d to be sized less than 50 nm. In figure 4.1b, the nanoparticles were seen to almost continuously cover most of the sample, obscuring the Cu surface and graphene. These particles were to small to characterized precisely by EDX in the SEM, but the EDX indicated they were amorphous carbon.

In the remaining batches 2, 3, 5 and the samples grown at 1030°C, different particles were observed. As seen by SEM in figure 4.3c, there were particles sized around 50 - 100 nm, which varied in concentration and were either spread randomly or aligned to structures on the surface. The particles also seemed to be the cause of the secondary graphene domains. The particles were first thought to be Cu or amorphous C, but they remained after Cu had been etched during the transfer process (see figure 4.10b), excluding Cu. At high resolution in figure 4.10d, they looked amorphous, as would be expected of C particles. However, the particles were conclusively identifies as SiO_2 by using high resolution EDX in STEM mode, seen in figures 4.22a and 4.22c. The particles likely originated from the quartz glass of either the stage holding the samples or the CVD chamber walls. The combined heat and low pressure of the process had caused the SiO_2 to evaporate. Curiously, in the Cu-TF experiment these particles only appeared on the Cu foil control (figure 4.6), and not the Cu-TF (figure 4.24). This indicates the particles form because of a feature of the Cu foil, which might be impurities alloyed in the metal or surface roughness from the machining of the foil.

Lastly, as was seen in high resolution TEM images (figures 4.12 and 4.13), the graphene has been contaminated by nanoparticles from the etching process. In these TEM images, the particles were seen to be sized ∼5 nm and crystalline with a lattice spacing measured to be 2.55 - 2.64 Å. These nanoparticles were also sometimes seen to have agglomerated in areas such as seen in figure 4.11a. The particles were first thought to be diamond, like in Sun et al.[96] EELS (figure 4.21) and EDX (figure 4.22) however, showed them to be made of Fe. The aberration corrected TEM gave higher resolution lattice from the particles, seen in figure 4.19. From this and other images, lattice spacings of approximately 1.6 Å, 2.2 Å, 2.5 Å, 2.9 Å, and 3.3 Å, were measured. Comparing these to table 5.1, these spacings were too large to be pure Fe, but it does not match any of the iron oxides exactly either. It is still likely the particles are to some degree oxidized.

Table 5.1: Lattice spacings of Fe-O based crystals.

α-Fe [Å]	γ-Fe [Å]	FeO [Å]	Fe_2O_3 [Å]	Fe_3O_4 [Å]
(110) 2.027	(111) 2.080	(111) 2.49	(012) 3.684	(111) 4.852
(200) 1.433	(200) 1.800	(200) 2.153	(104) 2.700	(220) 2.967
(211) 1.170	(220) 1.270	(220) 1.523	(110) 2.519	(311) 2.532
(220) 1.013	(311) 1.080	(311) 1.299	(006) 2.292	(222) 2.424
(310) 0.906	(222) 1.040	(222) 1.243	(113) 2.207	(400) 2.099

5.1.4 SEM Contrast and Operation

In the SEM images shown in this work, graphene looks to have a thickness contrast that makes its brightness change distinctly between one, two or more layers. In figure 4.3, on a Cu surface, domains of a second graphene layer are seen to be darker than the surrounding monolayered graphene. However, when the graphene had been transferred onto Si, as seen in figure 4.8, the graphene monolayer appears brighter than the Si surface, while additional layers makes it darker. The same is also seen with the graphene domains that were grown at $1030°C$ in figure 4.6d, where the graphene domains are slightly darker than the monolayer in between.

The thickness contrast of the graphene was clearest at low acceleration voltage. Distinguishing up to 10 layers of graphene have previously been reported, using HT 0.5 - 2 kV.[97] The contrast is believed to be caused by the attenuation in graphene of secondary electrons emitted by both the substrate surface and the graphene.[97,98] Even at a low voltage of 0.5 - 2 kV, electrons penetrate through several layers of graphene and a few nm into the substrate. As additional layers of graphene are added, the upper layers of graphene absorbs more of the SE emitted by the substrate and lower layers of graphene.

From this alone it would be expected that the graphene monolayer should appear darker than the surface. This is regularly reported with graphene on a SiO_2 surface.[97,98,99] However, Kochat et al.[100] finds the contrast to reverse at low HT, with the graphene becoming brighter that the surface. They believe this is because the graphene collects charge from the beam faster than the charge in graphene is conducted to the substrate, and therefore emits more SE.

Graphene wrinkles were seen in most of the SEM images, appearing as thin bright lines such as seen in figures 4.3c and 4.3d. These wrinkles were standing up from the surface, and were thus bright due to edge contrast. A second type of wrinkles formed when the wrinkle was too high and folded onto the graphene, forming a triple-layer. These two types of wrinkles are illustrated in figure 5.1. The second, wider type of wrinkles are seen in figure 4.4 as a wider dark line. These are dark, because as they are not standing up from the surface, the edge contrast is not significant, but rather being triple-layered, the thickness contrast dominates.

Both types of wrinkles are seen on Si in figure 4.8. The wide wrinkles were seen to have a weak edge contrast from its double layered edge. Crumpled graphene also had a similar edge and thickness contrast as the wrinkles. However, the secondary graphene domains are difficult to distinguish on Si wafer. Remarkably, at high magnification, what looks to be grain boundaries in the graphene are also seen on the Si surface. These appear similar to the small wrinkles, but thinner and less bright. Given the theory that graphene appears bright due to accumulating charge, as grain boundaries inhibits conduction, it is likely that charge accumulates on grain boundaries so they appear brighter. Overall, transferring to Si was found to be very useful, as the substrate is too even to give any topological contrast like Cu does. On this surface, additional details about graphene could be distinguished.
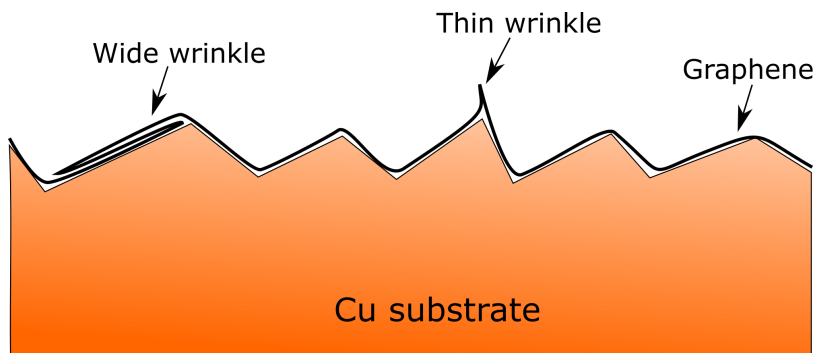
Figure 5.1: Illustrating of graphene covering a stepped Cu surface, with a thin and a wide wrinkle.

In figures 4.7c and 4.7d of graphene on Si, and in figure 4.1d from batch 1, there was an additional type of contrast from the graphene. It appears the graphene was suspended from nanoparticles under the sheet, like the canvas of a tent is hanging from tent poles. This is illustrated in figure 5.2. The contrast gives a dark gradient around some nanoparticles in the images. This same type of contrast has also been reported observed of graphene suspended from μm-sized Cu particles.[24] The contrast might be due to the angle relative to graphene, at which the electron beam passes through and the SE are emitted, causing an increased absorption of electrons in graphene.

Comparing the SE image in figure 4.7c with the LA-BSE image in figure 4.7d, LA-BSE seems to have emphasized the tent contrast. As well, the thickness contrast of the thicker crumpled graphene is also enhanced by LA-BSE. This is seen when comparing figures 4.4a and 4.4b of the Cu surface, where wrinkles in graphene that are barely visible by SE become clearly visible by LA-BSE. The thickness contrast is likely due to the high Z-contrast of BSE imaging, as C is lighter than Si or Cu. With a thicker layer of C, less electrons penetrate into the substrate, giving a lower yield of BSE. The contrast effects of the SE/BSE mixing was found to be optimal when adding 10 - 15 % BSE to the signal. This contrast of LA-BSE and explanation is similar to what was reported by Yang et al.[101]

Overall, these different highly detailed surface contrast of graphene at low HT, are reported to be due a feature of the in-lens detector due to its high sensitivity to low energy SE.[24,98,100] In comparison, an Everhart-Thornley side detector does not give a detailed surface contrast. Similarly, this was also observed with the YAG-BSE detector which unlike LA-BSE, gave no surface contrast of the graphene. The surface contrasts were mostly visible at low HT, as seen when comparing figure 4.1c at 5 kV with figure 4.1d at 1.5 kV. Where the graphene wrinkles and tent contrast are barely visible at 5 kV, they are clearly seen at 1.5 kV. Similarly in figure 4.3a at 30 kV, the contrast of the Cu surface dominates; while in figure
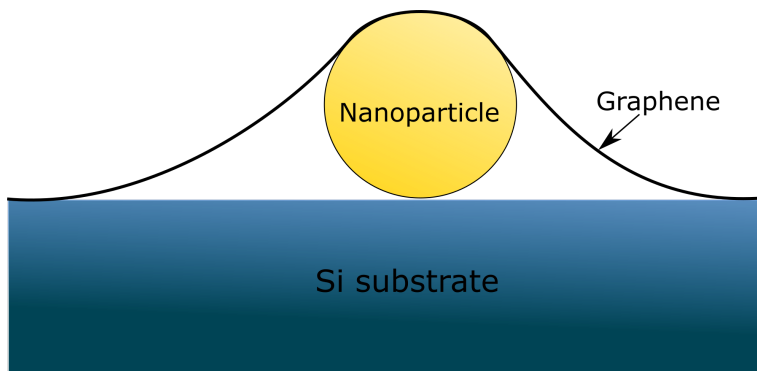
Figure 5.2: Illustration of tenting of graphene over nanoparticles.

4.3c at 1 kV, the Cu surface is barely visible compared to the graphene. On a Si surface at 5 kV in figure 4.7b, the graphene is less distinguishable from the Si and little tent or thickness contrast are seen, when comparing to figure 4.7c at 0.6 kV. Also worth noting, carbon contamination would quickly change the contrast and obscure details of the graphene at high magnification and high HT, but at low HT this was much less of an issue.

5.1.5 Transmission Electron Microscopy

BF-STEM

Images from the Hitachi operated in BF-STEM mode is seen in figure 4.9. Due to the thinness of graphene, very little of the 30 kV beam is absorbed or scattered. Therefore, to get any useful thickness contrast from the graphene, contrast had to be significantly digitally enhanced. This could possibly be improved by using an aperture to further increase contrast. As seen in figure 4.9a, this made anything thicker than ∼1 nm appear very dark. A significant issue with the microscope was the rapid growth of carbon contamination upon beam exposure. Focusing at high magnification, viewing and image capturing all caused a layer of contamination thicker than graphene, seen as the dark rectangles. Despite this, wrinkles and folds in the graphene could be seen. Imaging at high magnification was difficult due to the increased contamination rate. At high magnification, carbon was observed to grow from en edge at ∼1 nm/s. Some additional detail was seen in the image in figure 4.9b, where despite contamination obscuring details on the surface, a graphene grain boundary and iron oxide nanoparticles were seen. Increasing the scan rate of the beam and reducing the beam current and HT from 30 kV, reduced the contamination somewhat, but reduced current and HT also reduced the detected signal significantly. The same issues were worse in DF mode, where no good images could be acquired due to low signal and contrast. Due to the poor

results at high magnification, STEM was used mostly to quickly check if transfer onto TEM grids were successful, while most TEM work was instead done with the JEOL microscopes.

Contrast

Interpreting the contrast in TEM was much less straightforward than in SEM. The microscope was operated at 80, 120 and 200 kV, but at all HT almost all the electrons penetrates the graphene. This gave a weak thickness contrast in BF, and no surface contrasts as in low energy SEM. At low magnification seen in figure 4.10, the image is easily interpreted. But at higher magnification in figure 4.10c, the small focus depth along with the high transparency made the 3D structure projected overlapping as a 2D image that is challenging to interpret.

A feature of graphene that was easily seen however, were the interlayer lattice fringes. In many of the images at higher magnification, such as figures 4.12, 4.13, and 4.14a, the thickness of the graphene can be directly measured by counting the layers at the edge, with a spacing of ca 3.5 Å per layer. This contrast can also be seen in the walls of pieces of graphene that had rolled into a nanoscroll, such as seen in figures 4.11b and 4.15, but the thickness is not as clearly seen. Lattice fringes were also seen in figures 4.12 and 4.13 to give a spacing of 2.6 Å for the nanoparticles. In 4.13 there were also seen some unclear outlines of thin fragments, sized a few nanometers. These required the aberration corrected TEM at 80kV, to be identified as small graphene fragments (see section 5.1.6).

The low thickness contrast makes details that were visible in SEM, such as the secondary graphene domains, invisible. There is enough mass-thickness contrast to see both types of nanoparticles clearly. Wrinkles that formed during CVD are also not clearly visible, only the lattice fringes at their at edges can be seen. However, wrinkles formed during transfer can be seen due to the increased concentration of iron oxide particles. In figure 4.11a two examples of this are seen, a wide wrinkle and a thin flake lying across it, that was crumpled at the left of the image. The crumpled part looks darker due to a significantly higher concentration of nanoparticles. An additional contrast is seen in the thin wrinkle in figure 4.11a and the darker tip of the nanoscroll in figure 4.11b, where the curvature of the graphene has caused a diffraction contrast, making the edge darker.

Another feature of graphene that was sometimes seen at during the right conditions at high magnification, was grain boundaries in the monolayers. These were much less visible than the edge lattice fringes. One such is barely visible in figure 4.11c, and was verified by the SADP that changes from one orientation to another across the boundary. Similarly, a grain boundary was also seen in the BF-STEM image in figure 4.9b using the Hitachi microscope. But overall, these were very difficult to see by TEM.

Diffraction Patterns

During TEM operation DPs were routinely taken. Due to the presence of crumpled graphene, folds and wrinkles, most pattern seen were similar to the DP of the nanoscroll seen in figure 4.15, with two rings with spots of many rotations present. To get DPs of primarily monolayered graphene other obscuring details were avoided by using a small SA aperture sized a reducing the area to a few hundred nanometers. But the low amount of scattering from such thin materials, gave SADP with very low intensity. To capture these SADPs the beam not spread very much, and a poor diffraction focused was used. This enabled capturing the SADP seen in figure 4.11d giving a pattern of mostly just a monolayer. Such a SADP was easier to acquire in the aberration corrected TEM, seen in figure 4.18. In these DPs the different sets of spots correspond to the three lattice distances of the graphite crystal given in figure 2.1b. The innermost two spots correspond to edge lattice fringes, with a lattice spacing of the interlayer distance of 0.34 nm. The inner ring of six spots match the second nearest neighbour distance of 0.25 nm, and the outer ring is from the nearest neighbour distance of 0.14 nm.

The orientation of the DP give the graphene's orientation.[93,95] In figure 4.11c, the graphene on the right of the grain boundary, matching the stronger DP, is oriented with a zigzag edge along the boundary. The grain on the left is then, according to the weaker DP, rotated at 20° clockwise relative to the graphene on the right.

Dark-Field

Many attempts to acquire DF images from SADPs were done. But due to the low amount of electrons scattered from a material as thin as graphene, the DPs were very weak, and no good images could be made of monolayered graphene. The only good images that were taken were from pieces of crumpled graphene, such as the nanoscroll seen in figure 4.15. DF images from this DP are shown in figure 4.16, where the consistent fringes in 4.16b-d reflect ordering/stacking. The spots in the DP are broadened out due to variations in rotation by a few degrees, this causes the Moiré fringes seen in the DF images 4.16b-d. This is likely because of the nanoscroll having been rolled up imperfectly, as seen by the inside layers in figure 4.16a, and has a small conic angle instead of perfectly parallel sidewalls. Further analysis of these Moiré fringes are complicated, but they hold information about the relative orientation of the graphene layers.

Due to the thinness of the materials studied, a small amount of electrons are scattered from the main beam. Therefore, the dark-field images had a low brightness and required a long exposure time of several minutes, followed by post-processing contrast enhancement. The weak signal, in addition to the diffracted signal there was also a dim background signal from inelasticly scattered electrons from the materials. This causes the SiO_2 particles at the left and the additional crumpled graphene at the bottom, to also be visible in the images.

Beam Damage

The irradiation of the e-beam had as significant effect on the materials. Like in STEM with the Hitachi, there were some carbon contamination growing when imaging at high magnification, as seen in figure 4.14c. But in the JEOL TEMs this was much less of an issue compared to the Hitachi, likely due to the column, holder and vacuum being cleaner. The direct effect of the beam on the materials were however more significant. The two SiO_2 particles in figure 4.10d were observed to fuse during 1-2 minutes of study. In figure 4.14a and 4.14b, an edge of ∼10 graphene layers was observed to bend after 1 min exposure. The monolayered graphene was also severely affected. Nanometer sized holes formed quickly and after several minutes of exposure at high magnification, the graphene had often fallen apart. In figure 4.17b this is seen, where a ∼5 nm wide bridge that held up a larger sheet of highly damaged graphene, was imaged as it fell apart. When operating the aberration corrected TEM at atomic resolution, the area seen in figures 4.18 and 4.19 was irradiated for 7 minutes between the first and the last image. In this time, the nanoparticles were seen to move, change shape, merge and separate, and holes in the graphene were seen to appear and grow in size. The 2100 was operated at 80, 120 and 200 kV and the 200 ARM at 80 kV, but these damaging effects of the beam were not observed to vary significantly with changing HT. Although the rate of beam damage was lower at 80 kV, the graphene still disintegrated. Ideal graphene should have a knock-on threshold of ∼90 kV, but due to defects this is typically lower.[91] Therefore, operating at a lower voltage of 60 kV would be preferable.

5.1.6 High Resolution Transmission Microscopy

In the highest resolved images from the JEOL 2100 TEM, such as 4.12 and 4.13, a resolution of ∼2.6 Å is achieved. This is enough to see lattice fringes from the interlayer distance at the edge of multilayered graphene (3.4 Å), and from the iron oxide nanoparticles (2.6 Å). But this resolution is not enough to see the in-layer lattice distance of graphene (2.5 Å).

The aberration corrected JEOL 200 ARM achieves a higher resolution, and lattice fringes can be seen from all materials in figure 4.19. From studying this image and its FFT, the periodicity of the graphene matched 2.5 Å. From this image and others, periodicities of the smallest nanoparticles were found to range from 1.6 - 3.4 Å indicating iron oxide (see section 5.1.3). Fragments of secondary graphene are also seen, sized a few nanometers. These are different from the domains previously seen in SEM images. These might have been formed during CVD from excess carbon. It might also be remnant of the graphene from the underside of the foil, that was removed by plasma cleaning before transfer, as this seems to not have been removed completely (see section 5.1.2).

Electron Energy Loss Spectroscopy

The study of an area by EELS is seen in figures 4.20 and 4.21. The intention was to precisely characterize the nanoparticles. From the EDX and EELS spectra in respectively figures 4.20b and 4.20c, there were signals of C, O, Si and Fe in this area. The shape of the C peak in figure 4.20d is typical of graphene, with its sp_2-bond.[88] The maps in figure 4.21 clearly show the small nanoparticles to be of Fe, not C. Unfortunately mapping of O was not done, so exact determination of where O in the nanoparticles was, is not possible from this data. Therefore is it not possible to determine if the O in the EDX and EELS spectra were only from the larger SiO_2 particle on the left of figure 4.20a, or if there was O also in the smaller nanoparticles, as is suspected (see section 5.1.3).

The C post-peak EELS map in figure 4.21b also gives detailed information about the graphene. The area on the right of the image is monolayered, and the left is double layered. One or more layered graphene fragments also contributes to the thickness contrast. As seen by the inset intensity profile, along the red line it is possible to differentiate 1, 2 and 3 layers by thickness contrast.

HAADF-STEM

The JEOL ARM was operated in HAADF-STEM mode to more precisely identify the nanoparticles. This mode enables EDX mapping with nanometer resolution. Images and spectra from this is seen in figure 4.22. Figure 4.22a shows ADF imaging gives a useful thickness contrast, easily identifying wrinkles and folds in the graphene, similar to low energy SEM on a Si surface in figure 4.7. As seen in figure 4.22b, HAADF gives a clear Z-contrast, differentiating the iron oxide nanoparticles from the graphene. The point EDX measurements in figures 4.22c and 4.22d clearly identifies the larger particles as SiO_2 and the smaller as Fe. In conclusion, HAADF-STEM imaging is very useful and gives results similar to SEM and TEM results discussed above.

5.2　Graphene on Copper Thin Film

The idea of this method came from Ismach et al.[24] There, 100-450 nm Cu was e-beam deposited onto quartz and other dielectric substrates, then graphene was grown onto by low pressure CVD. Thereafter the Cu-TF was evaporated, leaving the graphene on the dielectric. The method given in section 3.1.2 differs somewhat, as a Si wafer substrate as used instead of dielectrics. Also instead of 1000°C, the CVD was operated at a higher temperature of 1030°C. The most significant difference was the CVD chamber pressure of 10 torr during CVD, compared to 100-500 mtorr in the article. Also in contrast to Ismach, after CVD all gas flow was stopped and the chamber pressure pumped as low as possible (the gauge only measured down to 1 mtorr), which was held for 10 minutes for evaporation.

The profilometer measurements in figure 4.23 indicated the Cu-TF was about 95 nm thick, and had an even surface with only nanoscale roughness. The as-deposited film was likely amorphous, but had crystallized during the heat treatment of the CVD. Despite this, as seen in the SEM images in figure 4.24, there was no obvious crystalline features of the Cu as it had dewetted. Also, when comparing to the reference sample, seen in figure 4.6, the SiO_2 particles are notably absent. This indicates the particles were not a feature of Cu surfaces in the system, but specifically a result of using this Cu foil in the system.

In contrast to Ismach's results for a 100 nm TF, most of the surface is still covered by Cu. This is likely due to the pressure during CVD being more than an order of magnitude higher, thus reducing the evaporation rate. Therefore, continuous graphene covers the entire surface before the evaporation phase begins. The presence of graphene is indicated by the many graphene wrinkles seen to have formed in the areas free of Cu in figure 4.24c. As the graphene hinders the evaporation rate of Cu, the rate was likely low during the evaporation phase, despite the low pressure and high temperature. Therefore, this experiment is more similar to Ismach's results with 450 nm Cu-TF, where the whole surface was covered by graphene and the Cu evaporated slowly; than with 100 nm Cu-TF, where the surface was only partially covered by graphene as the Cu had evaporated quickly.

In both experiments the dewetting causes a branching Cu pattern to form. A notable difference is that in Ismach, the branches are thin with a larger gap in between. This might be due to the higher temperature and lower pressure changing the surface tension and thus dewetting conditions of Cu. Or the substrate-Cu interaction might be different, as Si was not one of the substrates tested by them.

Due to the low evaporation rate of Cu, in Ismach et al. they tried up to 7 hours of evaporation time on the samples covered by graphene. As there was also much Cu left on the samples after the process, it would likely require hours of evaporation time to clear the surface of Cu. Even in areas where no Cu was detected by SEM, there would likely be trace amounts left. As one of the intentions of this work was to make graphene without Cu contamination, this method was not promising.

Chapter 6

Conclusion

The purpose of this work was to grow graphene by a newly installed CVD and study it by SEM and TEM available on site, for quality assurance and growth optimization. The CVD growth was done in 5 batches, at $1000°C$ and low pressure, with Cu foil as growth substrate. The 1st batch was contaminated by particles caused by a stainless steel stage, and the 4th batch failed to yield graphene. In the remaining three batches, the Cu foil was covered by a monolayer of graphene, along with SiO_2 nanoparticles, around which domains of a second graphene layer had also formed. Little difference was found between these three batches, despite a significant change in growth parameters. For optimizing the growth process, further work is required. To study the graphene further, the Cu foil was etched in a bath of $Fe(NO_3)_3$, and the remaining graphene was scooped onto a TEM grid or Si wafer. The etchant process also left iron oxide nanoparticles on the samples, sized ~5 nm.

It was found that SEM was most useful at low HT, around 1 kV, as the low penetration depth of the electrons makes the contrast of the upper atomic layers dominate. This made it possible to study the thickness and wrinkles of the graphene, separate from the contrast of the substrate surface. Transferring onto Si was especially useful for studying graphene, as the thickness contrast became clearer and studying graphene grain boundaries became possible. BF-TEM was useful for proving conclusively that the graphene was monolayered, but little additional details of the graphene could be seen. However, aberration corrected TEM proved useful, as the high resolution enabled study of defects in the graphene. EELS mapping was shown to give a layered thickness contrast of graphene at high resolution. HAADF-STEM proved especially useful, as it also gave precise thickness contrast of graphene, but also enabled high precision EDX, to determine the chemical composition of the contaminant nanoparticles.

Additionally, a new process was attempted for growing graphene without transfer, by first depositing a 100 nm Cu thin film on Si wafer. Then after CVD, the Cu was evaporated by keeping the temperature at 1030°C at low pressure. However, this technique was not very successful, as the graphene covering the sample prevented the Cu from evaporating completely. Longer evaporation time and further optimization are required. In this test growth, there was also control samples of Cu foil. As there was no SiO_2 nanoparticles on the Cu thin film, but on the Cu foil, the particles formed due to an unknown feature of the Cu foil.

Chapter 7

Future Work

Many suggestions can be made for how this work can be improved. Further optimization of the CVD process on Cu can likely be done by decreasing the chamber pressure and CH_4:H_2 ratio, and especially by doing chemical mechanical polishing of the Cu. These steps have been shown to reduce nucleation density and thus graphene grain size.[101] Considering the Cu foil was found to have caused the SiO_2 particles to form, a different Cu substrate should be used, ideally a Cu monocrystal, as grain boundaries increase the nucleation density. The etching process is also highly problematic. To avoid the formation of Fe particles another etchant should be used. It has also been shown that Fe-based etching weakens graphene grain boundaries, therefore different etchants such as $(NH_4)_2S_2O_8$ and HNO_3 has been suggested.[63,102] Many other transfer techniques have also been suggested, to avoid the formation of defects and without polymer contamination.[37,74,103,104] Additionally, for completely removing contamination of graphene and particles from the underside of the foil, stronger plasma cleaning should be used.

Methods to characterize the materials can be improved as well. An issue in this work was to identify contamination of Cu after transfer to TEM grid, as the grid was also of Cu. Therefore TEM grids of a different material should be used, e.g. Mo. The exact structure of the graphene wrinkles, as they formed on the Cu foil, can be studied more in detail by using AFM.[24] SEMs can also be operated at an even lower voltage, using surface deceleration, to improve the contrast for surface details. LEEM has been proven highly useful for in-situ study of CVD growth of graphene, which makes optimizing the growth process much easier.[84] These methods should be considered as means to evaluate growth optimization.

In this work we also cooperated with a group that grow semiconductor nanowires on graphene by MBE.[21] However, MBE is very sensitive to contamination by Cu, so it must be avoided. Therefore, we also attempted growing graphene on a Ge thin film (deposited by EBD), as this have been shown to make high quality graphene.[19,105] A preliminary experiment using the same CVD growth parameters

as batch 5 in table 3.1, gave ∼5 layers thick graphene, as shown by TEM in figure 7.1a. Raman spectroscopy is also a highly useful technique for characterizing graphene, enabling quantification of defects and grain structure.[20,106] A preliminary Raman spectrum measured from graphene grown on Ge is shown in figure 7.1b, indicating the graphene has grown with a high crystalline quality. These initial results look promising and a systematic growth study should be done.
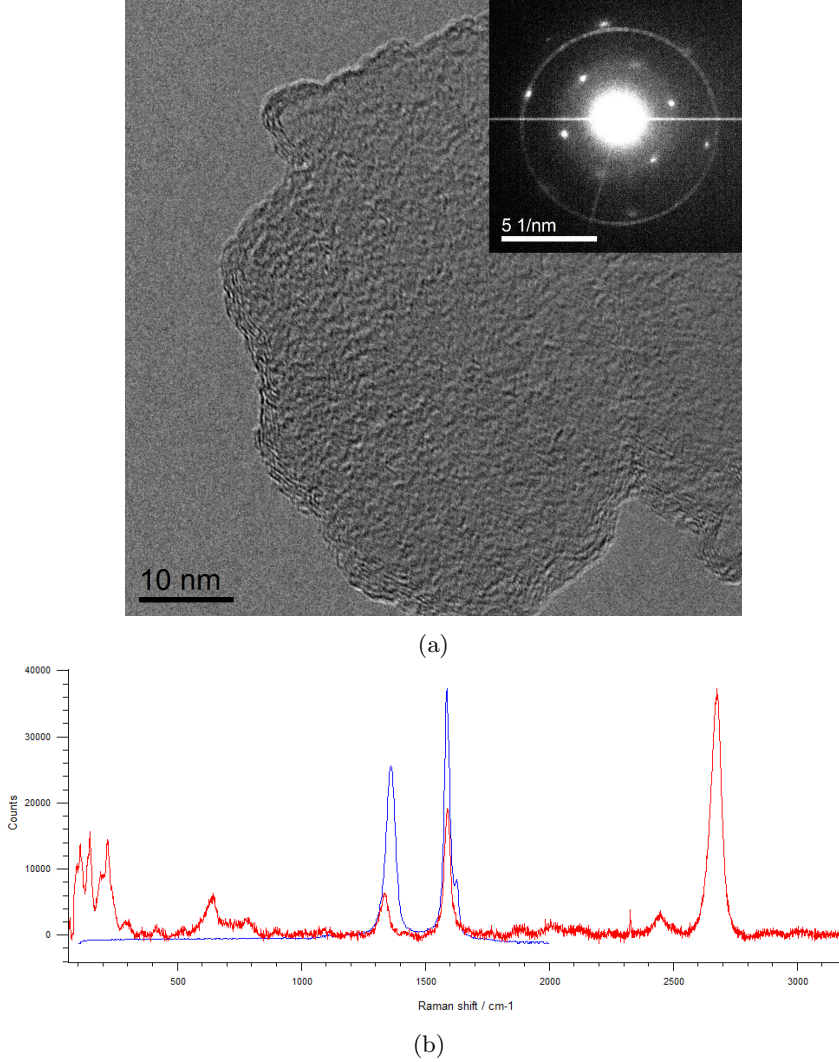

(a)

(b)

Figure 7.1: **(a)** HRTEM image of the edge of graphene grown on Ge. Inset is a SADP of this area (the ring is from the small SA aperture used). **(b)** Raman spectrum of graphene grown on Ge (red is the measurement and blue is a graphite fingerprint from a library).

References

[1] H. P. Boehm et al. "Das Adsorptionsverhalten sehr dünner Kohlenstoff-Folien". In: *Zeitschrift für anorganische und allgemeine Chemie* 316.3-4 (1962), pp. 119–127. URL: http://onlinelibrary.wiley.com/doi/10.1002/zaac.19623160303/abstract.

[2] K. S. Novoselov. "Electric Field Effect in Atomically Thin Carbon Films". In: *Science* 306.5696 (2004), pp. 666–669. URL: http://science.sciencemag.org/content/306/5696/666.

[3] Nobelprize.org. *The 2010 Nobel Prize in Physics - Press Release*. 2010. URL: http://www.nobelprize.org/nobel_prizes/physics/laureates/2010/press.html (visited on 02/10/2016).

[4] A. K. Geim and K. S. Novoselov. "The rise of graphene". In: *Nature Materials* 6.3 (2007), pp. 183–191. URL: http://www.nature.com/nmat/journal/v6/n3/abs/nmat1849.html.

[5] A. K. Geim. "Graphene: Status and Prospects". In: *Science* 324.5934 (2009), pp. 1530–1534. URL: http://science.sciencemag.org/content/324/5934/1530.short.

[6] R. R. Nair et al. "Unimpeded Permeation of Water Through Helium-Leak-Tight Graphene-Based Membranes". In: *Science* 335.6067 (2012), pp. 442–444. URL: http://science.sciencemag.org/content/335/6067/442.

[7] Y. Wang et al. "Supercapacitor Devices Based on Graphene Materials". In: *The Journal of Physical Chemistry C* 113.30 (2009), pp. 13103–13107. URL: http://pubs.acs.org/doi/abs/10.1021/jp902214f.

[8] E. Yoo et al. "Large Reversible Li Storage of Graphene Nanosheet Families for Use in Rechargeable Lithium Ion Batteries". In: *Nano Letters* 8.8 (2008), pp. 2277–2282. URL: http://pubs.acs.org/doi/abs/10.1021/nl800957b.

[9] Y. Zhang et al. "Experimental observation of the quantum Hall effect and Berry's phase in graphene". In: *Nature* 438.7065 (2005), pp. 201–204. URL: http://www.nature.com/nature/journal/v438/n7065/full/nature04235.html.

[10] K. S. Novoselov et al. "Room-Temperature Quantum Hall Effect in Graphene".
      In: *Science* 315.5817 (2007), pp. 1379–1379. URL: http://science.
      sciencemag.org/content/315/5817/1379.

[11] A. S. Mayorov et al. "Micrometer-Scale Ballistic Transport in Encapsulated
      Graphene at Room Temperature". In: *Nano Letters* 11.6 (2011), pp. 2396–
      2399. URL: http://pubs.acs.org/doi/abs/10.1021/nl200758b.

[12] J. J. Palacios. "Graphene nanoribbons: Electrons go ballistic". In: *Nature
      Physics* 10.3 (2014), pp. 182–183. URL: http://www.nature.com/nphys/
      journal/v10/n3/full/nphys2909.html.

[13] B. Uchoa and A. H. Castro Neto. "Superconducting States of Pure and
      Doped Graphene". In: *Physical Review Letters* 98.14 (2007), p. 146801. URL:
      http://journals.aps.org/prl/abstract/10.1103/PhysRevLett.98.
      146801.

[14] A. H. Castro Neto et al. "The electronic properties of graphene". In: *Reviews
      of Modern Physics* 81.1 (2009), pp. 109–162. URL: http://journals.aps.
      org/rmp/abstract/10.1103/RevModPhys.81.109.

[15] P. Avouris. "Graphene: Electronic and Photonic Properties and Devices".
      In: *Nano Letters* 10.11 (2010), pp. 4285–4294. URL: http://pubs.acs.
      org/doi/abs/10.1021/nl102824h.

[16] K. S. Novoselov et al. "A roadmap for graphene". In: *Nature* 490.7419
      (2012), pp. 192–200. URL: http://www.nature.com/nature/journal/
      v490/n7419/full/nature11458.html.

[17] S. Bae et al. "Roll-to-roll production of 30-inch graphene films for trans-
      parent electrodes." In: *Nature Nanotechnology* 5.8 (2010), pp. 574–8. URL:
      http://www.nature.com/nnano/journal/v5/n8/abs/nnano.2010.132.
      html.

[18] K. R. Paton et al. "Scalable production of large quantities of defect-free
      few-layer graphene by shear exfoliation in liquids". In: *Nature Materials*
      13.6 (2014), pp. 624–630. URL: http://www.nature.com/nmat/journal/
      v13/n6/full/nmat3944.html.

[19] J.-H. Lee et al. "Wafer-Scale Growth of Single-Crystal Monolayer Graphene
      on Reusable Hydrogen-Terminated Germanium". In: *Science* 344.6181 (2014),
      pp. 286–289. URL: http://science.sciencemag.org/content/344/
      6181/286.

[20] A. C. Ferrari et al. "Raman Spectrum of Graphene and Graphene Lay-
      ers". In: *Physical Review Letters* 97.18 (2006), p. 187401. URL: http:
      //journals.aps.org/prl/abstract/10.1103/PhysRevLett.97.187401.

[21] A. M. Munshi et al. "Vertically Aligned GaAs Nanowires on Graphite and
      Few-Layer Graphene: Generic Model and Epitaxial Growth". In: *Nano Let-
      ters* 12.9 (2012), pp. 4570–4576. URL: http://pubs.acs.org/doi/abs/
      10.1021/nl3018115.

[22] A. Mazid Munshi and H. Weman. "Advances in semiconductor nanowire growth on graphene". In: *physica status solidi (RRL) - Rapid Research Letters* 7.10 (2013), pp. 713–726. URL: http://onlinelibrary.wiley.com/doi/10.1002/pssr.201308010/abstract.

[23] X. Li et al. "Transfer of Large-Area Graphene Films for High-Performance Transparent Conductive Electrodes". In: *Nano Letters* 9.12 (2009), pp. 4359–4363. URL: http://pubs.acs.org/doi/abs/10.1021/nl902623y.

[24] A. Ismach et al. "Direct Chemical Vapor Deposition of Graphene on Dielectric Surfaces". In: *Nano Letters* 10.5 (2010), pp. 1542–1548. URL: http://pubs.acs.org/doi/abs/10.1021/nl9037714.

[25] Nanosurf. *STM on HOPG*. 2006. URL: https://www.nanosurf.com/en/application/244-stm-on-hopg-atomic-resolution-in-air (visited on 02/11/2016).

[26] C. Lee et al. "Measurement of the Elastic Properties and Intrinsic Strength of Monolayer Graphene". In: *Science* 321.5887 (2008), pp. 385–388. URL: http://science.sciencemag.org/content/321/5887/385.

[27] N. Savage. "Materials science: Super carbon". In: *Nature* 483.7389 (2012), S30–S31. URL: http://www.nature.com/nature/journal/v483/n7389_supp/full/483S30a.html.

[28] V. M. Pereira, A. H. Castro Neto, and N. M. R. Peres. "Tight-binding approach to uniaxial strain in graphene". In: *Physical Review B* 80.4 (2009), p. 045401. URL: http://journals.aps.org/prb/abstract/10.1103/PhysRevB.80.045401.

[29] S. Stankovich et al. "Graphene-based composite materials". In: *Nature* 442.7100 (2006), pp. 282–286. URL: http://www.nature.com/nature/journal/v442/n7100/full/nature04969.html.

[30] T Ramanathan et al. "Functionalized graphene sheets for polymer nanocomposites". In: *Nature Nanotechnology* 3.6 (2008), pp. 327–331. URL: http://www.nature.com/nnano/journal/v3/n6/full/nnano.2008.96.html.

[31] J. T. Robinson et al. "Wafer-scale Reduced Graphene Oxide Films for Nanomechanical Devices". In: *Nano Letters* 8.10 (2008), pp. 3441–3445. URL: http://pubs.acs.org/doi/abs/10.1021/nl8023092.

[32] J. S. Bunch et al. "Electromechanical Resonators from Graphene Sheets". In: *Science* 315.5811 (2007), pp. 490–493. URL: http://science.sciencemag.org/content/315/5811/490.

[33] B. Butz et al. "Dislocations in bilayer graphene". In: *Nature* 505.7484 (2013), pp. 533–537. URL: http://www.nature.com/nature/journal/vaop/ncurrent/full/nature12780.html.

[34] W. J. Yu et al. "Toward Tunable Band Gap and Tunable Dirac Point in Bilayer Graphene with Molecular Doping". In: *Nano Letters* 11.11 (2011), pp. 4759–4763. URL: http://pubs.acs.org/doi/abs/10.1021/nl2025739.

[35] J.-H. Chen et al. "Intrinsic and extrinsic performance limits of graphene devices on SiO2". In: *Nature Nanotechnology* 3.4 (2008), pp. 206–209. URL: http://www.nature.com/nnano/journal/v3/n4/full/nnano.2008.58.html.

[36] K. Bolotin et al. "Ultrahigh electron mobility in suspended graphene". In: *Solid State Communications* 146.9-10 (2008), pp. 351–355. URL: http://www.sciencedirect.com/science/article/pii/S0038109808001178.

[37] W.-H. Lin et al. "A direct and polymer-free method for transferring graphene grown by chemical vapor deposition to any substrate." In: *ACS Nano* 8.2 (2014), pp. 1784–91. URL: http://pubs.acs.org/doi/abs/10.1021/nn406170d.

[38] F. Xia et al. "Graphene Field-Effect Transistors with High On/Off Current Ratio and Large Transport Band Gap at Room Temperature". In: *Nano Letters* 10.2 (2010), pp. 715–718. URL: http://pubs.acs.org/doi/abs/10.1021/nl9039636.

[39] F. Schwierz. "Graphene transistors". In: *Nature Nanotechnology* 5.7 (2010), pp. 487–496. URL: http://www.nature.com/nnano/journal/v5/n7/full/nnano.2010.89.html.

[40] R. R. Nair et al. "Fine Structure Constant Defines Visual Transparency of Graphene". In: *Science* 320.5881 (2008), pp. 1308–1308. URL: http://science.sciencemag.org/content/320/5881/1308.

[41] A. B. Kuzmenko et al. "Universal Optical Conductance of Graphite". In: *Physical Review Letters* 100.11 (2008), p. 117401. URL: http://journals.aps.org/prl/abstract/10.1103/PhysRevLett.100.117401.

[42] J. Wu et al. "Organic solar cells with solution-processed graphene transparent electrodes". In: *Applied Physics Letters* 92.26 (2008), p. 263302. URL: http://scitation.aip.org/content/aip/journal/apl/92/26/10.1063/1.2924771.

[43] K. S. Kim et al. "Large-scale pattern growth of graphene films for stretchable transparent electrodes". In: *Nature* 457.7230 (2009), pp. 706–710. URL: http://www.nature.com/nature/journal/v457/n7230/full/nature07719.html.

[44] F. Xia et al. "Ultrafast graphene photodetector". In: *Nature Nanotechnology* 4.12 (2009), pp. 839–843. URL: http://www.nature.com/nnano/journal/v4/n12/full/nnano.2009.292.html.

[45] C.-H. Liu et al. "Graphene photodetectors with ultra-broadband and high responsivity at room temperature". In: *Nature Nanotechnology* 9.4 (2014), pp. 273–278. URL: http://www.nature.com/nnano/journal/v9/n4/full/nnano.2014.31.html.

[46] G. Diankov, M. Neumann, and D. Goldhaber-Gordon. "Extreme monolayer-selectivity of hydrogen-plasma reactions with graphene." In: *ACS Nano* 7.2 (2013), pp. 1324–32. URL: http://pubs.acs.org/doi/abs/10.1021/nn304903m.

[47] D. Cohen-Tanugi and J. C. Grossman. "Water Desalination across Nanoporous Graphene". In: *Nano Letters* 12.7 (2012), pp. 3602–3608. URL: http://pubs.acs.org/doi/abs/10.1021/nl3012853.

[48] R. K. Joshi et al. "Precise and Ultrafast Molecular Sieving Through Graphene Oxide Membranes". In: *Science* 343.6172 (2014), pp. 752–754. URL: http://science.sciencemag.org/content/343/6172/752.short.

[49] V. Chandra et al. "Water-Dispersible Magnetite-Reduced Graphene Oxide Composites for Arsenic Removal". In: *ACS Nano* 4.7 (2010), pp. 3979–3986. URL: http://pubs.acs.org/doi/abs/10.1021/nn1008897.

[50] K. S. Novoselov et al. "Two-dimensional atomic crystals". In: *Proceedings of the National Academy of Sciences* 102.30 (2005), pp. 10451–10453. URL: http://www.pnas.org/content/102/30/10451.

[51] H. Li et al. "Mechanical Exfoliation and Characterization of Single- and Few-Layer Nanosheets of WSe 2 , TaS 2 , and TaSe 2". In: *Small* 9.11 (2013), pp. 1974–1981. URL: http://onlinelibrary.wiley.com/doi/10.1002/smll.201202919/abstract.

[52] G.-H. Lee et al. "Flexible and Transparent MoS 2 Field-Effect Transistors on Hexagonal Boron Nitride-Graphene Heterostructures". EN. In: *ACS Nano* 7.9 (2013), pp. 7931–7936. URL: http://pubs.acs.org/doi/abs/10.1021/nn402954e.

[53] T. Georgiou et al. "Vertical field-effect transistor based on graphene-WS2 heterostructures for flexible and transparent electronics." In: *Nature Nanotechnology* 8.2 (2013), pp. 100–3. URL: http://www.nature.com/nnano/journal/v8/n2/full/nnano.2012.224.html.

[54] W. S. Hummers and R. E. Offeman. "Preparation of Graphitic Oxide". In: *Journal of the American Chemical Society* 80.6 (1958), pp. 1339–1339. URL: http://pubs.acs.org/doi/abs/10.1021/ja01539a017.

[55] N. I. Kovtyukhova et al. "Layer-by-Layer Assembly of Ultrathin Composite Films from Micron-Sized Graphite Oxide Sheets and Polycations". In: *Chemistry of Materials* 11.3 (1999), pp. 771–778. URL: http://pubs.acs.org/doi/abs/10.1021/cm981085u.

[56] D. a. Dikin et al. "Preparation and characterization of graphene oxide paper". In: *Nature* 448.7152 (2007), pp. 457–460. URL: http://www.nature.com/nature/journal/v448/n7152/full/nature06016.html.

[57] D. Li et al. "Processable aqueous dispersions of graphene nanosheets". In: *Nature Nanotechnology* 3.2 (2008), pp. 101–105. URL: http://www.nature.com/nnano/journal/v3/n2/full/nnano.2007.451.html.

[58] K. V. Emtsev et al. "Towards wafer-size graphene layers by atmospheric pressure graphitization of silicon carbide". In: *Nature Materials* 8.3 (2009), pp. 203–207. URL: http://www.nature.com/nmat/journal/v8/n3/full/nmat2382.html.

[59] H. Kim et al. "Activation energy paths for graphene nucleation and growth on Cu." In: *ACS Nano* 6.4 (2012), pp. 3614–23. URL: http://pubs.acs.org/doi/abs/10.1021/nn3008965.

[60] *Graphene Square. Thermal CVD system.* 2011. URL: http://www.graphenesq.com/graphene/goods_detail.asp?productid=10 (visited on 06/11/2014).

[61] P. Y. Huang et al. "Grains and grain boundaries in single-layer graphene atomic patchwork quilts". In: *Nature* 469.7330 (2011), pp. 389–392. URL: http://www.nature.com/nature/journal/v469/n7330/full/nature09718.html.

[62] I. Vlassiouk et al. "Graphene Nucleation Density on Copper: Fundamental Role of Background Pressure". In: *The Journal of Physical Chemistry C* 117.37 (2013), pp. 18919–18926. URL: http://pubs.acs.org/doi/abs/10.1021/jp4047648.

[63] C. Mattevi, H. Kim, and M. Chhowalla. "A review of chemical vapour deposition of graphene on copper". In: *J. Mater. Chem.* 21.10 (2011), pp. 3324–3334. URL: http://pubs.rsc.org/en/Content/ArticleLanding/2011/JM/c0jm02126a#!divAbstract.

[64] I. Vlassiouk et al. "Role of hydrogen in chemical vapor deposition growth of large single-crystal graphene." In: *ACS Nano* 5.7 (2011), pp. 6069–76. URL: http://pubs.acs.org/doi/abs/10.1021/nn201978y.

[65] S. J. Chae et al. "Synthesis of Large-Area Graphene Layers on Poly-Nickel Substrate by Chemical Vapor Deposition: Wrinkle Formation". In: *Advanced Materials* 21.22 (2009), pp. 2328–2333. URL: http://onlinelibrary.wiley.com/doi/10.1002/adma.200803016/abstract.

[66] L. Zhao et al. "Influence of copper crystal surface on the CVD growth of large area monolayer graphene". In: *Solid State Communications* 151.7 (2011), pp. 509–513. URL: http://www.sciencedirect.com/science/article/pii/S0038109811000433.

[67] G. H. Han et al. "Influence of Copper Morphology in Forming Nucleation Seeds for Graphene Growth". In: *Nano Letters* 11.10 (2011), pp. 4144–4148. URL: http://pubs.acs.org/doi/abs/10.1021/nl201980p.

[68] Y. Gamo et al. "Atomic Structure of Monolayer Graphite Formed on Ni(111)." In: *Hyomen Kagaku* 17.12 (1996), pp. 745–749. URL: https://www.jstage.jst.go.jp/article/jsssj1980/17/12/17_12_745/_article/-char/ja/.

[69] A. Reina et al. "Large Area, Few-Layer Graphene Films on Arbitrary Substrates by Chemical Vapor Deposition". In: *Nano Letters* 9.1 (2009), pp. 30–35. URL: http://pubs.acs.org/doi/abs/10.1021/nl801827v.

[70] X. Li et al. "Large-Area Synthesis of High-Quality and Uniform Graphene Films on Copper Foils". In: *Science* 324.5932 (2009), pp. 1312–1314. URL: http://science.sciencemag.org/content/324/5932/1312.

[71] X. Liang et al. "Toward Clean and Crackless Transfer of Graphene". In: *ACS Nano* 5.11 (2011), pp. 9144–9153. URL: http://pubs.acs.org/doi/abs/10.1021/nn203377t.

[72] L. Gao et al. "Face-to-face transfer of wafer-scale graphene films". In: *Nature* 505.7482 (2013), pp. 190–194. URL: http://www.nature.com/nature/journal/v505/n7482/full/nature12763.html.

[73] W. Regan et al. "A direct transfer of layer-area graphene". In: *Applied Physics Letters* 96.11 (2010), p. 113102. URL: http://scitation.aip.org/content/aip/journal/apl/96/11/10.1063/1.3337091.

[74] J.-Y. Choi. "Graphene transfer: A stamp for all substrates". In: *Nature Nanotechnology* 8.5 (2013), pp. 311–312. URL: http://www.nature.com/nnano/journal/v8/n5/full/nnano.2013.74.html.

[75] Y.-C. Lin et al. "Graphene Annealing: How Clean Can It Be?" In: *Nano Letters* 12.1 (2012), pp. 414–419. URL: http://pubs.acs.org/doi/abs/10.1021/nl203733r.

[76] N. Nanolab. *Hitachi S-5500 S(T)EM*. 2014. URL: http://www.norfab.no/technologies/characterization/ntnu-nanolab/stem/ (visited on 02/11/2016).

[77] Hitachi High-Tech. *Ultra-high Resolution Scanning Electron Microscope S-5500*. Tech. rep. 2004. URL: http://www.spectral.se/spectral.nsf/f164f3e9b82f0febc1256dcc004611c1/973be1ca97284456c1256f4a007aadc6/.

[78] Hitachi High-Tech. *Hitachi SU9000*. 2014. URL: http://www.hht-eu.com/cms/5149.html (visited on 02/11/2016).

[79] Y Zhu et al. "Imaging single atoms using secondary electrons with an aberration-corrected electron microscope". In: *Nature Materials* 8.10 (2009), pp. 808–812. URL: http://www.nature.com/nmat/journal/v8/n10/full/nmat2532.html.

[80] R. F. Egerton. *Physical Principles of Electron Microscopy*. Springer Berlin Heidelberg, 2005. URL: http://www.springer.com/gp/book/9780387258003.

[81] P. Sutter et al. "Chemical Vapor Deposition and Etching of High-Quality Monolayer Hexagonal Boron Nitride Films". In: *ACS Nano* 5.9 (2011), pp. 7303–7309. URL: http://pubs.acs.org/doi/abs/10.1021/nn202141k.

[82] A. Acun et al. "The instability of silicene on Ag(111)". In: *Applied Physics Letters* 103.26 (2013), p. 263119. URL: http://scitation.aip.org/content/aip/journal/apl/103/26/10.1063/1.4860964.

[83] C. M. Orofeo et al. "Growth and low-energy electron microscopy characterization of monolayer hexagonal boron nitride on epitaxial cobalt". In: *Nano Research* 6.5 (2013), pp. 335–347. URL: http://link.springer.com/10.1007/s12274-013-0310-1.

[84] R. Addou et al. "Monolayer graphene growth on Ni(111) by low temperature chemical vapor deposition". In: *Applied Physics Letters* 100.2 (2012), p. 021601. URL: http://scitation.aip.org/content/aip/journal/apl/100/2/10.1063/1.3675481.

[85] *EMEZ ETH Zürich. SEM: Imaging with Secondary Electrons.* 2012. URL: http://www.microscopy.ethz.ch/se.htm (visited on 02/11/2016).

[86] James H. Wittike. *GLG 510 - Electron Microprobe Techniques.* 2007. URL: http://www4.nau.edu/microanalysis/microprobe-sem/signals.html (visited on 12/06/2014).

[87] Hitachi High-Tech. *Ultra-high Resolution Scanning Electron Microscope SU8000 Series.* Tech. rep. 2011. URL: http://www.hitachi-hightech.com/us/product_detail/?pn=em-su8000series.

[88] D. B. Williams and C. B. Carter. *The Transmission Electron Microscope.* Springer Berlin Heidelberg, 2009. URL: http://link.springer.com/book/10.1007/978-1-4757-2519-3.

[89] NTNU Gemini Center. *NTNU Gemini Center. JEOL JEM-2100.* 2013. URL: http://www.ntnu.edu/geminicentre/j2100 (visited on 07/03/2014).

[90] JEOL. *JEM-2100 Instructions.* Tech. rep. 2004. URL: http://www.jeol.co.jp/en.

[91] J. C. Meyer et al. "Accurate Measurement of Electron Beam Induced Displacement Cross Sections for Single-Layer Graphene". In: *Physical Review Letters* 108.19 (2012), p. 196102. URL: http://link.aps.org/doi/10.1103/PhysRevLett.108.196102.

[92] H. Kauko et al. "Compositional characterization of GaAs/GaAsSb nanowires by quantitative HAADF-STEM". In: *Micron* 44.1 (2013), pp. 254–260. URL: http://linkinghub.elsevier.com/retrieve/pii/S0968432812001990.

[93] A. W. Robertson and J. H. Warner. "Hexagonal Single Crystal Domains of Few-Layer Graphene on Copper Foils". In: *Nano Letters* 11.3 (2011), pp. 1182–1189. URL: http://pubs.acs.org/doi/abs/10.1021/nl104142k.

[94] A. Mohsin et al. "Synthesis of millimeter-size hexagon-shaped graphene single crystals on resolidified copper." In: *ACS Nano* 7.10 (2013), pp. 8924–31. URL: http://pubs.acs.org/doi/abs/10.1021/nn4034019.

[95] Q. Yu et al. "Control and characterization of individual grains and grain boundaries in graphene grown by chemical vapour deposition". In: *Nature Materials* 10.6 (2011), pp. 443–449. URL: http://www.nature.com/nmat/journal/v10/n6/full/nmat3010.html.

[96] Y. Sun et al. "Radiation-Induced Nucleation of Diamond from Amorphous Carbon: Effect of Hydrogen". In: *The Journal of Physical Chemistry Letters* 5.11 (2014), pp. 1924–1928. URL: http://pubs.acs.org/doi/abs/10.1021/jz5007912.

[97]   H. Hiura, H. Miyazaki, and K. Tsukagoshi. "Determination of the Number of Graphene Layers: Discrete Distribution of the Secondary Electron Intensity Stemming from Individual Graphene Layers". In: *Applied Physics Express* 3.9 (2010), p. 095101. URL: http://iopscience.iop.org/article/10.1143/APEX.3.095101.

[98]   J. Xie and J. P. Spallas. *Different contrast mechanisms in SEM imaging of graphene*. Tech. rep. 2012. URL: http://literature.agilent.com/litweb/pdf/5991-0782EN.pdf.

[99]   J. Xie and J. P. Spallas. *Imaging Graphene via Low Voltage Field Emission Scanning Electron Microscopy Application Note*. Tech. rep. Agilent Technologies, 2012. URL: cp.literature.agilent.com/litweb/pdf/5991-0781EN.pdf.

[100] V. Kochat et al. "High contrast imaging and thickness determination of graphene with in-column secondary electron microscopy". In: *Journal of Applied Physics* 110.1 (2011), p. 014315. URL: http://scitation.aip.org/content/aip/journal/jap/110/1/10.1063/1.3608062.

[101] F. Yang et al. "A facile method to observe graphene growth on copper foil". In: *Nanotechnology* 23.47 (2012), p. 475705. URL: http://iopscience.iop.org/article/10.1088/0957-4484/23/47/475705/meta.

[102] G.-H. Lee et al. "High-Strength Chemical-Vapor-Deposited Graphene and Grain Boundaries". In: *Science* 340.6136 (2013), pp. 1073–1076. URL: http://science.sciencemag.org/content/340/6136/1073.

[103] L. Banszerus et al. "Ultrahigh-mobility graphene devices from chemical vapor deposition on reusable copper." en. In: *Science Advances* 1.6 (2015), e1500222. URL: http://advances.sciencemag.org/content/1/6/e1500222.abstract.

[104] D. Q. McNerny et al. "Direct fabrication of graphene on SiO2 enabled by thin film stress engineering". In: *Scientific Reports* 4 (2014), pp. 1–9. URL: http://www.nature.com/articles/srep05049.

[105] G. Wang et al. "Direct Growth of Graphene Film on Germanium Substrate". In: *Scientific Reports* 3 (2013), p. 2465. URL: http://www.nature.com/articles/srep02465.

[106] L. Malard et al. "Raman spectroscopy in graphene". In: *Physics Reports* 473.5-6 (2009), pp. 51–87. URL: http://www.sciencedirect.com/science/article/pii/S0370157309000520.